

AD/A-004 647

RESEARCH IN MATERIALS SCIENCE

D. Epstein, et al

Massachusetts Institute of Technology

Prepared for:

Advanced Research Projects Agency  
Defense Supply Service

31 December 1974

DISTRIBUTED BY:

**NTIS**

National Technical Information Service  
U. S. DEPARTMENT OF COMMERCE

**UNCLASSIFIED**

SECURITY CLASSIFICATION OF THIS PAGE (When Data Entered)

REPORT DOCUMENTATION PAGE		READ INSTRUCTIONS BEFORE COMPLETING FORM
1. REPORT NUMBER <b>#3</b>	2. GOVT ACCESSION NO.	3. RECIPIENT'S CATALOG NUMBER <b>AD/A-004647</b>
4. TITLE (and Subtitle)  <b>Research in Materials Science</b>		5. TYPE OF REPORT & PERIOD COVERED <b>Semi-Annual Technical 1 July 1974 - 31 Dec. 1974</b>
		6. PERFORMING ORG. REPORT NUMBER
7. AUTHOR(s) <b>D. Epstein, R. M. Rose, M. MacVicar, R. Lagow</b>		8. CONTRACT OR GRANT NUMBER(s)  <b>DAHC 15-73-C-0316</b>
9. PERFORMING ORGANIZATION NAME AND ADDRESS <b>Massachusetts Institute of Technology Center for Materials Science and Engineering Cambridge, Mass. 02139</b>		10. PROGRAM ELEMENT, PROJECT, TASK AREA & WORK UNIT NUMBERS  <b>3D10</b>
11. CONTROLLING OFFICE NAME AND ADDRESS <b>Defense Supply Service-Washington Room 1D 245 - The Pentagon Washington, D. C. 20310</b>		12. REPORT DATE <b>31 Dec. 1974</b>
14. MONITORING AGENCY NAME & ADDRESS (if different from Controlling Office) <b>ONR Resident Representative M.I.T. Room E19-629 Cambridge, Mass. 02139</b>		13. NUMBER OF PAGES <b>228</b>
		15. SECURITY CLASS. (of this report) <b>Unclassified</b>
16. DISTRIBUTION STATEMENT (of this Report)  <b>UNLIMITED</b>		15a. DECLASSIFICATION/DOWNGRADING SCHEDULE
17. DISTRIBUTION STATEMENT (of the abstract entered in Block 20, if different from Report)  <b>UNLIMITED</b>		
18. SUPPLEMENTARY NOTES		
19. KEY WORDS (Continue on reverse side if necessary and identify by block number) <b>Optoelectronic Materials, Components, Miniaturized Laser Sources and Thin Film Modulators; Superconducting Transition Metal Alloys; Chemical Synthesis/High Temperature Lithium Vapor Species</b>		
20. ABSTRACT (Continue on reverse side if necessary and identify by block number) <b>This report presents the Results and status of work after the third six month period of this research program which consists of three (originally five) separate tasks involving research in Materials Science.</b>  <b>)</b>		

1  
UNCLASSIFIED

SECURITY CLASSIFICATION OF THIS PAGE(When Data Entered)

1. Optoelectronic Materials and Components

Minilaser development, diode pumps, KTN modulator program, coupling from laser to wave guide, feed materials for crystal growth.

2. Superconducting Transition Metal Alloys

Development of surfaces and tunneling barriers for A15 substrates.

3. Chemical Synthesis Using High Temperature Lithium Vapor Species

Initiation of program involving the Synthesis of polymers and diamond-like materials; problem of purification and separation of the novel polylithium compounds.

11  
SECURITY CLASSIFICATION OF THIS PAGE(When Data Entered)

For Period July 1, 1974 - December 31, 1974

Semi-Annual Technical Report #3

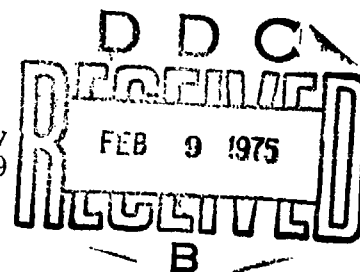
RESEARCH IN MATERIALS SCIENCE

Sponsored By  
Advanced Research Projects Agency  
Contract No. DAHC 15-73-C-0316

ARPA Order No.: 2469  
Program Code No.: 3D10

Contractor:  
Massachusetts Institute of Technology  
Cambridge, Massachusetts 02139

Principal Investigator:  
N. J. Grant (617) 253-5638



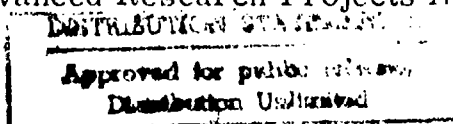
Project Scientists or Engineers:

- I Optoelectronic Materials and Components: Miniaturized Thin Film Laser Sources and Modulators. D. J. Epstein (617) 253-4676
- II Superconducting Transition Metal Alloys. R. M. Rose (617) 253-3230, M. MacVicar (617) 253-5617
- III Chemical Synthesis Using High Temperature Lithium Vapor Species. R. Lagow (617) 253-5617

Effective Date of Contract: June 1, 1973  
Contract Expiration Date: May 31, 1975  
Amount of Contract: \$770,233

The views and conclusions contained in this document are those of the authors and should not be interpreted as necessarily representing the official policies, either expressed or implied of the Advanced Research Projects Agency or the U. S. Government.

iii





SEMI-ANNUAL TECHNICAL REPORT NO.3

Period: July 1, 1974 - December 30, 1974

Title: Research in Materials Sciences

Project Title: Optoelectronic Materials and Components:  
Miniaturized Laser Sources and Thin Film  
Modulators

Contract Number: DAHC-15-73-C-0317

ARPA Order No.: 2469

Program Code No.: 3D10

Name of Contractor: Massachusetts Institute of Technology  
Cambridge, Massachusetts 02139

Principal Investigator: N. J. Grant, (617) 253-5638

Project Scientists or Engineers: D. J. Epstein - (617) 253-4676  
C. G. Fonstad - (617) 253-4634  
H. P. Jenssen - (617) 253-6873  
A. Linz - (617) 253-3208

Effective Date of Contract: June 1, 1973

Contract Expiration Date: May 31, 1975

Amount of Contract: \$770,233

Amount of Project: \$315,601

Sponsored by:

Advanced Research Projects Agency

ARPA Order No.2469

The views and conclusions contained in this document are those of the authors and should not be interpreted as necessarily representing the official policies, either expressed or implied, of the Advanced Research Projects Agency or the U.S. Government.

OPTOELECTRONIC MATERIALS AND COMPONENTS:  
MINIATURIZED LASERS AND THIN FILM MODULATORS

TABLE OF CONTENTS

	Page
I. SUMMARY	1
II. MINILASER DEVELOPMENT	4
2.1 Introduction	4
2.2 Energy Transfer Study in Sensitized Ho:YbLF	5
2.3 Oxide Hosts	13
III. DIODE PUMPS	18
3.1 Diode Pump Program Objectives	18
3.2 Diode Fabrication and Evaluation	19
3.3 Silicon-Doped Gallium Arsenide	27
3.4 Gallium Arsenide Antimonide	28
IV. KTN MODULATOR PROGRAM	36
4.1 Modulator Theory	36
4.2 Modulator Evaluation	38
4.3 Improvement of Performance	47
4.4 KTN Growth by Chemical Vapor Deposition	49
V. COUPLING FROM LASER TO WAVEGUIDE	50
5.1 Mode Control by Dielectric Cladding	53
5.2 General Considerations for the Grating Coupler	57
5.3 Tolerance in Grating Periodicity	62
5.4 Grating Fabrication	62

## TABLE OF CONTENTS (continued)

	Page
VI. PREPARATION OF FEED MATERIALS FOR CRYSTAL GROWTH	66
6.1 Clean Room	66
6.2 Chemicals: Purification and Synthesis of Oxide Feeds	66
6.3 Rare Earth Fluorides	73
6.4 Continuing Work	73
VII. SPECIAL FACILITIES AND STUDIES	75
7.1 Clean Oxide Crystal Growth Furnace	75
7.2 Refractive Index of $\text{LiYF}_4$	75
VIII. REFERENCES	80
IX. PUBLICATIONS AND PAPERS PRESENTED AT MEETINGS	81

OPTOELECTRONIC MATERIALS AND COMPONENTS;  
MINIATURIZED LASERS AND THIN FILM MODULATORS

I. SUMMARY

The research carried out under the subject contract has the following major objectives: (1) development of rare earth doped fluoride and oxide materials suitable for miniaturized optically pumped lasers; (2) development of LED pumps for these lasers; (3) growth and evaluation of electro-optical thin films suitable for optical modulators. Although the research is materials based, it is being carried out in a context which recognizes the interplay between materials development and device design.

The following listing summarizes our main achievements during the six month period covered by the present report.

1. The importance of upconversion processes in determining laser threshold has been demonstrated via a rate equation model applied to the system  $Tm^{3+}:Yb^{3+}$ . The rate equations are nonlinear and reveal undesirable saturation effects in energy level populations at the pump rates required for laser operation. The study shows that the type and concentration of sensitizer and activator ions must be chosen with extreme care if efficient laser operation is to be obtained. In particular, it becomes evident that  $Tm$  in moderate concentration will be required for the  $Ho:YLF$  minilaser.

(Section II)

2. Preliminary spectroscopic results on RE and Ni doped CAMGAR are presented and possible laser action in this crystal is discussed.

(Section II)

3. LED's fabricated from Si-doped GaAs are showing an external efficiency  $> 4\%$ . This value is higher than the 2.5% assumed in our original design calculations for minilaser pumps. An improved inverted

device structure, now being developed, will allow for better heat sinking and permit the use of higher current densities. The dependence of spectral output on current level is being studied. (Section III)

4. In the Ga(AaSb) system, emission matched to the Yb pump band has been obtained for the composition  $\text{GaAs}_{0.97}\text{Sb}_{0.03}$  doped with 0.1 at. % Si. The emission bandwidth is 25% narrower than for comparable GaAs diodes. Emission at  $1.06 \mu\text{m}$  has been obtained from  $\text{GaAs}_{0.93}\text{Sb}_{0.07}$  diodes grown from melts containing 1.1 at. % Si. Emission at longer wavelengths, to pump other absorption bands such as  $\text{Ni}^{2+}$  at  $1.2 \mu\text{m}$ , seems attainable in this material. (Section III)

5. A KTN thin film interdigital modulator has been fabricated and tested. Essentially full modulation is attained with a 15 volt drive. Preliminary measurements of frequency response show a relatively restricted bandwidth. Modifications in materials composition, growth procedure and device structure are being made with a view toward determining the parameters which limit device performance. (Section IV)

6. An experimental setup for measuring optical loss in waveguide films has been completed. Measurements on a KTN film, grown by liquid phase epitaxy, revealed the rather high loss of 28 db/cm. We intend to determine the extent to which optical attenuation is influenced by conditions of crystal growth. (Section IV)

7. Problems involved in coupling from the minilaser to a dielectric waveguide are being considered. Direct coupling can be achieved if the dielectric cavity has a sufficiently large index. However, the use of a high index material leads to an excessively large number of cavity modes; dielectric coatings on one or more cavity faces can be used to strip off unwanted modes to the point where the number of remaining modes becomes

arbitrarily small. When direct coupling fails a grating coupler can be used. (Section V)

8. A facility to produce gratings has been completed and a test grating has been made. (Section V)

9. Considerable effort has been made to develop chemical techniques for the preparation of high purity feed materials for the fluoride and oxide crystals needed for the minilaser program. Impurities can seriously reduce fluorescence lifetimes. (Section VI)

10. Now that high purity feeds are available it is important to have crystal growing furnaces which do not recontaminate the feed. A "clean" furnace for top-seeded solution growth of oxide crystals has been built and is now "on line". (Section VII)

11. The refractive index of YLF has been measured over the range of 0.225 - 2.6  $\mu$ m. Published values for the index, measured in the visible, appear to be in considerable error. (Section VII)

## II. MINILASER DEVELOPMENT

### 2.1 Introduction

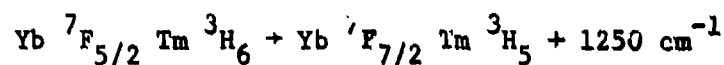
The concept of a light-emitting-diode pumped miniature crystal laser evolved from earlier successful work on the alphabet Ho:YLF laser. Pump-light is absorbed in the levels of  $\text{Er}^{3+}$  and  $\text{Tm}^{3+}$ , where the absorption coefficient is high owing to the high concentration of these ions, and the energy is then transferred to the upper level of the  $\text{Ho}^{3+}$  laser transition. Using as a pump a Kr-ion laser, matched to an absorption line in  $\text{Er}^{3+}$ , we have shown that a miniature laser of alphabet Ho:YLF can be operated at room temperature with pump power that can reasonably be expected from a GaAs light-emitting diode.<sup>(1)</sup> The alphabet Ho:YLF material used in these experiments had rare earth concentrations that had been found experimentally to be near optimum for pulsed laser rod operation. It was reasonable to believe that for cw operation the optimum concentrations might be different. Specifically, it was not clear if  $\text{Tm}^{3+}$  was necessary in addition to  $\text{Er}^{3+}$  as a sensitizer. However, it was found that Ho-doped  $\text{LiErF}_4$  did not lase even at 77°K.<sup>(1)</sup> In the present reporting period, energy transfer processes in the Ho:YLF have been investigated in more detail. Specifically, the system with  $\text{Yb}^{3+}$  as a sensitizer has been studied. This is an important sensitizer ion because it has an absorption band which can be matched to a 0.96  $\mu\text{m}$  LED pump.

In the following section the transfer processes between  $\text{Yb}^{3+}$  and  $\text{Tm}^{3+}$  in YLF are treated in detail. Based on the results, the possibility of a Ho laser sensitized by Yb and Tm is discussed. In the last section some preliminary spectroscopic results on rare earth and Ni doped CAMGAR are presented and possible laser action in this crystal is discussed.

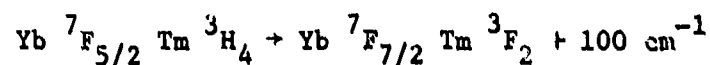
## 2.2 Energy Transfer Study in Sensitized Ho:YbLF

A successful Yb<sup>3+</sup> sensitized laser will require efficient energy transfer from Yb<sup>3+</sup> to the active ion (Ho<sup>3+</sup>, Er<sup>3+</sup>, or Tm<sup>3+</sup>). However, it is also known that Yb<sup>3+</sup> sensitized materials are excellent upconverter materials, that is, materials which absorb low energy photons and emit higher energy photons. It will be shown that upconversion processes can significantly reduce the efficiency of energy transfer from Yb<sup>3+</sup> to activator ions; furthermore, this effect may not be seen under the low intensity pumping used in spectroscopy experiments. Only under the intense pumping needed for laser operation will this reduction in transfer efficiency occur, and the laser will not work as predicted from conventional spectroscopy experiments. Rare earth concentrations must be optimized to reduce this effect.

The Tm<sup>3+</sup> doped LiYbF<sub>4</sub> system was chosen for first studies of the effect of upconversion because most of the transfer rates can be easily measured. The energy levels of Yb<sup>3+</sup> and Tm<sup>3+</sup> are shown in Fig. 2.1. The upconversion processes involve two energy transfer steps. The first is a non-resonant transfer



with the excess energy being taken by lattice phonons. The Tm<sup>3+</sup>:<sup>3</sup>H<sub>5</sub> rapidly decays to <sup>3</sup>H<sub>4</sub> by multiphonon decay. The second transfer is more nearly resonant



The <sup>3</sup>F<sub>2</sub> then decays rapidly to the <sup>3</sup>F<sub>4</sub>.

To study the populations in various excited levels and the transfer efficiencies, a simple rate equation model was used. The model in Fig. 2.2 shows the transfer processes considered. The populations of the



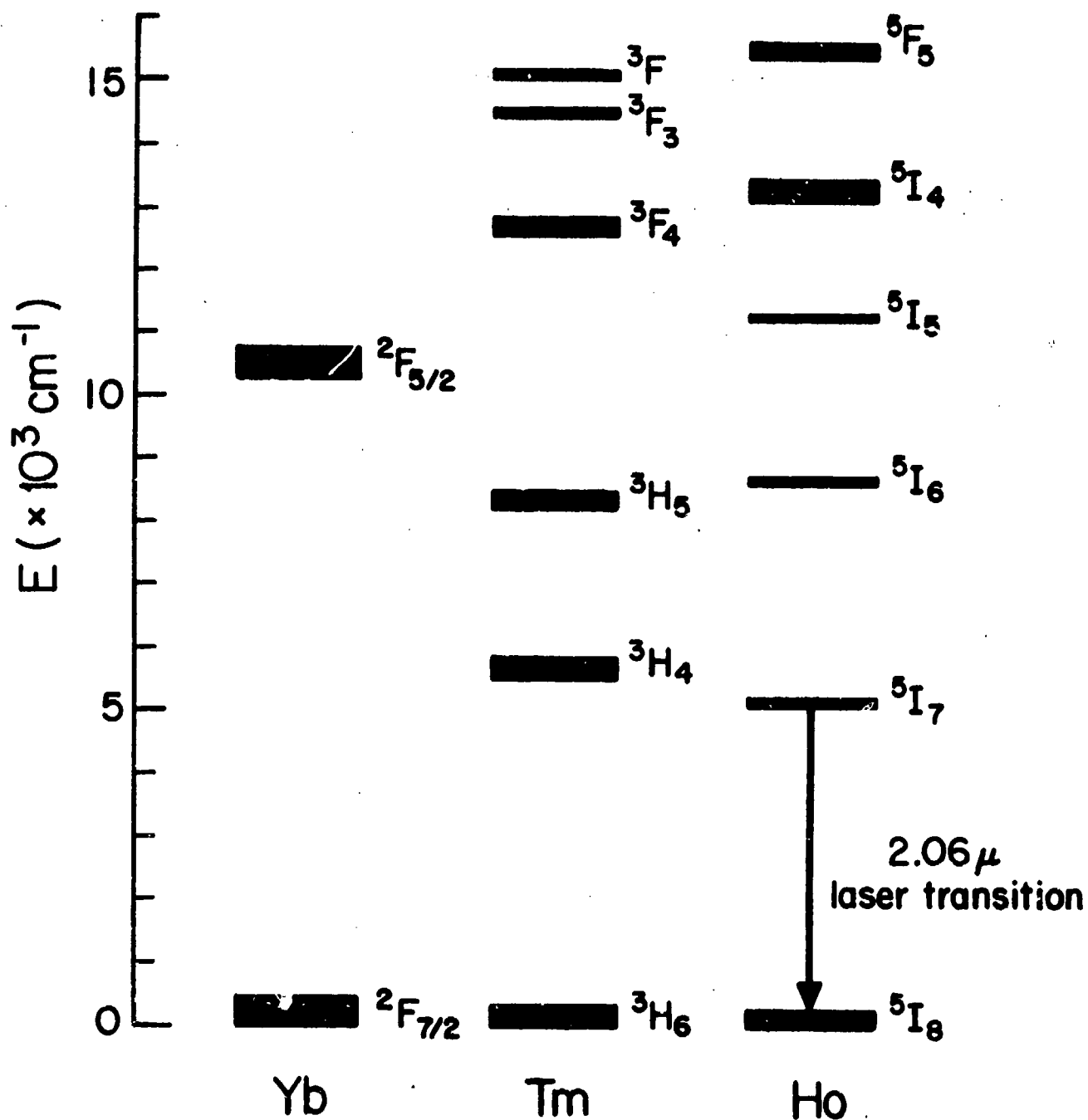
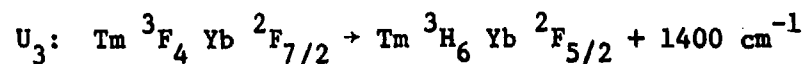
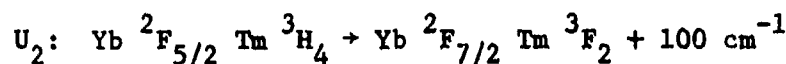
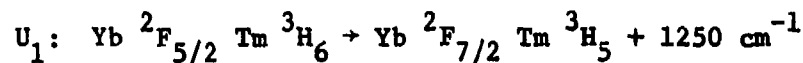


Fig. 2.1 Energy levels for the ions  $\text{Yb}^{3+}$ ,  $\text{Tm}^{3+}$ ,  $\text{Ho}^{3+}$ .

$i^{\text{th}}$  level of the activator ( $\text{Tm}^{3+}$ ) and the sensitizer ( $\text{Yb}^{3+}$ ) are denoted by  $A_i$  and  $S_i$ , respectively. The  $\text{Tm}^{3+} : {}^3\text{F}_2$ ,  ${}^3\text{F}_3$ , and  ${}^3\text{F}_4$  are labeled together as  $A_3$  since the  ${}^3\text{F}_2$  and  ${}^3\text{F}_3$  decay rapidly ( $< 10 \mu\text{s}$ ) to the  ${}^3\text{F}_4$ ; likewise, the  ${}^3\text{H}_5$  and  ${}^3\text{H}_4$  are labeled  $A_2$ . The transfer rate constants  $U_i$  are for the following processes:



With  $R_s$  defined as the inverse of the  $\text{Yb}^{3+} : {}^2\text{F}_{5/2}$  fluorescent lifetime and with  $R_2$  and  $R_3$  defined respectively as the fluorescent decay rates of the  $\text{Tm}^{3+} : {}^3\text{H}_4$  and  ${}^3\text{F}_4$  levels, the rate equations become:

$$\dot{S}_2 = X(S_1 - S_2) - U_1 A_1 S_2 - U_2 A_2 S_2 + U_3 A_3 S_1 - R_s S_2$$

$$\dot{A}_2 = U_1 A_1 S_2 - U_2 A_2 S_2 + 2U_4 A_1 A_3 - R_2 A_2$$

$$\dot{A}_3 = U_2 A_2 S_2 - U_3 A_3 S_1 - U_4 A_1 A_3 - R_3 A_3$$

The pump rate  $x = \sigma\Phi$ , where  $\sigma$  is the  $\text{Yb}^{3+} : {}^2\text{F}_{5/2}$  absorption cross section, and  $\Phi$  is the pump photon flux. The  $A_i$  and  $S_i$  are normalized such that

$$A_1 + A_2 + A_3 = C_{\text{Tm}},$$

where  $C_{\text{Tm}}$  is the fraction of  $\text{Yb}^{3+}$  sites occupied by  $\text{Tm}^{3+}$ . Therefore,

$$S_1 + S_2 = 1 - C_{\text{Tm}}.$$

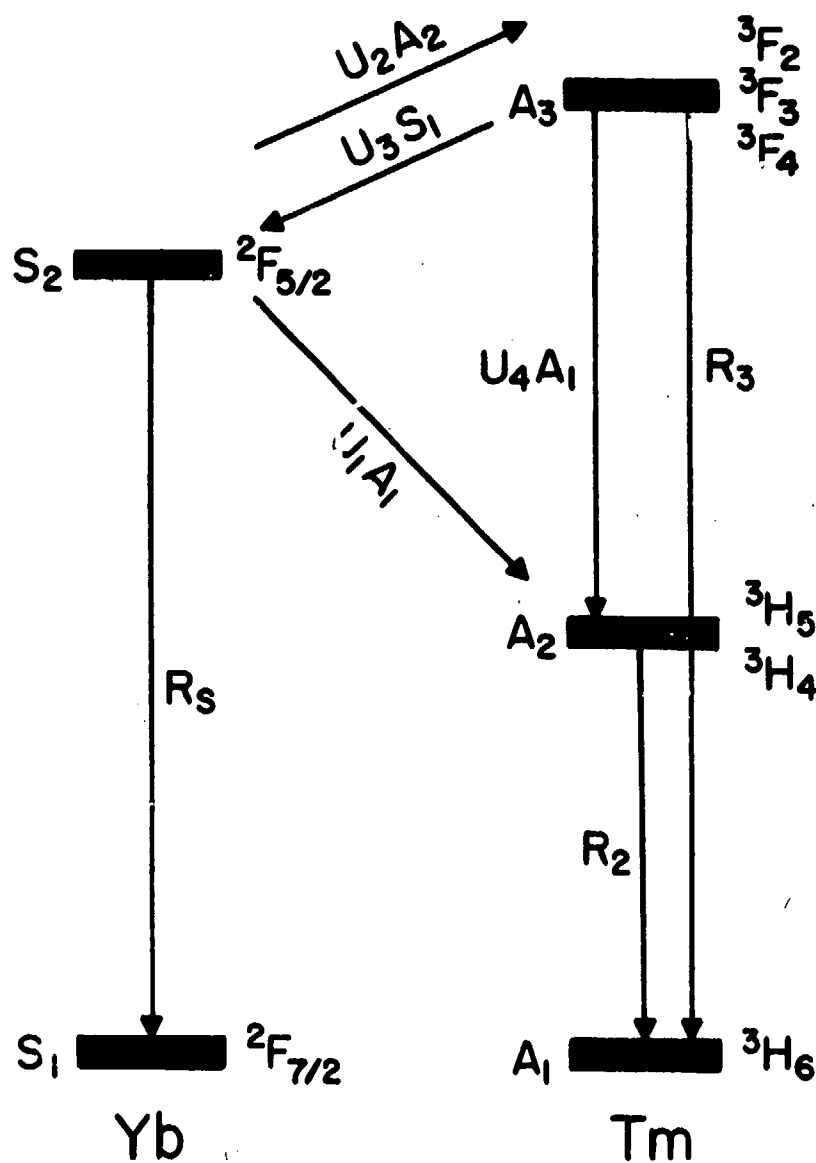


Fig. 2.2 Energy decay and transfer processes for the system  $\text{Yb}^{3+}$ - $\text{Tm}^{3+}$ .

The rate constants were measured by pulsed excitation in the following crystals:  $\text{LiYbF}_4$ ,  $\text{LiYb}_{0.995}\text{Tm}_{0.005}\text{F}_4$ ,  $\text{LiYb}_{0.9475}\text{Tm}_{0.05}\text{Ho}_{0.0025}\text{F}_4$  and  $\text{LiY}_{0.98}\text{Tm}_{0.02}\text{F}_4$ . The  $R_1$  were obtained from fluorescent lifetime measurements.  $U_1$  was obtained from the  $\text{Yb}^{3+}:^2\text{F}_{5/2}$  decay time and the  $\text{Tm}^{3+}:^3\text{H}_4$  build-up time in  $\text{LiYb}_{0.995}\text{Tm}_{0.005}\text{F}_4$ ; likewise,  $U_3$  was measured from the  $\text{Tm}^{3+}:^3\text{F}_4$  decay time.  $U_4$  was obtained from the concentration dependence of the  $^3\text{F}_4$  lifetime in the three Tm-doped crystals.  $U_2$  cannot be measured by simple pulsed excitation experiments, so the value used for this rate constant was one measured in  $\text{YF}_3$ .<sup>(2)</sup> The rate constants used in the model are:

	Rate ( $\text{sec}^{-1}$ )
$R_S$	394
$R_2$	85.5
$R_3$	770
$U_1$	$2.4 \times 10^5$
$U_2$	$1.4 \times 10^8$
$U_3$	$1.17 \times 10^4$
$U_4$	$10^6$

The three nonlinear coupled rate equations were numerically solved for the steady state values of  $S_2$ ,  $A_2$ , and  $A_3$ , for a wide range of pump rate  $X$ . The results are shown in Fig. 2.3 for Tm concentrations of 0.5% and 5%. At low pump rates ( $X \approx 10^{-5} \text{ sec}^{-1}$ )  $S_2$  and  $A_2$  increase linearly and  $A_3$  quadratically with pump rate; this is the regime in which most spectroscopy experiments are performed. Laser operation usually requires pump rates greater than  $X = 0.1 \text{ sec}^{-1}$ ; here, the populations begin to saturate, showing that laser materials which look good from spectroscopic

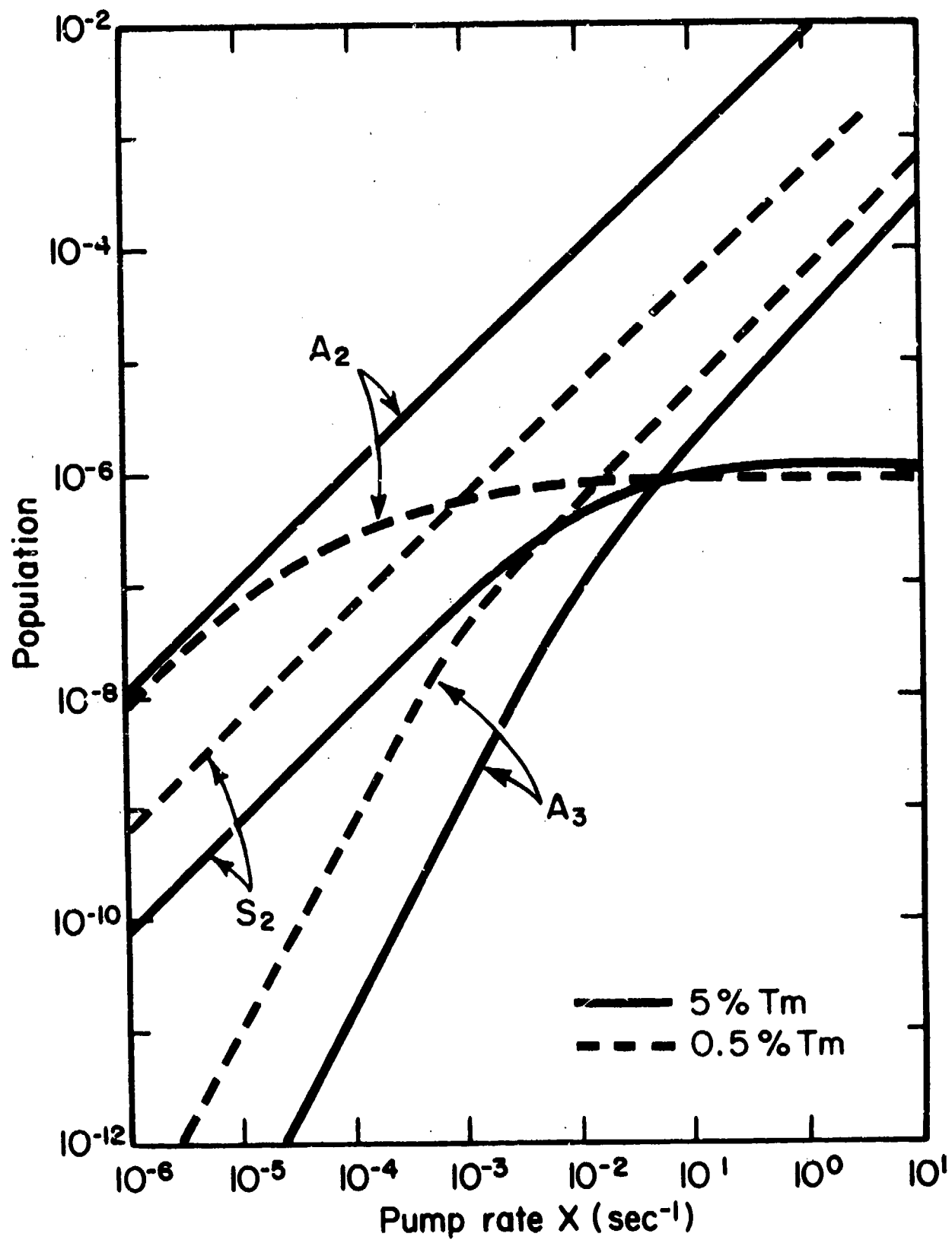


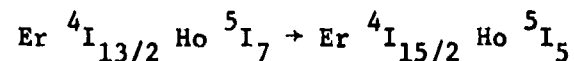
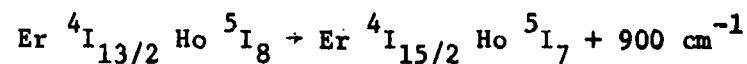
Fig. 2.3 Energy level populations as a function of pump rate.

measurements may behave very differently under laser pumping conditions.

The  $\text{Yb}^{3+}:^2\text{F}_{5/2}$  to  $\text{Tm}^{3+}:^3\text{H}_4$  transfer efficiency is shown in Fig. 2.4. A Yb-sensitized  $\text{Tm}^{3+}:^3\text{H}_4 \rightarrow ^3\text{H}_6$  laser would require low ( $< 0.5\%$ ) Tm concentration because it is a 3-level laser; however, Fig. 2.4 shows that transfer efficiency would be very small and this laser material would not work.

Some observations about a  $\text{Ho}^{3+}$  laser material, with composition  $\text{LiYbF}_4:5\% \text{ Tm}, 0.25\% \text{ Ho}$ , can be made from Fig. 2.4. It was shown in Semi-Annual Technical Report No.2 that the distributions of excitations in the  $\text{Ho}^{3+}:^5\text{I}_7 \rightarrow \text{Tm}^{3+}:^3\text{H}_4$  system are in thermal equilibrium, and with a Tm:Ho ratio of 20:1, half of the excited ions are Tm. Thus the addition of 0.25% Ho will not appreciably change the results of Fig. 2.4. For a pump rate of  $X = 0.2$ , the transfer efficiency from Yb to the  $^3\text{H}_4 - ^5\text{I}_7$  system is about 80%. A crystal of  $\text{LiYbF}_4:5\% \text{ Tm}, 0.25\% \text{ Ho}$  has been grown and laser tests will soon be made.

A similar upconversion process has been found to occur in  $\alpha\beta\text{-Ho}$  laser materials. For example, when a  $\text{LiErF}_4:0.3\% \text{ Ho}$  crystal is excited with  $1.5 \mu$  light, fluorescence is observed at  $1.2 \mu$ . The upconversion process is



The second transfer is resonant, and therefore occurs with a higher rate than the Yb-Tm upconversion transfer. A decrease in transfer efficiency at high pump rates like that in Fig. 2.4 is expected in this system. This may also explain why  $\text{LiErF}_4:0.3\% \text{ Ho}$  which, as spectroscopic experiments have shown, has efficient transfer at low pump rates, does not work as a

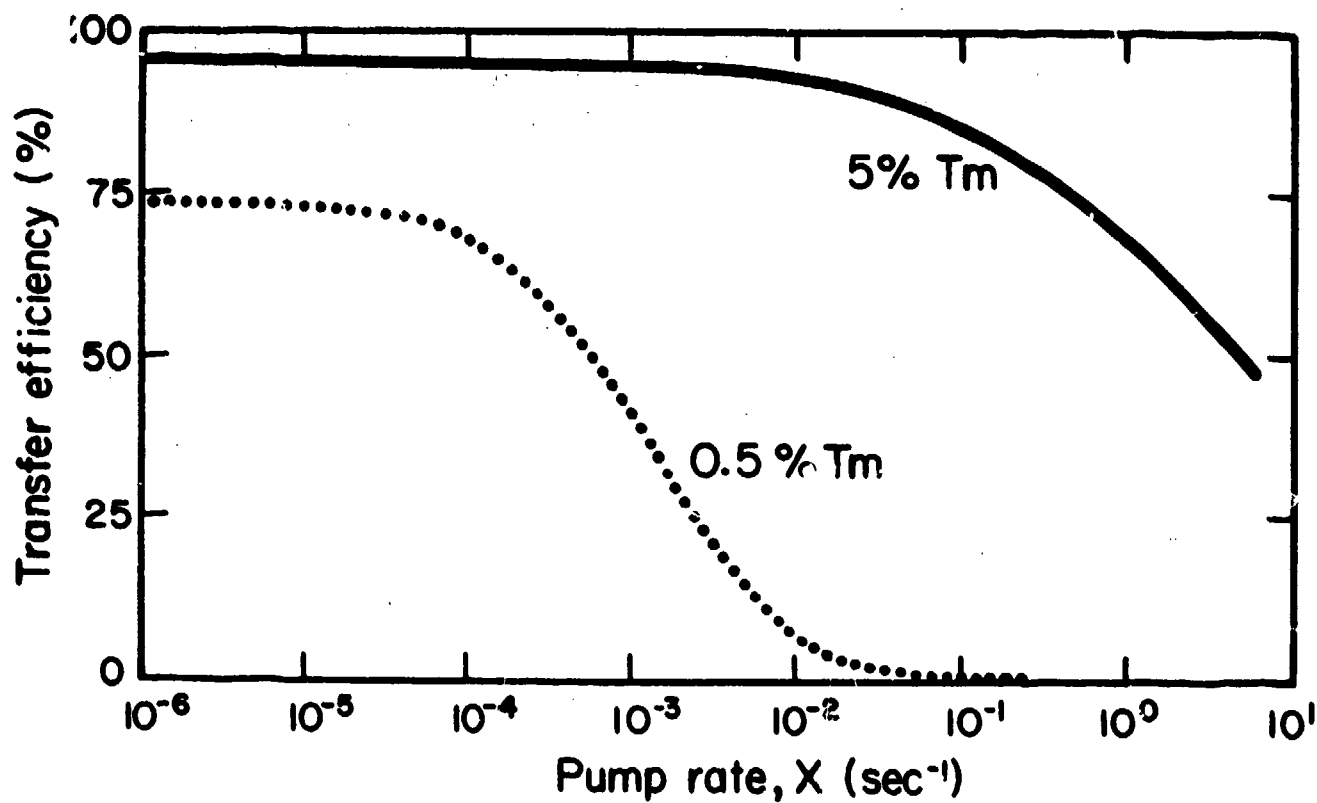
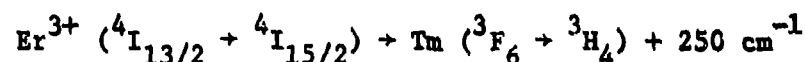


Fig. 2.4 Dependence of transfer efficiency on pump rate.

laser, yet  $\text{LiErF}_4$ :5% Tm, 0.3% Ho is a good laser material. The role of  $\text{Tm}^{3+}$  is to rapidly quench the  $\text{Er}^{3+}$ :  $^4\text{I}_{13/2}$  level



before the upconversion can take place.

### 2.3 Oxide Hosts

The upconversion problem discussed in the previous section was unforeseen and severely limits the possible combinations of sensitizers and activators in YLF as well as in other host crystals. The problem is basically that in the minilaser the inversion of the active ions is quite high and therefore transfer out of the upper laser level can be as fast as the transfer into that level. The upper laser level population can, therefore, be clamped at a level below that needed for threshold. This is what happens in the system containing  $\text{Er}^{3+}$  and  $\text{Ho}^{3+}$ . The transfer process  $\text{Er } ^4\text{I}_{13/2} \text{ Ho } ^5\text{I}_7 \rightarrow \text{Er } ^4\text{I}_{15/2} \text{ Ho } ^5\text{I}_5$  is resonant and therefore more efficient than  $\text{Er } ^4\text{I}_{13/2} \text{ Ho } ^5\text{I}_8 \rightarrow \text{Er } ^4\text{I}_{15/2} \text{ Ho } ^5\text{I}_7$ , which is the desired pumping transition. The addition of  $\text{Tm}^{3+}$  to this system prevents the unwanted upconversion process. Now the dominant transfer process is  $\text{Er } ^4\text{I}_{13/2} \text{ Tm } ^3\text{H}_6 \rightarrow \text{Er } ^4\text{I}_{15/2} \text{ Tm } ^3\text{H}_4$  and then  $\text{Tm } ^3\text{H}_4 \text{ Ho } ^5\text{I}_8 \rightarrow \text{Tm } ^3\text{H}_6 \text{ Ho } ^5\text{I}_7$ . Thus, in order to have an efficient sensitizer-activator system, there should not be any upconversion process that could be faster than the transfer process feeding the upper laser level. The energy transfer rate is dependent on the energy gap between initial and final state of the system. The smaller the gap the faster the rate. It is also dependent on the concentrations of both activator and sensitizer ions. Thus, in the previous example, the  $\text{Er } ^4\text{I}_{13/2} \text{ Tm } ^3\text{H}_6 \rightarrow \text{Er } ^4\text{I}_{15/2} \text{ Tm } ^3\text{H}_4$  is faster than  $\text{Er } ^4\text{I}_{13/2} \text{ Ho } ^5\text{I}_7 \rightarrow \text{Er } ^4\text{I}_{15/2} \text{ Ho } ^5\text{I}_5$  when the Tm concentration is larger



than the Ho concentration by about a factor of 10.

For the LED pumped minilasers,  $\text{Yb}^{3+}$  is a desirable sensitizer because the absorption band centered around  $0.95 \mu\text{m}$  can be matched to LED's that can be fabricated. Resonant or near resonant upconversion is present with either  $\text{Tm}^{3+}$ ,  $\text{Ho}^{3+}$ , or  $\text{Er}^{3+}$  as activator, and  $\text{Yb}^{3+}$  as sensitizer. If another ion can be added to the system to act as a bridge between Yb and the activator ion, as with Tm in the Er, Ho system, upconversion may not cause any problem. In the host crystal CAMGAR ( $\text{CaY}_2\text{Mg}_2\text{Ge}_3\text{O}_{12}$ ), rare earth ions can be substituted for  $\text{Y}^{3+}$ , and  $\text{Ni}^{2+}$  can be substituted for  $\text{Mg}^{2+}$  at a divalent octahedral site. Figure 2.5 shows absorption and emission of the first excited state of  $\text{Ni}^{2+}$  in CAMGAR at room temperature. The parent electronic transitions can not be seen even at  $77^\circ\text{K}$ . Only the vibronic sidebands are observed both in absorption and emission. The peak absorption cross section is about  $10^{-20} \text{ cm}^2$ , peak absorption coefficient is  $0.8 \text{ cm}^{-1}$  for 1 atomic percent  $\text{Ni}^{2+}$ . The fluorescent lifetime for  $\text{Ni}^{2+}$  was measured to be 2.5 ms for 1% Ni in  $\text{CaY}_{1.6}\text{Yb}_{0.4}\text{Mg}_2\text{Ge}_3\text{O}_{12}$ . In this crystal the Yb fluorescence was completely quenched by the Ni. It thus seems that  $\text{Ni}^{2+}$  could serve as a bridge between  $\text{Yb}^{3+}$  as sensitizer and  $\text{Tm}^{3+}$ ,  $\text{Ho}^{3+}$  as activators. Figure 2.6 shows the fluorescence from Yb:CAMGAR doped with 5% Ni and 0.25% Ho. The  $\text{Yb } ^2\text{F}_{5/2}$  level was pumped. It can be seen that the  $\text{Ni}^{2+}$  fluorescence is not completely quenched. The situation is similar to the  $\text{Er } ^4\text{I}_{12/2} \rightarrow \text{Ho } ^5\text{I}_7$  transfer. Thus it seems that the addition of  $\text{Tm}^{3+}$  will be necessary to increase the transfer rate from  $\text{Ni}^{2+}$  to  $\text{Ho } ^5\text{I}_7$ .

The Ni-doped CAMGAR is not limited to Yb as sensitizer and Ho as activator.  $\text{Ni}^{2+}$  itself can possibly be the active ion.  $\text{Ni:MgF}_2$  has previously been reported as a laser.<sup>(3)</sup>  $\text{Ni}^{2+}$ -sensitized  $\text{Tm}^{3+}$  is another

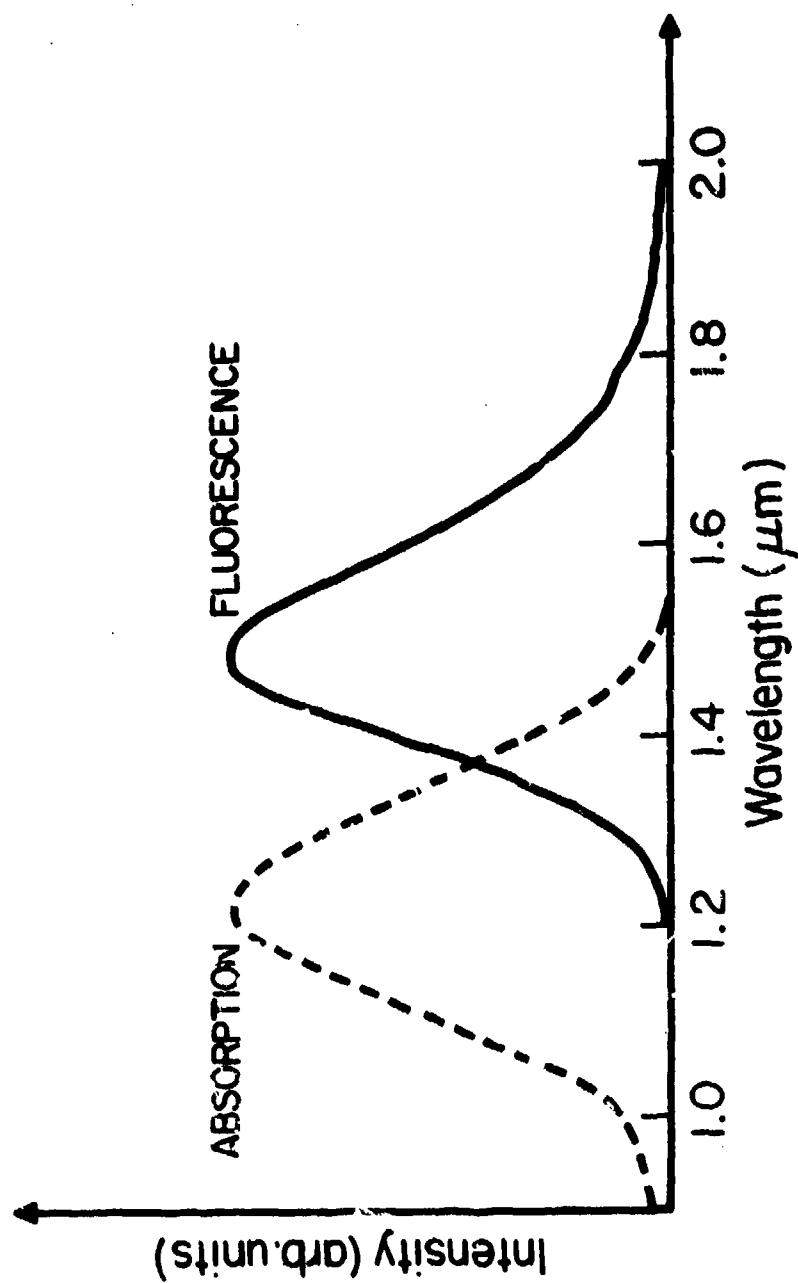


Fig. 2.5 Absorption and fluorescence of first excited state of  $K_1^{2+}$  in CAMGAR (at room temperature).

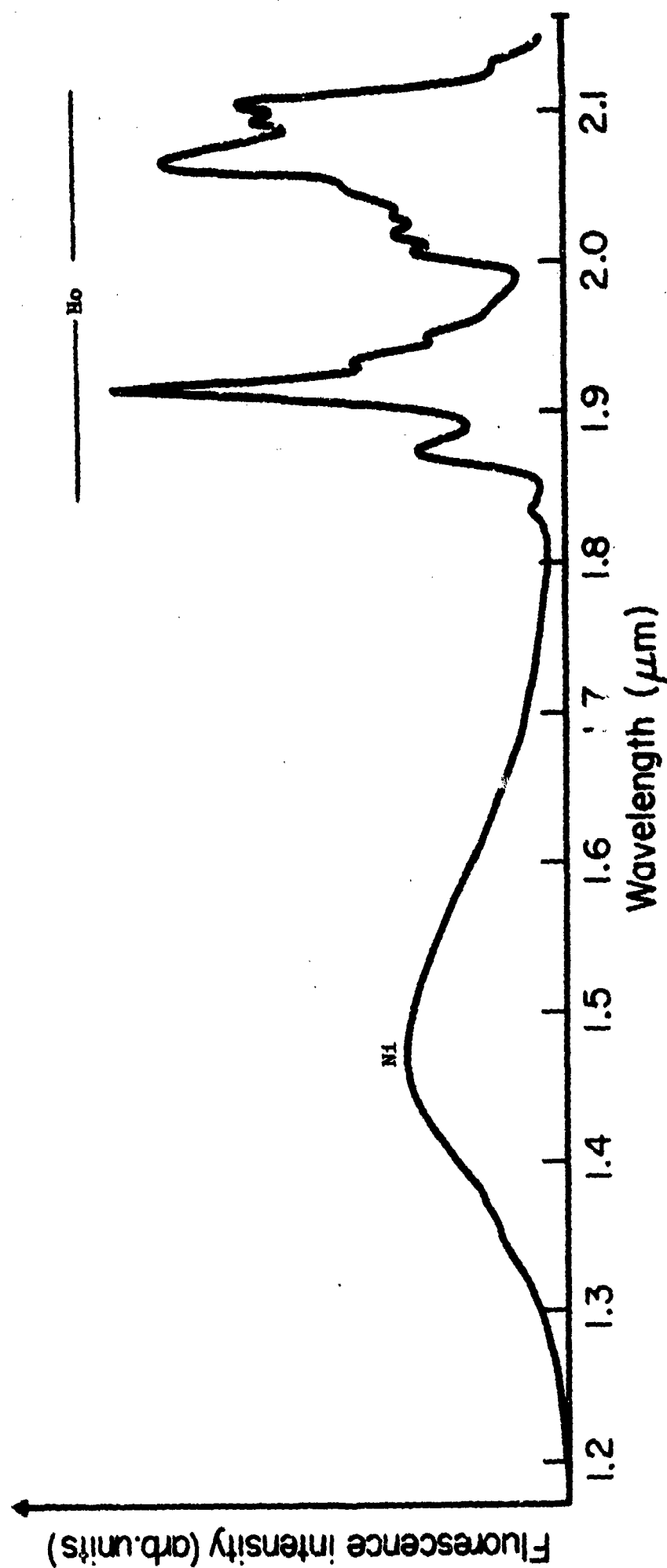


Fig. 2.6 Fluorescence from Yb:CaF<sub>2</sub> doped with 5% Nd, 0.25% Ho.

possibility.

Upconversion processes have not been studied in CAMGAR yet. Results similar to those found in YLF are expected, but energy gap dependence and concentration dependence of transfer rates will have to be measured.

The original alphabet Ho laser was first obtained with YAG as the host crystal. This laser never performed as expected at room temperature. The reason might be upconversion and it is now possible to determine whether this is so by the methods described in Section 2.2. Since YAG is one of the host crystals proposed for the LED-pumped minilaser, it is important to know if the high threshold for the Ho laser is a fundamental limit of that particular host crystal.

### III. DIODE PUMPS

#### 3.1 Diode Pump Program Objectives

The solid state minilaser excitation source, or pump, is to be a semiconductor light emitting diode designed specifically to pump the lasers already discussed. There are two distinct aspects to the development of such diodes: (1) the design of suitable device geometries, the development of fabrication procedures to produce them, and the evaluation of their performance, and (2) the tailoring through materials development efforts of the diode emission spectrum to optimally and adequately pump a laser absorption, or "pump", band.

Structurally, the diodes to be used will have planar emitting surfaces to which the lasers can be intimately attached, and will be designed to deliver the maximum amount of radiation into the laser rod. They will further be constructed so that the junction can be well heat-sunk to permit operation at high current levels,  $\sim 500 \text{ A/cm}^2$ .

Optimally matching the emission spectrum to the laser rod absorption band requires as narrow an emission band as practical peaking at the laser absorption maximum. To achieve this two approaches are being followed: (1) the use of silicon-doped gallium arsenide, GaAs, diodes, and (2) the use of silicon and/or zinc-doped gallium arsenide antimonide, Ga(As,Sb), diodes. Both systems, as is required, emit further into the infrared than do conventional zinc-doped GaAs LED's and each has its own particular advantages. The GaAs:Si system, for example, has been the subject of considerable study so that our work with it is as much development as research. We have consequently been concerned in this program with developing our own capability in growing the required diode layers,

with tailoring the pump diode emission spectrum, and with maximizing the emission intensity and overall pump efficiency. The Ga(As,Sb) system, on the other hand, is much more poorly understood and the work on this system is considerably more basic, starting with the determination of parameters in the growth system and the behavior of dopants in the alloy system.

To summarize, the diode minilaser pump program's two aspects in device design and materials development, are being addressed via three primary efforts, or thrusts: (1) the design, fabrication (including technology development), and evaluation of specialized diode geometries; (2) the growth, testing, and evaluation of Si-doped GaAs LED's with emission tailored to pump the Yb:YLF minilaser absorption band and with efficient, high intensity output; and (3) the growth and characterization of Si doped GaAsSb LED's in order to fully understand this system and evaluate it for ultimate use in the pump diodes. Initial pump diodes and minilaser-diode structures will evolve from a combination of the results of efforts 1 and 2 above. Future structures will involve more sophisticated, heterostructure diode geometries and materials developed in the third effort. In the following sections we will summarize progress in each of these areas during the last six month period.

### 3.2 Diode Fabrication and Evaluation

Device development efforts have concentrated on the pump diode geometry illustrated in Figure 3.1. This device is designed to side pump square cross-section "ring," or internal reflection mode lasers. The fabrication sequence for this device is illustrated in Figure 3.2. Development of the techniques necessary to produce the diodes has now

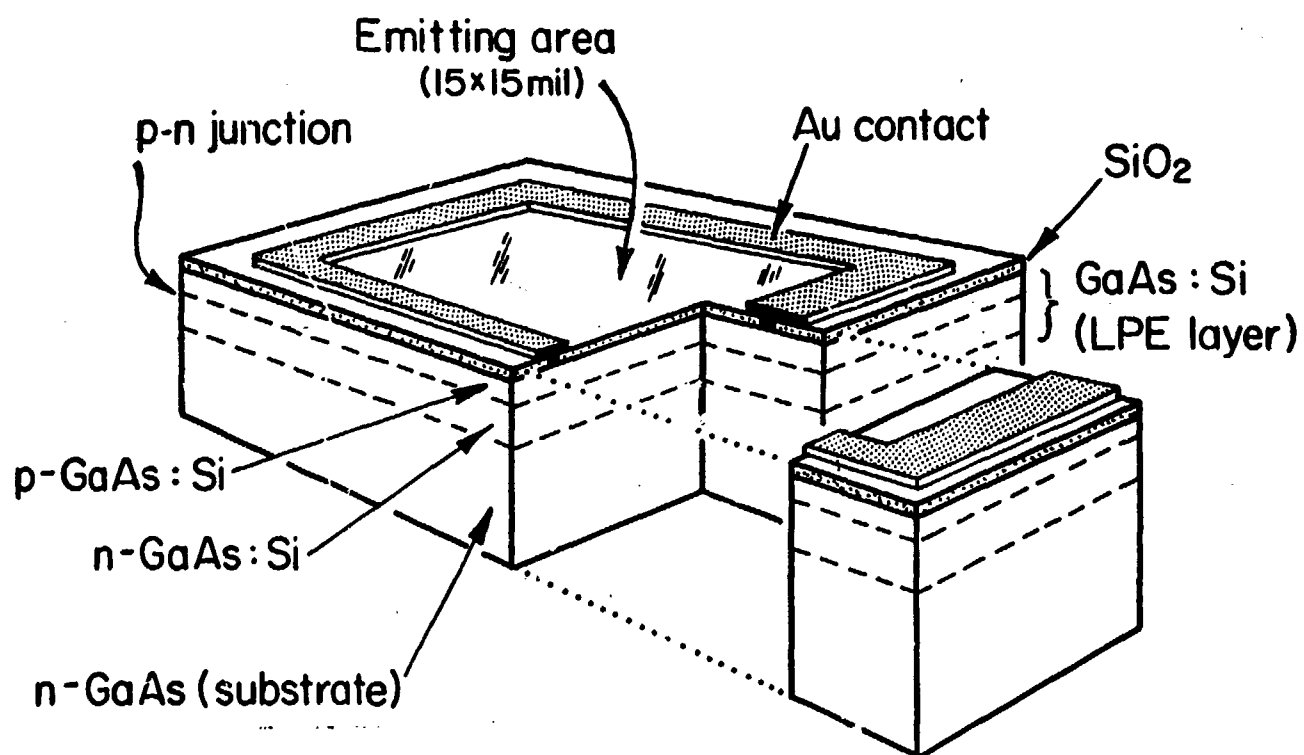
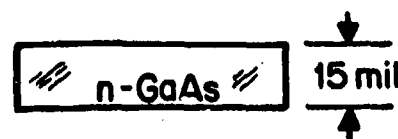
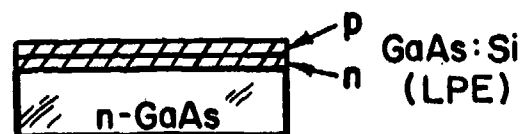


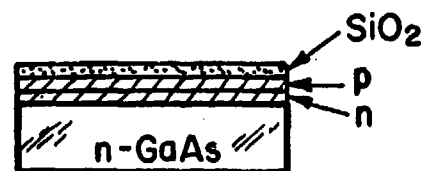
FIGURE 3.1. An artist's conception cut-away view of the pump diode to be used to side pump internal reflection mode lasers.



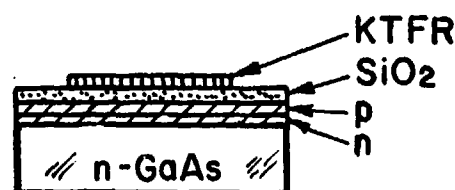
Substrate n-GaAs



Diode layers epitaxially grown



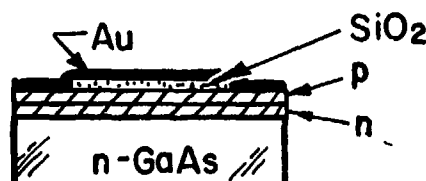
Deposited silicon dioxide mask  
3500 Å



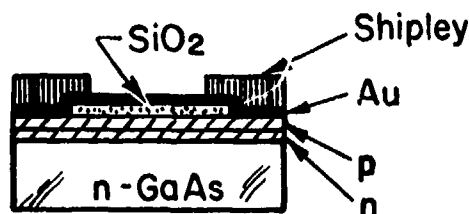
KTFR Photoresist mask, spun-on and developed



Silicon dioxide mask pattern etched and KTFR mask removed



Gold (Au) vapor deposited over entire surface 3000 Å



Shipley photoresist mask, spun-on and developed



Gold contact etched and Shipley photoresist removed

FIGURE 3.2. The sequence of steps in the fabrication of the pump diode illustrated in the previous figure, Figure 3.1.

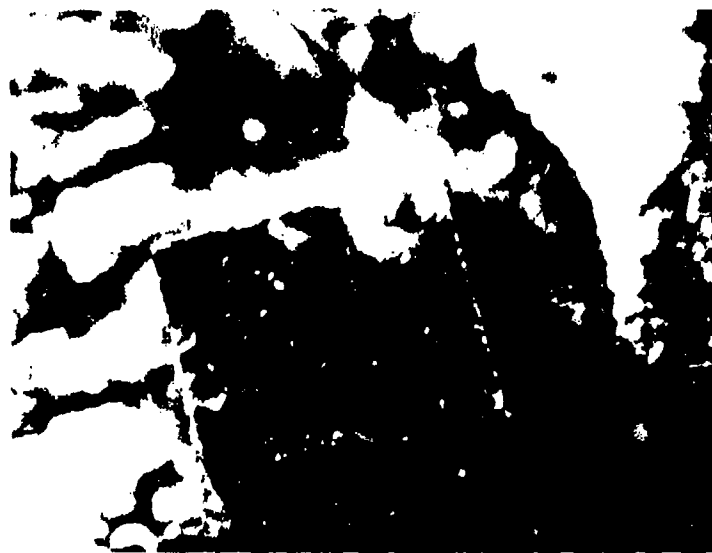


been completed, and they are being fabricated routinely. An ordinary microphotograph of a typical device is shown in Figure 3.3a; Figure 3.3b shows the same device viewed under an infrared microscope with a current through it of 60 mA. (The center emitting area is approximately  $1.5 \times 10^{-3} \text{ cm}^2$ ; the current density is  $\sim 20 \text{ A/cm}^2$ .)

In evaluating the above diodes, problems have been encountered with excessive heating at high current densities,  $> 100 \text{ A/cm}^2$ . Two corrective measures are being taken. The first is to use a more suitable package to mount the diodes. The TO-5 transistor headers used originally can only be poorly heat-sunk and have been replaced by a coined eyelet header, TO-39. The second is to fabricate the diode structure with the epitaxial layers on the bottom rather than on the top. That is, in Figure 3.2, after the diode layers are epitaxially grown (the second step) the wafer is inverted and then the processing continues as illustrated but with the patterned  $\text{SiO}_2$  and Au layers being generated on the substrate side rather than on the epitaxial layers. This relatively simple change has some significant advantages and costs little in increased fabrication complexity. As for advantages, it will mean that the entire p-layer surface will be contacted rather than just a thin ring (this side is soldered to the device header) which will lower the contact resistance and also eliminate the problem of spreading resistance\* in the thin p-type epi-layer. Furthermore, the junction region which is where the heat is generated and which it is important to

---

\*This is the problem of the voltage drop due to current flowing from the contact at the edge of the emitting area to points near the center of the emitting area keeping the diode from turning on in the center and leading to non-uniform emission across the emission area.



Reproduced from  
best available copy.

a



b

FIGURE 3.3. Photomicrographs of a device like that illustrated in Figure 3.1. a) Viewed through an ordinary microscope. b) Viewed through an infrared microscope. The contact in this particular device has been damaged by previous testing and is not typical.

keep cool, is now much closer to the heat sink, i.e. the header. Typically the substrate is close to 10 mils thick and the p-type epi-layer is 0.5-1.0 mils thick. This decrease of an order of magnitude or more in the thickness of GaAs between the junction and the header is expected to significantly improve the heat sinking and the high current density performance.

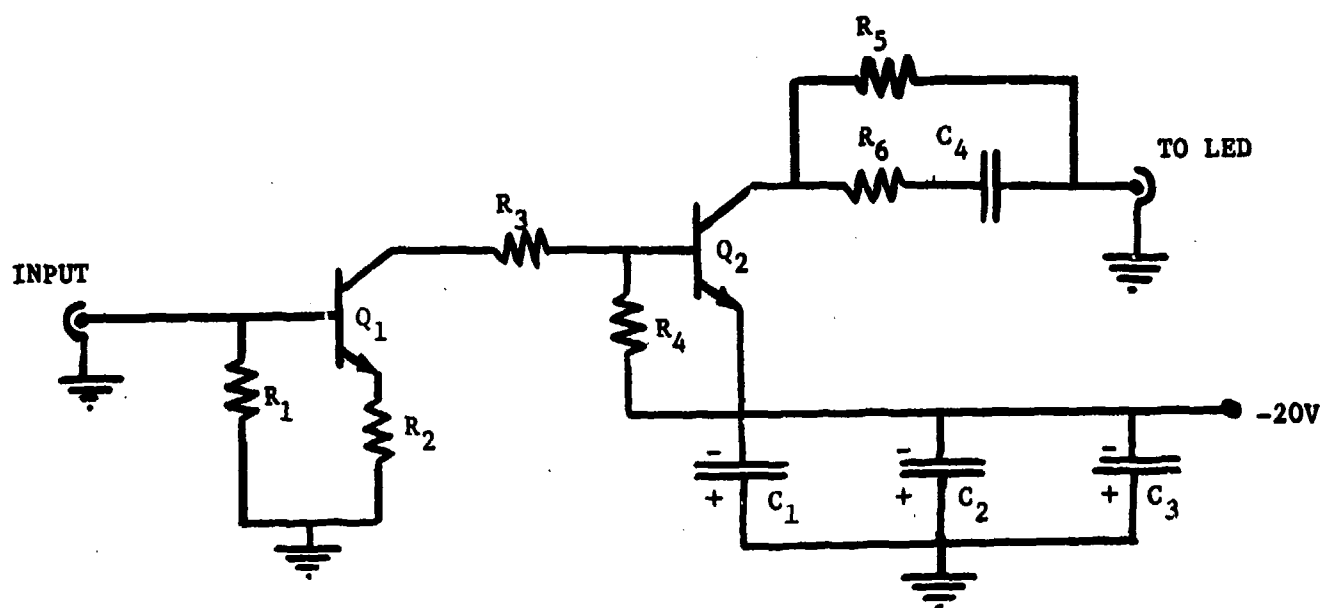
The only problem with the inverted structure appears to be avoiding shorting the junction when soldering the device to the header. This is mainly a question of care being taken during assembly, coupled with suitable mounting techniques. We are currently fabricating our first inverted devices and expect to begin testing some shortly. It is anticipated after experience is gained with these first devices, that the top surface contact pattern will be modified. The problem of spreading resistance is much less severe in the inverted structure because, in the converse of the situation for heat sinking, the layer in which the current must spread is now 10 mils thick rather than 0.5-1.0 mils thick.

With the progress in areas of fabrication (and growth, as well-- see the following sections) attention has been given to evaluating devices. Two systems are being developed: one is an instrument with which the emission pattern of diodes can be measured and the total emission and/or its spatial distribution can be determined. The other is a high current, variable duty cycle, frequency, and output diode pulser to be used to measure emission intensity, spectra, and uniformity across the emitting region at high current densities in the absence of heating effects.

The schematic of the pulse amplifier we have built is shown in Figure 3.4. It is capable of 10 Amp pulses and has a 10 nsec response time. The pulse frequency, duty cycle, and shape are determined within the constraints set by the amplifier response time by the pulse generator connected to the input. Initial results of measurements of the emission intensity at high current levels under pulsed conditions indicate that there is no saturation of the light output at least to 500 A/cm<sup>2</sup>.

The emission intensity perpendicular to the face of a typical diode has been measured to be 10 μW/cm<sup>2</sup> at a distance of 6.5 cm with a current of 50 mA (10 A/cm<sup>2</sup>). The total emitting surface area was 3.8x10<sup>-3</sup> cm<sup>2</sup>. To appreciate this result we can consider the following argument. Consider a window 1 cm x 1 cm at 6.5 cm distance from the diode. There will be 10 μW of power emitted through this opening. If we trace this power back to the diode junction we realize that because of the higher index of refraction of GaAs,  $n \approx 3.6$  vs 1.0 for air, the light has diverged in passing from GaAs to air. If it had not, these 10 μW would have been concentrated into a square 0.28 cm on a side and the power density at 6.5 cm would be 130 μW/cm<sup>2</sup>. Thus at the junction light is being emitted in all directions corresponding to an intensity at 6.5 cm of 130 μW/cm<sup>2</sup> or 5.5 mW/steradian. Actually it is even higher than this because the normal transmission going from GaAs to air is only 68%. Taking this into account we have 8 mW/steradian.

So far we have assumed that only light originally directed upward is observed. If light directed downward undergoes 100% reflection off the bottom contact, the above number will be halved to 40 mW/steradian.



Component identification:	$R_{1,2}$	47 $\Omega$ , 1/2 W	$C_1$	0.1 $\mu\text{F}$ , disc
	$R_3$	100 $\Omega$ , 1/2 W	$C_2$	50 $\mu\text{F}$
	$R_4$	390 $\Omega$ , 1/2 W	$C_3$	0.01 $\mu\text{F}$ , paper
	$R_5$	4.57 $\Omega$ , 2 W	$C_4$	0.0018 $\mu\text{F}$ , disc
	$R_6$	5.6 $\Omega$ , 1/2 W		
	$Q_1$	2N5160 (Motorola)		
	$Q_2$	2N4431 (TRW)		

FIGURE 3.4. Electrical schematic of the high current, fast rise-time pulse amplifier used to test diodes at high current densities.

There are  $4\pi$  steradians in a sphere so the total emission at the junction is  $4\pi \times 4 \text{ mW} \approx 50 \text{ mW}$ . The diode current is 50 mA and the voltage drop is 1.24 V implying a power input of 62 mW, and an internal efficiency approaching 100%. Note that we said the output was doubled by light reflected off the back contact, but that we neglected light scattered upwards after suffering higher order internal reflections. We can conclude from our arguments that the diodes are very efficient for practical purposes, i.e. as far as the light out the top surface is concerned, having nearly 100% internal efficiency.

While high internal efficiency is significant and necessary, the number of ultimate interest is the power density emitted from the emitting area into a laser diode. Referring back to the feasibility arguments made in the original proposals for this work, we find that they are based on assuming 50% internal efficiency and 60% reflection off the back contact. The present results indicate that we exceed both of these estimates and should be well within our original design objectives. Direct confirmation of this will be obtained from the measurement of the spatial distribution of the emission mentioned above. If, however, we say that the emission is uniform over the hemisphere, we have  $10 \text{ } \mu\text{W}/\text{cm}^2 \times 2\pi (6.5 \text{ cm})^2 \approx 2.5 \text{ mW}$  emitted or an external efficiency of 4%. Our feasibility arguments involved a figure of 2.5% and again are seen to have been conservative as we had claimed.

### 3.3 Silicon-Doped Gallium Arsenide

The optimum silicon doping level in gallium arsenide has previously been determined to be 1.4 at % Si in the melt. Layers of this composition are being grown regularly for use in fabricating pump diodes (see the previous section). During these growths minor improvements are

made in the growth procedures but the growth is largely routine. For a description of the growth philosophy and illustrations of the growth system and technique the reader is referred to prior semi-annual technical reports and proposals. A curve of the emission spectrum of a GaAs:Si diode grown from a melt containing 1.4 atomic % Si is found in Figure 3.6 in conjunction with the discussion in the following section.

### 3.4 Gallium Arsenide Antimonide

The study of Ga(As,Sb) as an alternative to GaAs as the pump diode material has of necessity been largely concerned with characterization of the growth system and of the diode emission spectra. A potential source of problems in the liquid phase epitaxy growth of Ga(As,Sb) is the very small distribution coefficient of antimony. This can be seen from the table below which gives typical melt compositions for the growth of GaAs, GaAs<sub>0.97</sub>Sb<sub>0.03</sub>, and GaAs<sub>0.93</sub>Sb<sub>0.07</sub>. The implication is that constitutional supercooling is increasingly a problem as the antimony concentration is raised. To avoid constitutional supercooling effects we use a mild vertical temperature gradient ( $\approx 1^\circ\text{C}/\text{cm}$  at the melt-substrate interface), a very slow growth rate (5  $\mu\text{m}/\text{hr}$ ) and a small cooling range (about  $7^\circ\text{C}$ ). For 7% Sb growth it now appears that an even slower growth rate would be advantageous.

	$T_{\text{tilt}} (^\circ\text{C})$	Ga	As	Sb
GaAs	880	95.1	4.9	--
GaAs <sub>0.97</sub> Sb <sub>0.03</sub>	880	80.4	4.6	15.0
GaAs <sub>0.93</sub> Sb <sub>0.07</sub>	860	72.6	3.9	23.5

Typical Melt Compositions (Atomic Percent)

Table 3.1

One of the important parameters is the transition temperature, that is, the temperature at which Si switches from a net n-type to a net p-type dopant. This temperature has been determined for alloy compositions containing 3% and 7% Sb and for from 0.1 to 1.4 atomic % Si in the melt. The results are presented in Figure 3.5.

Simple test diodes are fabricated from epitaxial layers and the emission spectra, particularly the peak wavelength and halfwidth, are measured. We have observed emission peaking at from 0.96  $\mu\text{m}$  for a 3% Sb alloy, 0.1 atomic percent Si in the melt, to 1.06  $\mu\text{m}$  for 7% Sb, 1.1 at. % in the melt. The former composition matches well the solid state laser pump band as illustrated in Figure 3.6. The latter is of interest for fiber optics communication because optical fibers have an absorption minimum at approximately 1.06  $\mu\text{m}$ . The emission spectrum of this device is shown in Figure 3.7.

The argument for using GaAsSb was that at a given wavelength the emission linewidth would be less because less Si would be needed. That this is indeed the case can be seen by referring to Figure 3.6. The emission of GaAs and  $\text{GaAs}_{0.97}\text{Sb}_{0.03}$  are compared and one finds the Ga(As,Sb) peak is 25% more narrow. The same result holds at other wavelengths as well; see Figure 3.8. In general the linewidth in Ga(As,Sb) is greater for a given Si doping level than in GaAs, see Figure 3.9, but is narrower at a given peak wavelength. The halfwidth at 1.06  $\mu\text{m}$  of 700 nm compares very well to (In,Ga)As diodes emitting at this wavelength.

A significant by-product of this research has been the demonstration of relatively narrow emission at 1.06  $\mu\text{m}$  in  $\text{GaAs}_{0.93}\text{Sb}_{0.07}$  (1.4 at. % Si); see Figure 3.7. Compared to other possible sources, this emission



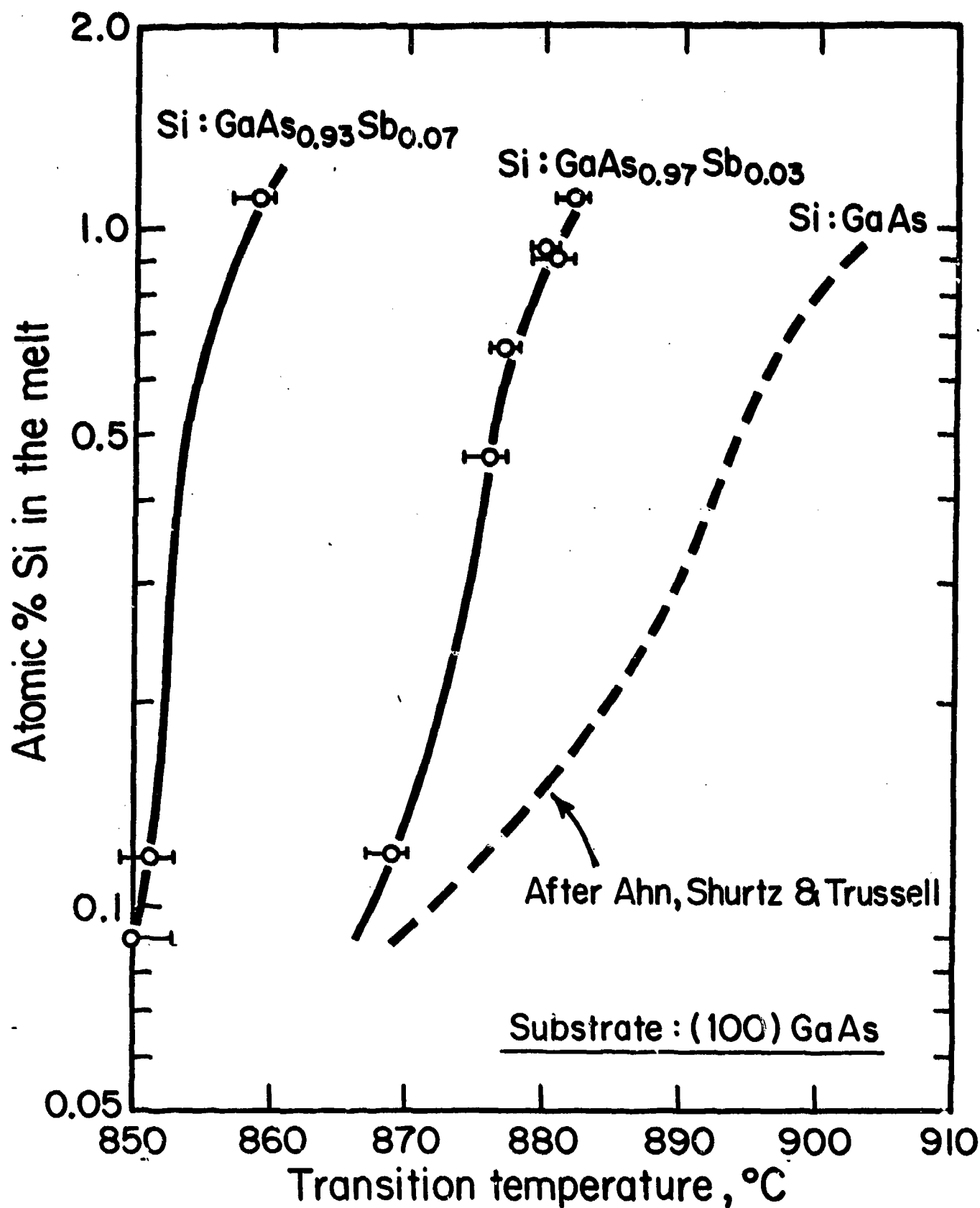


FIGURE 3.5. The n-type to p-type transition temperature associated with the amphoteric dopant silicon in GaAs<sub>1-x</sub>Sb<sub>x</sub>,  $x = 0.0, 0.03$ , and  $0.07$ , for up to 1.4 atomic percent silicon in the melt.

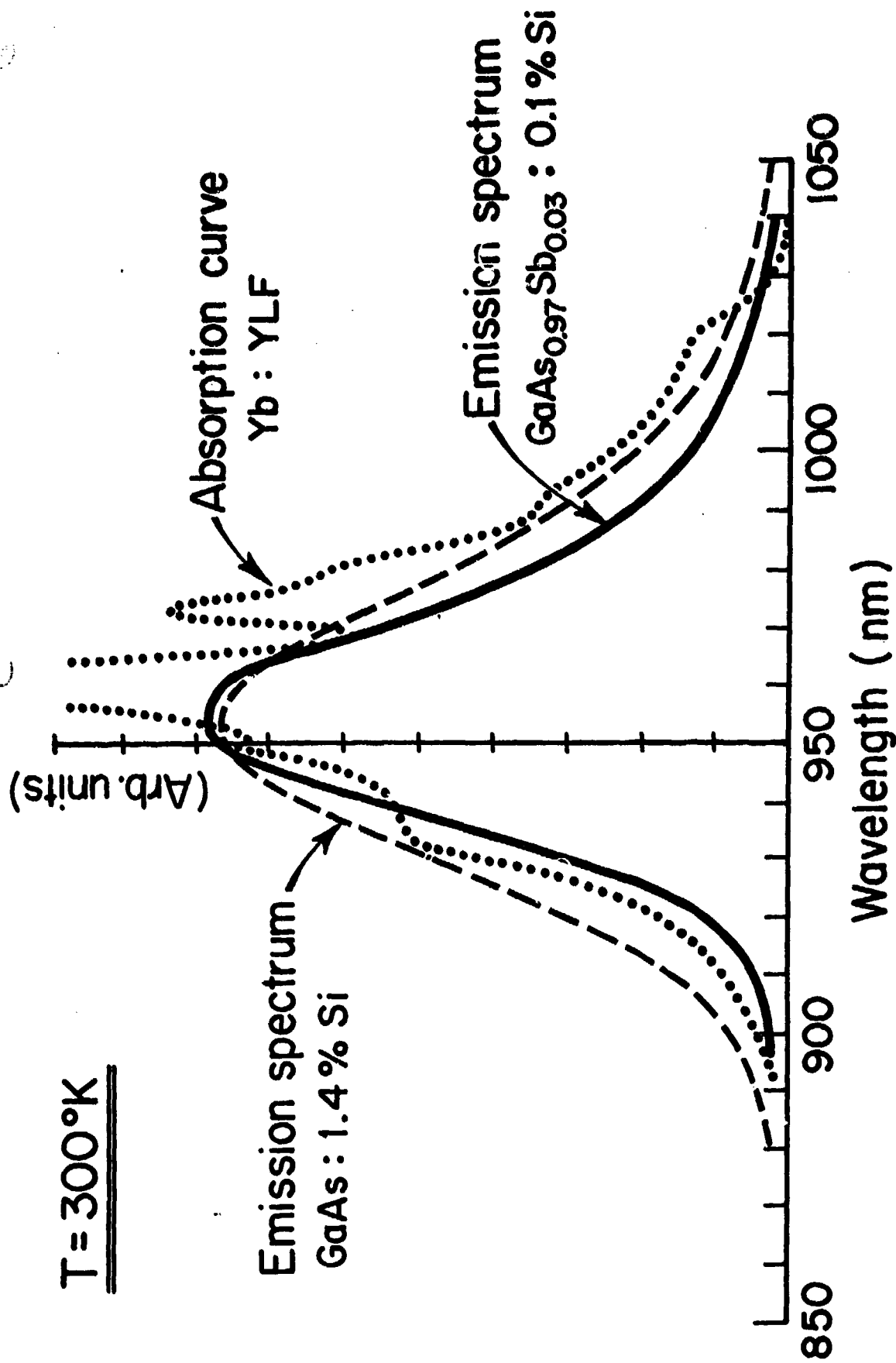


FIGURE 3.6. A comparison of the Yb absorption spectrum with the emission spectra of GaAs:Si and Ga(As,Sb):Si LED's grown in this program. The emission curves have been adjusted to have the same peak value; the absorption spectrum curve is absorption coefficient, arbitrary units.

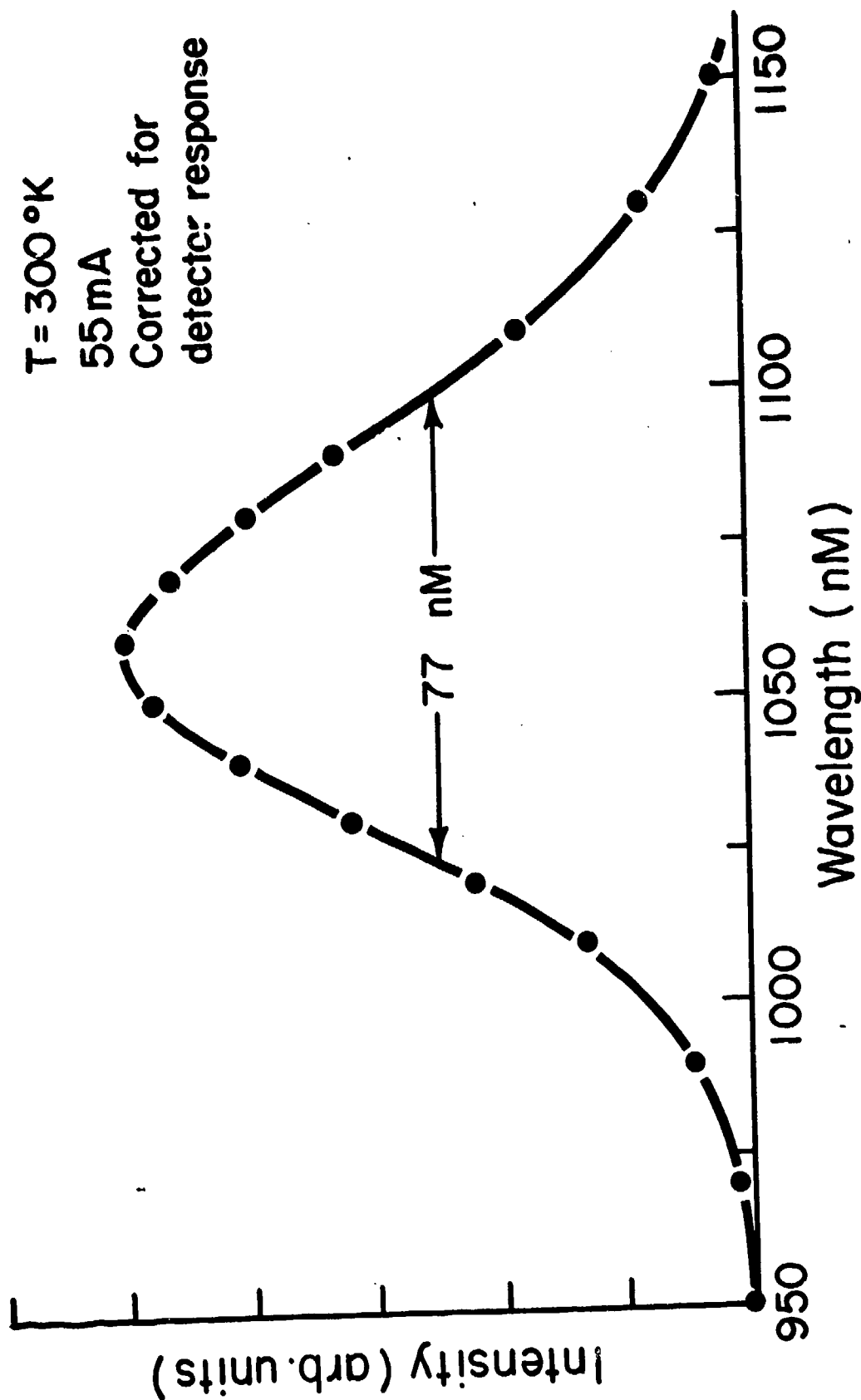


FIGURE 3.7. Emission spectrum of a Ga(As,Sb):Si device grown with 7% Sb in the alloy from a melt containing 1.1 atomic percent Si. The curve is corrected for detector response and shows a peak emission at  $1.06\text{ }\mu\text{m}$ .

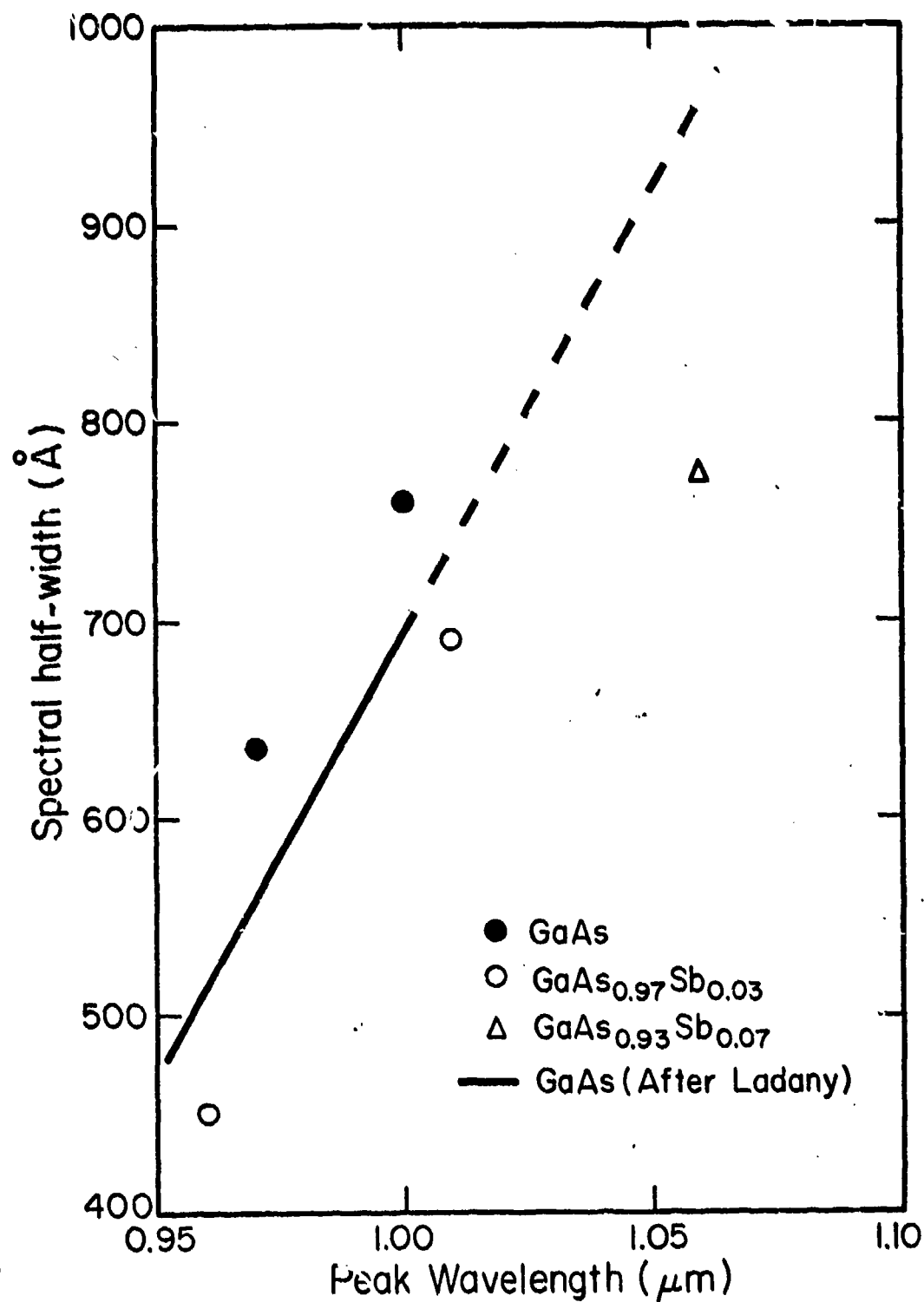


FIGURE 3.8. Emission linewidth (half-width) as a function of peak wavelength.

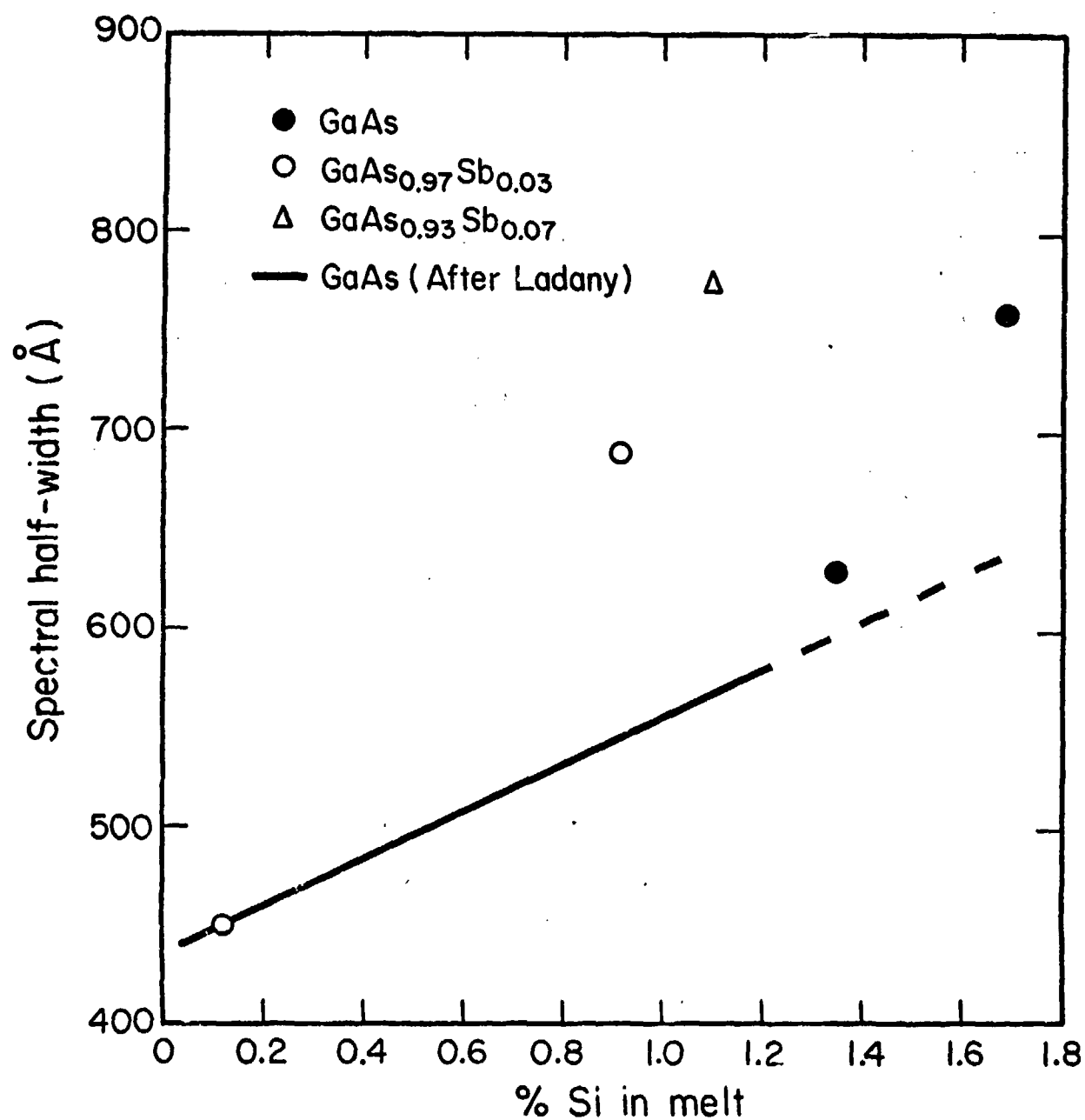


FIGURE 3.9. Emission linewidth as a function of atomic percent of silicon in the melt.

is much narrower than that of InP, and comparable to (In,Ga)As. With (In,Ga)As, however, zinc has been used as a dopant and an alloy with 15% In must be used. To grow this on GaAs substrates requires a very complicated layered grading, i.e. layers of 3% In, 7% In, and 12% In, for example, between the diode layers with 15% In, and the substrate. Our diodes are single step growths with the p-n junction being grown in (recall the amphoteric behavior of silicon).

Current work on Ga(As,Sb) concerns improving the growth technique and further evaluation of test diodes. Of particular interest is a measurement of the external efficiency of the diodes.

#### IV. KTN MODULATOR PROGRAM

Work on the modulator program, during the reporting period, has concentrated on the fabrication and evaluation of a prototype KTN thin film modulator. In this section we report on the operating characteristics of this modulator and outline several approaches for improved device performance; these include modification in crystal composition to obtain higher electro-optical coefficients, and changes in LPE growth procedures to improve film quality. We also report on our continuing effort to grow KTN by the method of chemical vapor deposition (CVD). Because we are obtaining useful films by LPE, the CVD program has lower priority at the moment.

##### 4.1 Modulator Theory

Thin film modulators, which employ the principle of light diffraction, require a periodic index of refraction variation in the waveguide transverse to the propagation direction of the guided mode. The periodicity can be obtained "mechanically" by propagating an ultrasonic wave across the beam, or electrically by using a pair of interdigital electrodes deposited on the surface of an electro-optic film. Our work has been with the latter type of modulator. Device performance is determined by the electro-optical properties of the film and by geometric parameters: electrode length,  $W$ ; center-to-center finger separation,  $2D$ ; finger width,  $L$ ; and number of fingers,  $N$ . For our prototype modulator, these parameters were  $N = 3$  mm,  $L = D = 25$   $\mu$ m,  $N = 18$ .

The diffraction theory associated with acousto-optic modulation<sup>4</sup> has been successfully applied to thin film electro-optic modulators. Depending on the period of the index variation and the wavelength of the guide mode, there are two domains of behavior, defined by the value of the coupling

factor

$$Q = \left(\frac{2\pi}{A}\right)^2 W / \left(\frac{2\pi}{\lambda_0}\right) N_m \quad (4.1)$$

where  $\lambda_0$  is the free space wavelength,  $N_m$  is the effective mode index, and  $A$  is either the center-to-center finger spacing of the electrode for materials with a quadratic electro-optic effect or twice this value for materials possessing a linear electro-optic effect. For  $Q \ll 1$ , Raman-Nath diffraction, characterized by the diffraction of the output beam into a central beam and many side lobes occurs. For  $Q = 10$ , Bragg deflection takes place, and the output beam is deflected into one side lobe only. For the intermediate range of  $Q$ , the output diffraction pattern becomes complex.

The degree of amplitude modulation depends on the net phase change,  $\Delta\theta$ , the beam experiences in traversing the region of perturbed index. For Raman-Nath diffraction, the central beam intensity varies as  $J_0^2(\Delta\theta)$ , where  $J_0$  is the Bessel function of zero order; this function has its first zero when  $\Delta\theta = 2.4$ . For Bragg deflection, the central beam intensity goes as  $\cos^2(\Delta\theta/2)$ , which has a zero for  $\Delta\theta = 3.14$ .

The change in index of refraction  $\Delta n$  for a quadratic electro-optic material is given by the relation

$$\Delta n = -\frac{1}{2} g n^3 \epsilon^2 E^2 \quad (4.2)$$

where  $g$  is the electro-optic coefficient,  $\epsilon$  is the dielectric constant and  $E$  is the applied electric field. The phase change can then be expressed as:

$$\Delta\theta = \frac{2\pi}{\lambda_0} W \Delta n \quad (4.3a)$$

$$= \frac{\pi}{\lambda_0} g n^3 \epsilon^2 E^2 W \quad (4.3b)$$



Equations 4.1 - 4.3 are the basic design equations determining device operation. In general, one desires to minimize drive voltage,  $V$  (proportional in our case to the product of  $E$  and  $L$ ). The design options include: changing electrode geometry, increasing  $W$ , decreasing  $L$ , or finding materials with larger values of  $g$ ,  $\epsilon$  or  $n$ .

#### 4.2 Modulator Evaluation

For our KTN modulator a film with composition  $\text{KTa}_{0.74}\text{Nb}_{0.26}$  was used. Film thickness was about 3 microns, allowing for propagation of 2 TE and 2 TM modes. All evaluation and analysis was done using the  $\text{TE}_0$  mode at 633 nm (Fig. 4.1). For our electrode geometry,  $Q = 2.09$  ( $N_m \approx 2.25$ ), and consequently we were operating in the Raman-Nath regime. The predicted<sup>4</sup> amplitude modulation for the central beam is 90% for  $\Delta\theta = 2.3$ , a value obtained in our system when  $\Delta n = 7.7 \times 10^{-5}$ . We find from experiment (Fig. 4.2) that maximum intensity modulation of the central beam is achieved with about 15 volts applied across the electrode. This value corresponds to a surface field of 6000 V/cm. As a check we can compute the predicted index change in a 36 mole % Nb film for this field strength. From the data of Chen et al.,<sup>5</sup> we have  $\epsilon = 1930 \epsilon_0$ ,  $g = 0.136 \text{ m}^4/\text{c}^2$ . Using Eq. (4.2) we then obtain  $\Delta n = 7.9 \times 10^{-5}$ , in close agreement with the theoretical value of  $7.7 \times 10^{-5}$ .

Waveforms of the modulated central beam are shown in Figs. 4.3 and 4.4. Biased operation is shown in Fig. 4.3, modulation without bias in Fig. 4.4. The latter yields a second harmonic output because the KTN film is in the paraelectric phase, where it is characterized by a quadratic electro-optic effect. There is, however, some first harmonic signal, suggesting the presence of a linear electro-optic effect (which may be strain induced).

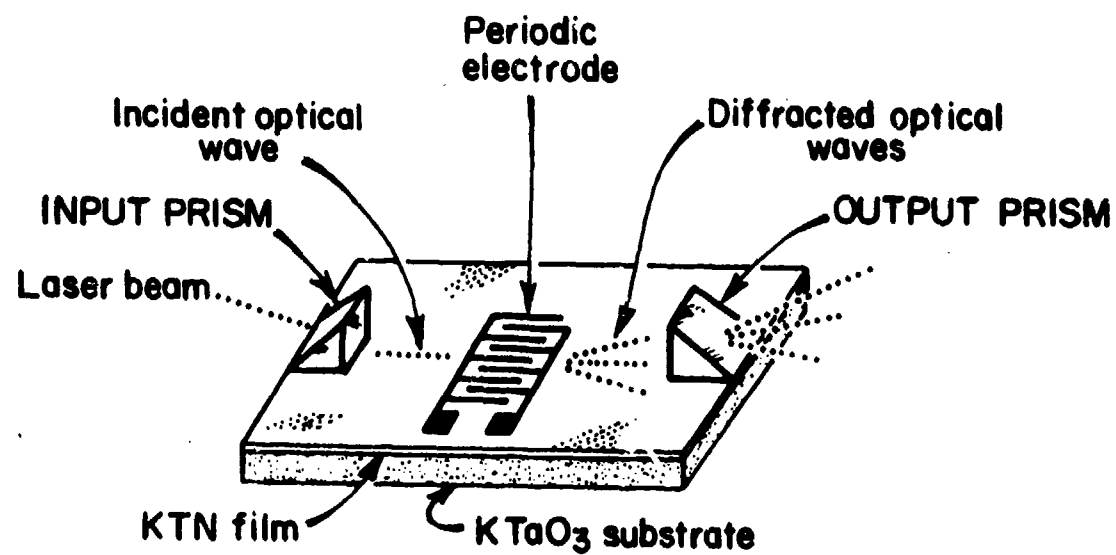


Fig. 4.1 Experimental arrangement for evaluation of modulator.

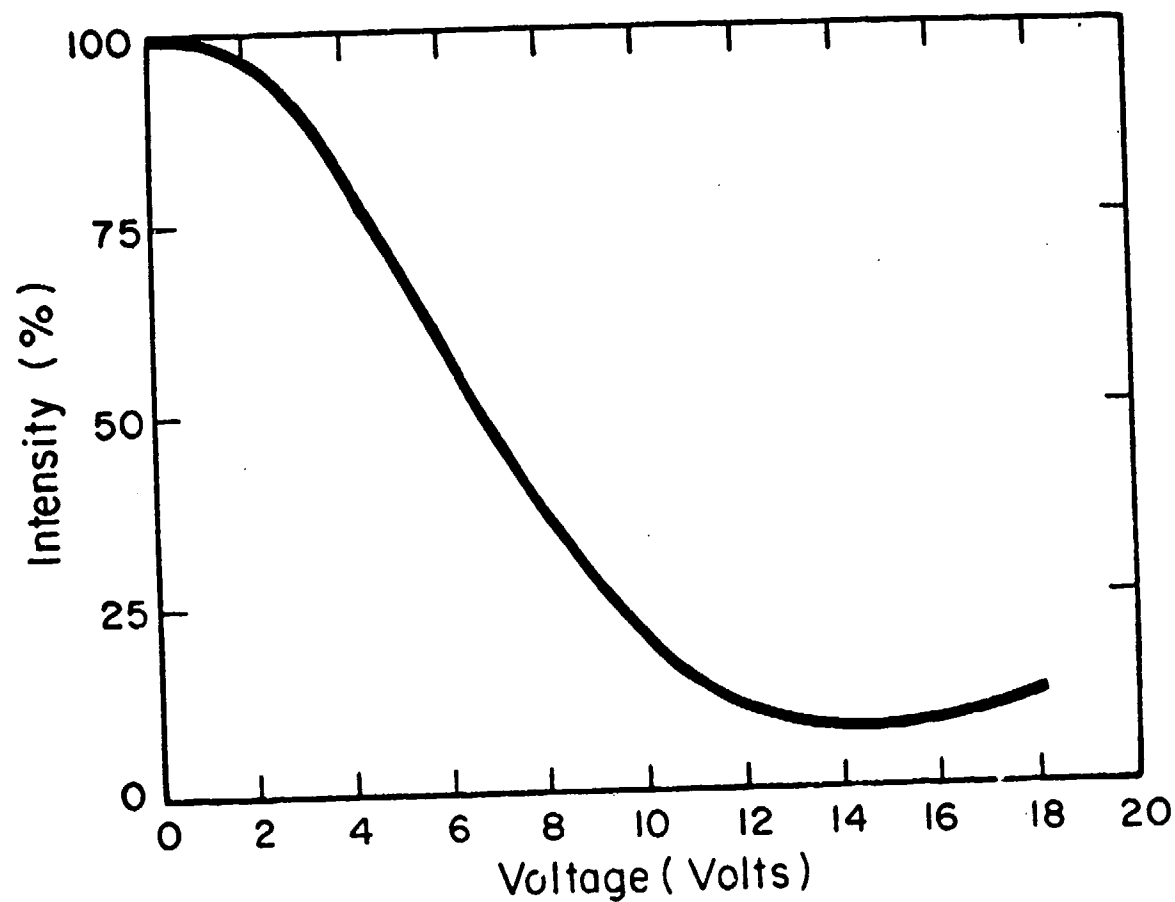
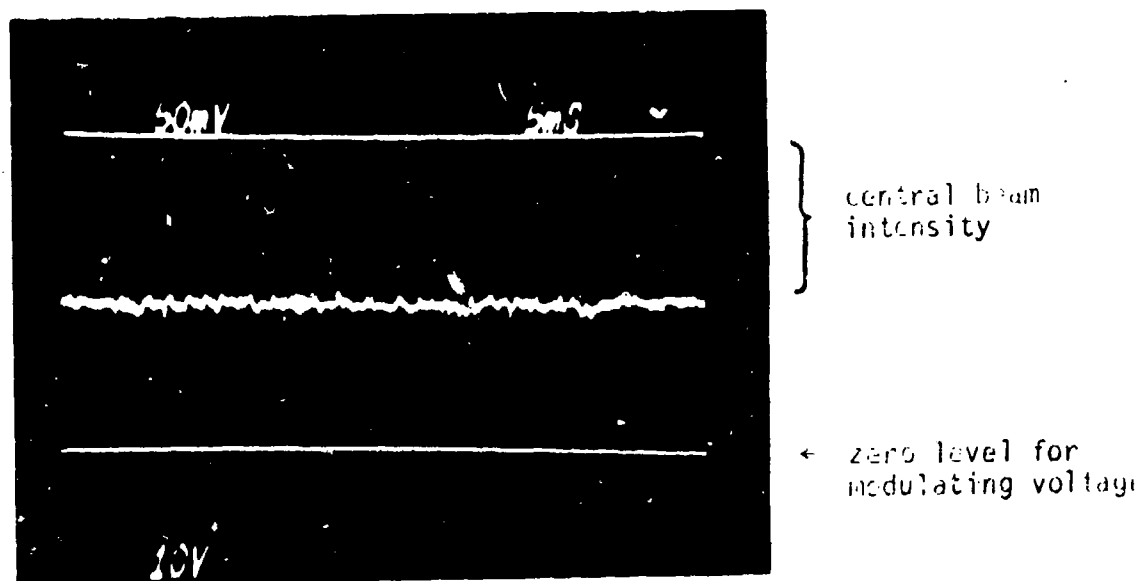


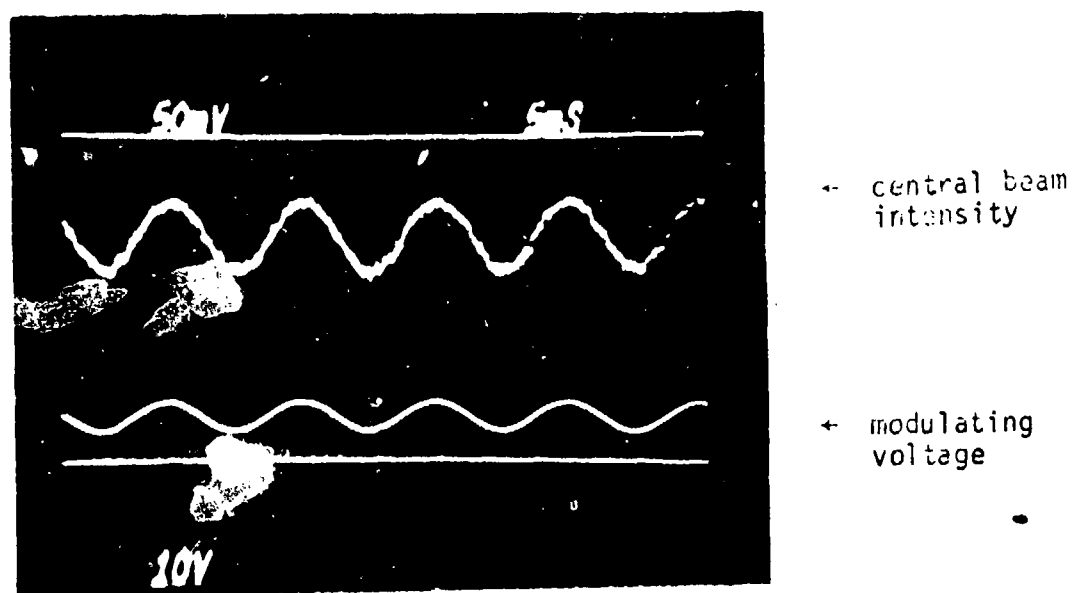
Fig. 4.2 Output of central beam as a function of voltage applied to modulator.

Reproduced from  
best available copy.



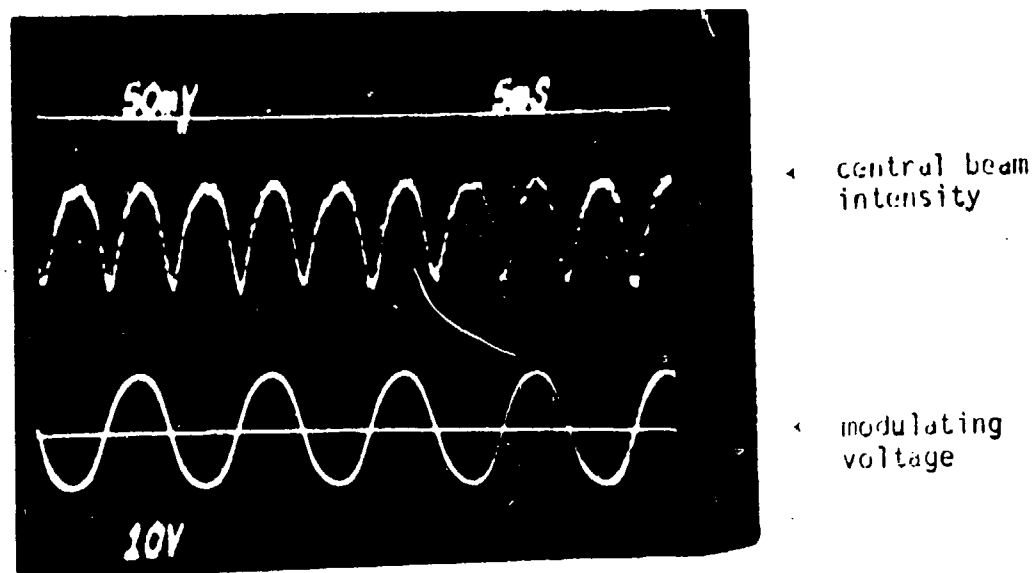
Intensity of central beam with no modulating voltage applied to electrodes.

Fig. 4.3a



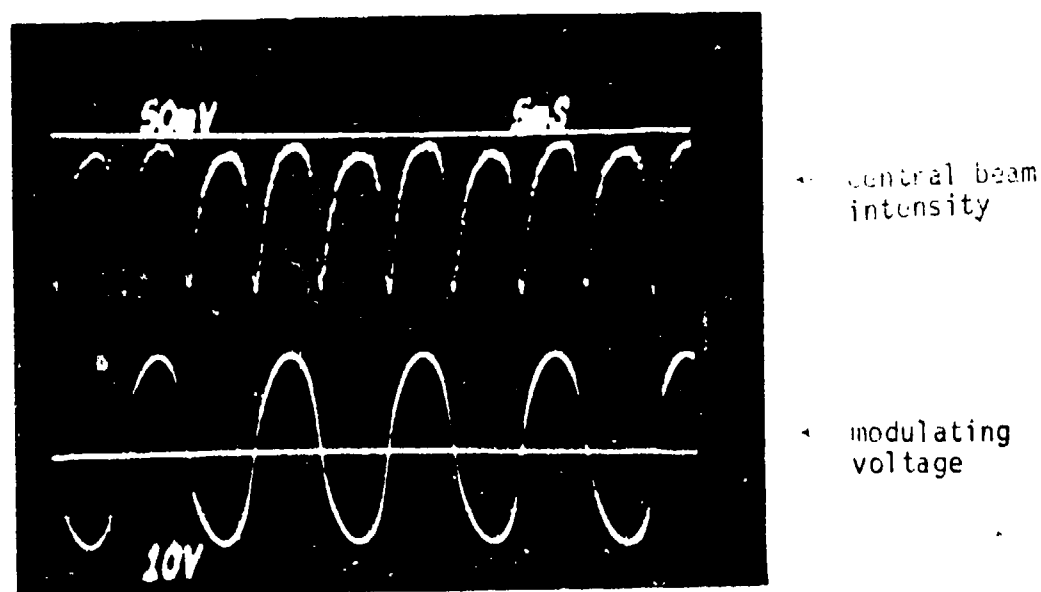
Intensity of central beam for a 5-volt peak to peak modulating voltage superimposed on a 7-volt dc bias.

Fig. 4.3b



Intensity of central beam for a 16-volt peak to peak modulating voltage. Approximately 65% modulation is achieved.

Fig. 4.4a



Intensity of central beam for a 32-volt peak to peak modulating voltage. Approximately 90% modulation is achieved.

Fig. 4.4b

Modulation of the central beam was further demonstrated by monitoring the diffracted light output as a function of distance from the central beam (Fig. 4.5). Note the presence of a first and second order side lobe. These data were taken using a photomultiplier tube behind a 100  $\mu\text{m}$  pinhole aperture.

Film loss in the  $\text{TE}_0$  was determined using a fiber optic probe to monitor the scattered light of the mode streak as a function of distance. From the results shown in Fig. 4.6, a loss of 28 db/cm was calculated.

The present modulator has a rather restricted bandwidth and at the moment we are trying to understand why this is so. The response to a step function input shows a rise time of at least 3  $\mu\text{s}$ . The response is probably faster, but we are limited in our present measurements by the time constant of our photodetector circuit. Because of the high loss in the film, the photodetector load resistor must be kept relatively high to maintain sensitivity and we are forced, in the existing arrangement, to accept the consequent time constant. If we take 3  $\mu\text{s}$  as the upper bound for response time, we conclude that the frequency response for sinusoidal excitation should have a lower bound of about  $5 \times 10^4$  Hz. Although we feel that this value is an unduly low estimate, it appears not much out of line with the results shown in Fig. 4.7. These data, obtained with periodic pulse excitation, show an additional complication. The response is duty cycle dependent, being lower at higher duty cycle. This feature suggests we may be encountering a heating problem in the film.

The I-V characteristic of the modulator shows non-ohmic behavior at field strengths above 4000 V/cm. This phenomenon is characteristic of blocking contacts observed in bulk KTN.<sup>6</sup> Low field measurements give a dc resistance of 1.4 M $\Omega$ , corresponding to a conductivity of  $\sim 10^{-6}$

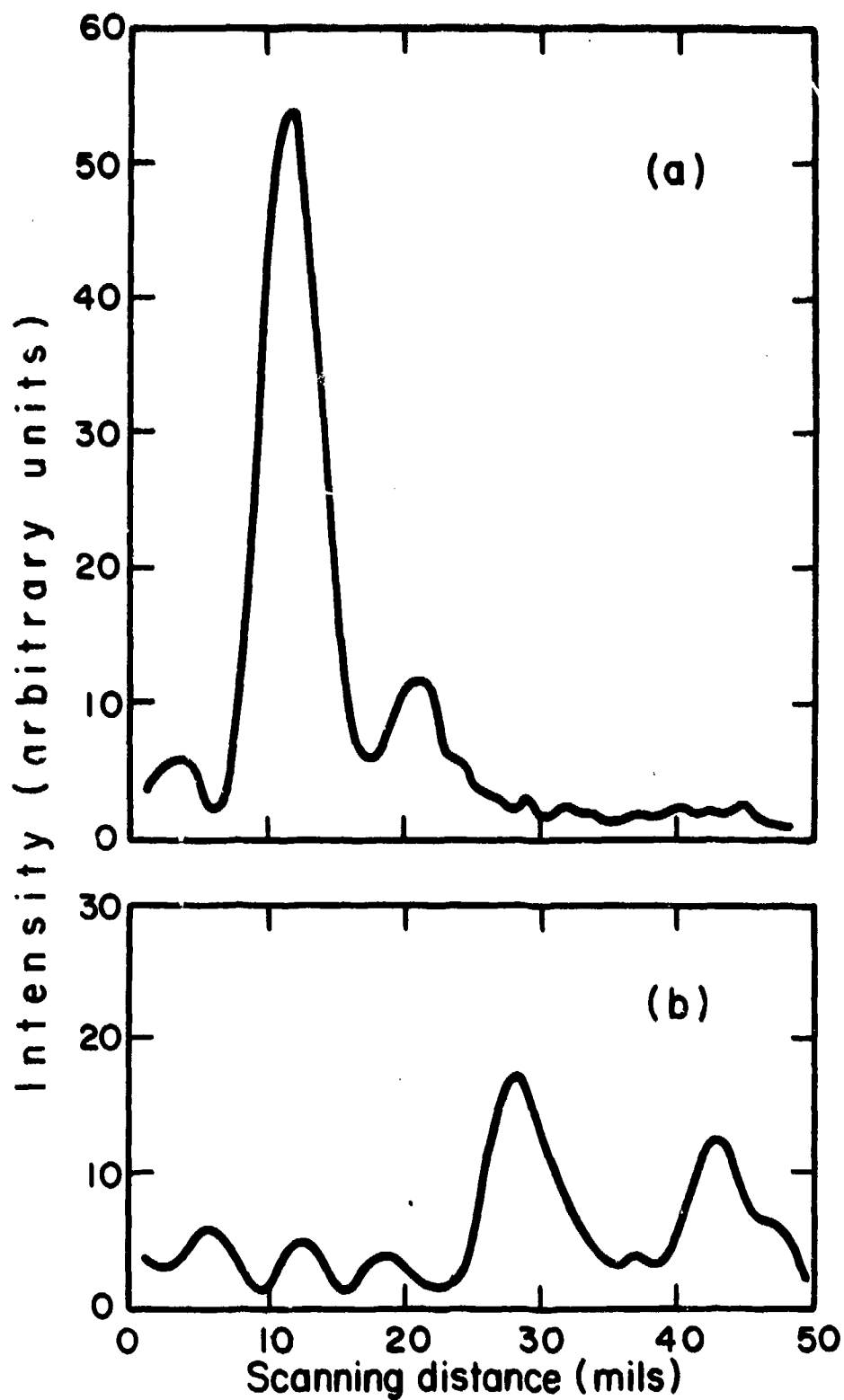


Fig. 4.5 Profile of output light beam: (a) zero modulator voltage; (b) modulator voltage adjusted for maximum reduction of central beam.

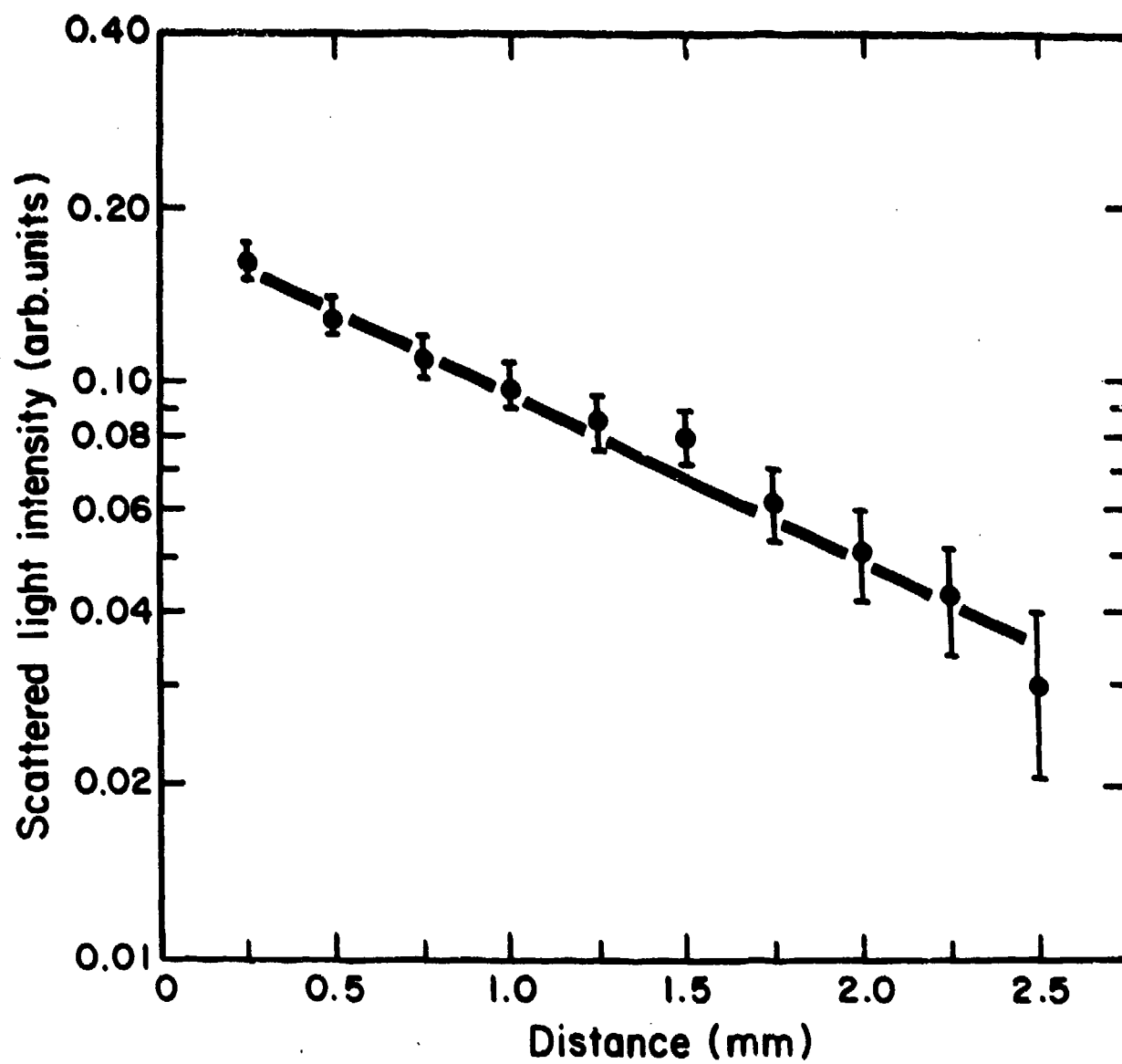


Fig. 4.6 Scattered light intensity measured along track of guided mode.



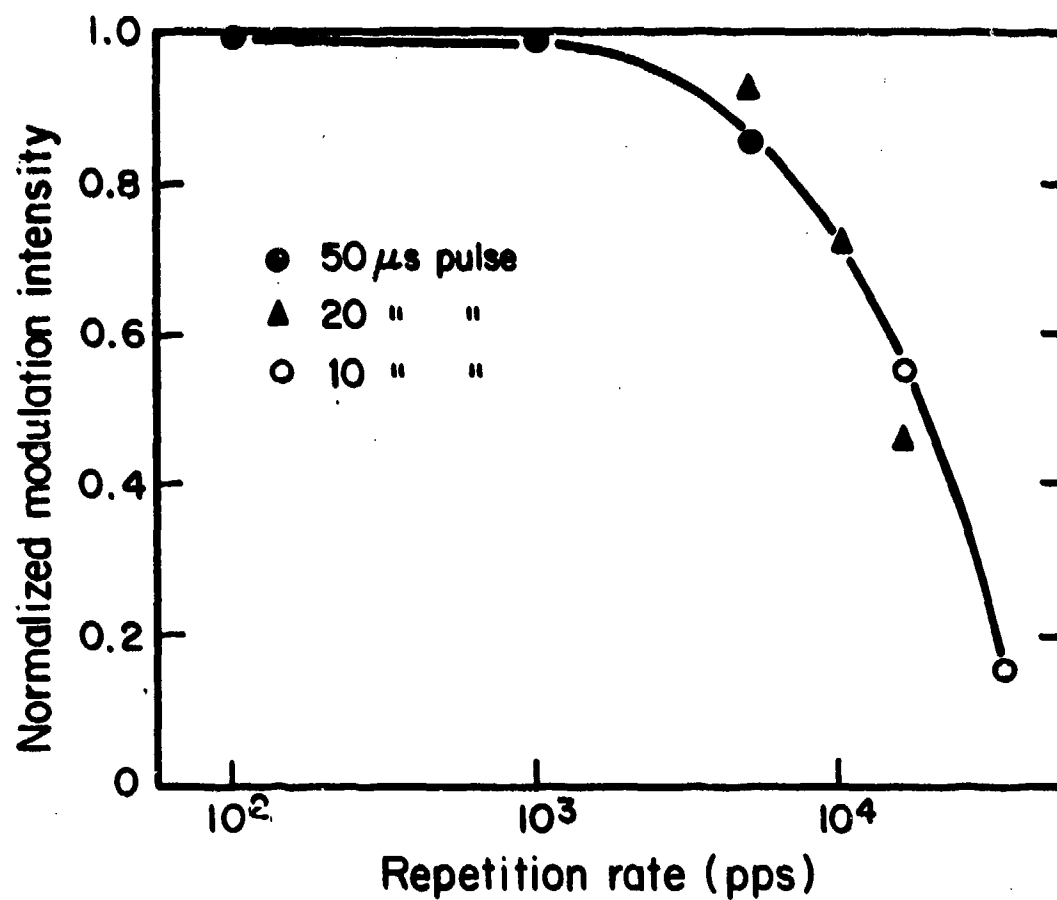


Fig. 4.7 Modulator response to periodic pulse train.

$(\text{ohm-cm})^{-1}$ . The relatively large conductivity suggests that the film is partially reduced.

#### 4.3 Improvement of Performance

The discussion in the previous section reveals a number of materials problems that require detailed investigation. To begin with, optical loss in the films we have grown thus far is excessively high. At present we can only speculate on its origin. One possibility is that the loss results from an excessively rapid and multinucleated crystal growth which produces a highly dislocated film. This growth condition may also be responsible for the "hillocky" surface texture shown by these films. To obtain films which can guide light we have removed the hillocks by polishing, and thereby have reduced light scattering due to surface variations, but if the hillocks are merely manifestations of volume variations we must still contend with a large bulk scattering. We hope to obtain improved film quality by growing more slowly from a melt somewhat diluted in nutrient. An attempt will be made to correlate growth conditions with optical attenuation.

Another source of optical loss could be lattice mismatch between film and substrate. It has been noted<sup>7</sup> that lattice mismatch can lead to periodic strain in the film. This sort of strain would give rise to index fluctuations capable of scattering light. We have recently acquired a tuneable cw dye laser that will enable us to measure optical attenuation as a function of wavelength. The information on size of scattering volume, provided by such measurements, will be valuable in distinguishing among the variety of possible causes for optical attenuation. If, for example, lattice mismatch is indeed the basic cause, not only should the loss diminish with reduction in mismatch but there should also be an

increase in the volume of the effective scattering "element". We note in passing that biaxial stress produced by lattice mismatch could also account for the slight first harmonic frequency component seen in the modulator output (Fig. 4.4).

The dc conductivity observed in our present films, estimated to be of the order of  $10^{-6} \text{ ohm}^{-1} \text{ cm}^{-1}$ , is less troublesome as a source of dissipation than as a source of contact problems. The addition of Sn as a dopant should increase the resistivity by compensating for the n-type donors we believe have been created in our films by conditions of crystal growth that are slightly reducing. An increase in resistivity and the use of contact materials with low oxygen affinity<sup>8</sup> should eliminate the blocking contacts. The presence of such contacts might conceivably be desirable in designing optical switches with sharp threshold characteristics, but at the present state of our work their existence only creates unnecessary complications in interpreting device performance and carrying out film evaluation.

The observed degradation of modulator response with increasing duty cycle is very much suggestive of a heating problem and could be indicative of excessive dielectric losses. Once our contact problems are eliminated we shall begin a detailed study of the dielectric properties of our films as a function of both frequency and field strength.

We are starting now to grow films with Nb concentrations in the range 35-38 mole %, an amount larger than previously used. These new compositions, with larger electro-optic coefficients, will enable us to reduce modulator operating voltage. A further reduction will be obtained by using an electrode configuration with closer spaced fingers. Our expectation is a modulator with peak drive in the 1-5 volt range. We

have already grown for preliminary tests a 35 mole % Nb film on a  $\text{KTaO}_3$  substrate and are preparing an 18 mm diameter substrate for a new modulator.

#### 4.4 Growth of KTN by Chemical Vapor Deposition

Previous attempts to grow KTN by CVD were not successful because the reactants could not be brought together under the proper conditions in a single zone furnace, principally because no flat temperature zone existed that would accommodate the Knudsen cell used as a KCl source. A two-zone furnace has been modified and adapted to grow KTN. The modifications included redesign and rebuilding of the external reactors to handle the Ta and Nb. Necessary improvements in the gas distribution system and pumping system and replacement of parts have been carried out. The work underway at present is concerned with modifying the existing temperature profile so that it will be nearly flat (at  $\sim 950^\circ\text{C}$ ) over the 5" length of the Knudsen cell. This objective will be achieved by adding a second Kanthal wire-wound furnace around an extended reactor tube just outside the main furnace. The main furnace consists of eight globars which run the length of a 48 mm diameter gas-tight mullite reaction tube with four globars perpendicular to these in one half of the furnace. Each set of globars is separately controlled by an API Instruments Company controller. In the unmodified two-zone system, the temperature profile across the Knudsen cell was found to be much too steep. The value of  $950^\circ\text{C}$  was arrived at experimentally by determining the temperature at which the vapor pressure of KCl in the cell became sufficiently high to provide a gas flow large enough to react with  $\text{TaCl}_5$  and  $\text{NbCl}_5$ .

## V. COUPLING FROM LASER TO WAVEGUIDE

For the thin film waveguide structure shown in Fig. 5.1 it is well known that the normal modes of propagation fall into three distinct categories: (1) guided modes, which propagate in the dielectric film of index  $n_1$  but are evanescent in the superstrate  $n_0$  and substrate  $n_2$ ; (2) substrate modes which exhibit evanescent behavior only in the superstrate; and (3) superstrate modes which show no evanescence in any region of space. (When  $n_0 = 1$  these are the so-called air modes.) The allowed values of  $k_z$  for each category of modes is shown in Fig. 5.2, where the mode angle  $\theta$  for a representative guided mode is also shown.

In order to launch a guided mode it is necessary to match the z-directed phase variation of the excitation to the phase constant  $k_z$  of the guided wave. In the prism coupler the required phase synchronism is established by physically adjusting the angle of the incident light beam relative to the prism base. In the grating coupler the spatial periodicity of the grating provides an additional k-vector which is used to make up the difference in phase between the exciting wave and the guided mode.

In this program our interest is in coupling from a laser mode in a dielectric cavity to a thin film waveguide. The required phase matching can in some circumstances be obtained by suitably adjusting the propagation angle of the laser mode. This approach requires that the cavity be cladded with suitable dielectric coatings in order to restrict the allowed cavity modes to the desired angles. The design principles which underlie this scheme are described below in section 5.1. Because this approach has a number of limitations, we encounter situations where

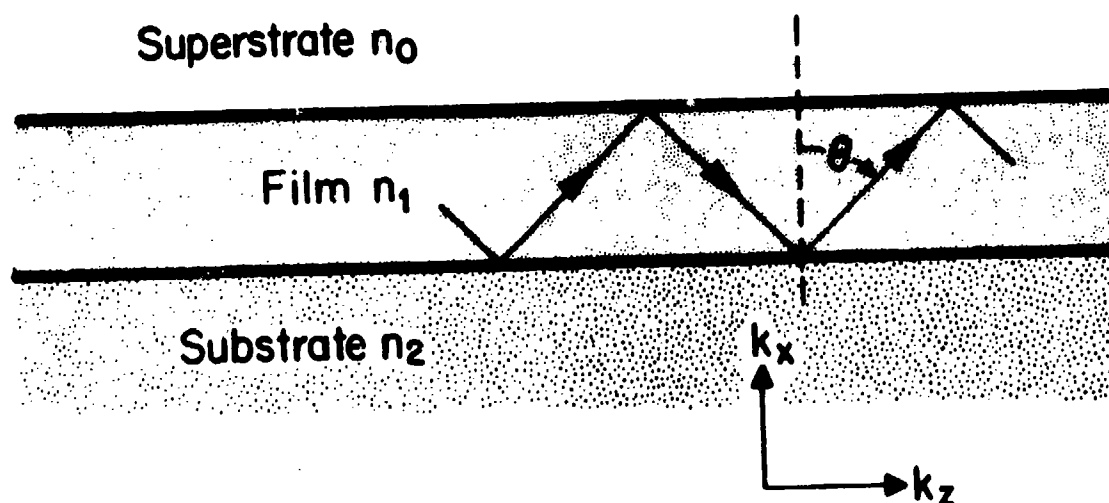


Fig. 5.1 Thin film waveguide structure.

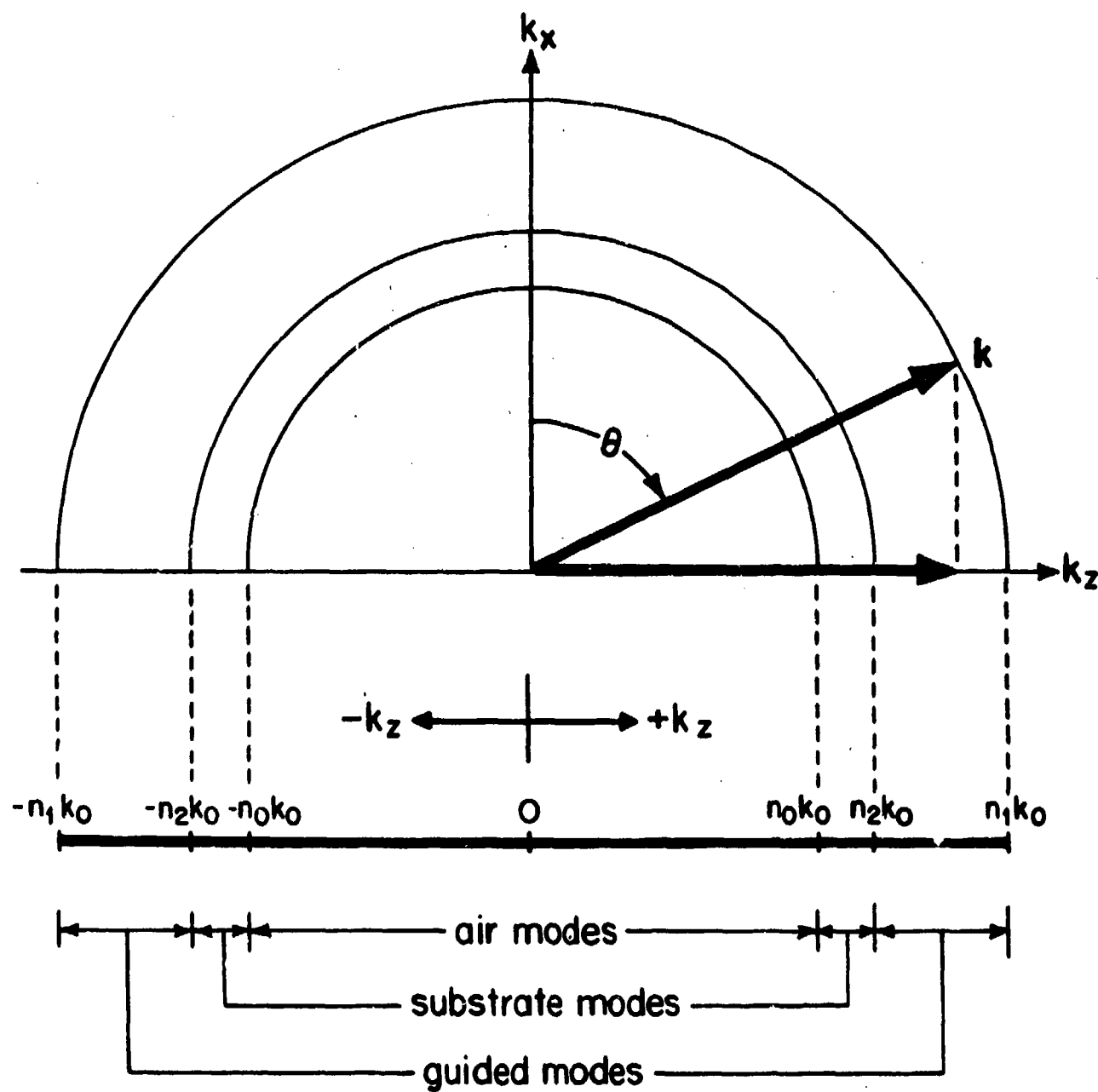


Fig. 5.2 Modes in thin film waveguide.

grating couplers must be used. The usual grating coupler is designed to couple an air mode to a waveguide mode, but, as we note in section 5.2, our problem is slightly different in that the source of excitation is the evanescent field associated with the laser cavity mode.

### 5.1 Mode Control by Dielectric Cladding

For the dielectric cavity laser there is a simple geometric way of determining the allowed cavity modes. We draw in  $k$ -space two circular arcs, as shown in Fig. 5.3, one of radius  $n_L k_0$ , the other of radius  $n_0 k_0$  ( $n_L$  is the refractive index of the laser material,  $n_0$  the index of the surrounding medium and  $k_0 = 2\pi/\lambda_0$ , where  $\lambda_0$  is the free space wavelength). We now draw the horizontal and vertical tangents to the smaller arc, as shown, and find their intersections (A and B) with the arc  $n_L k_0$ . For laser oscillation at  $\lambda_0$  the allowed  $\bar{k}$ -vectors lie on the latter arc between the points A and B, and have mode angles bounded by  $\theta_A$  and  $\theta_B$ . Accordingly, the  $z$ -component of  $\bar{k}$  is confined to the range  $k \sin \theta_A < k \sin \theta_B$ .

In order to get single mode laser operation it is important to limit the allowed number of cavity modes. This objective can be met by adjusting the refractive index of the cavity relative to the external index. It is easily seen from Fig. 5.3 that as  $n_L \rightarrow \sqrt{2}n_0$  the number of modes becomes vanishingly small since  $\theta_A \rightarrow \theta_B \rightarrow 45^\circ$ , with the attendant result that  $k_z \rightarrow n_0 k_0$ . This situation, desirable from the point of view of obtaining single mode laser oscillation, imposes serious restrictions on other design considerations. It would, for example, be very convenient to have the laser crystal mounted in air; but if we set  $n_0 = 1$  we require that the index of the laser host be  $n_L \approx \sqrt{2}$ , thus imposing a serious constraint on laser design. Fortunately, the refractive index of  $\text{LiYF}_4$  (see Table 7.1) meets the index criterion and, consequently, we have



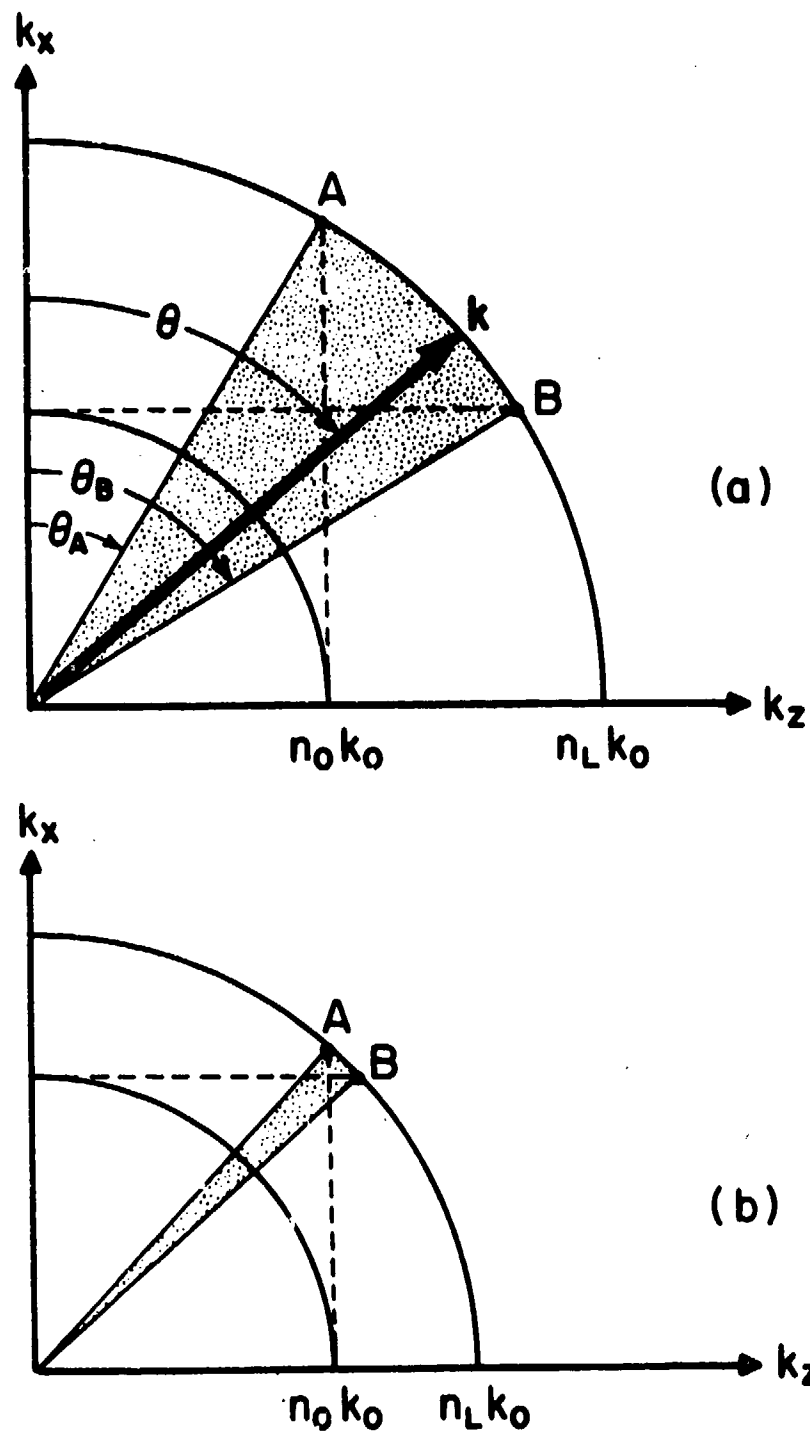


Fig. 5.3 Allowed modes for dielectric cavity. The allowed  $\vec{k}$ -vectors occur with the shaded sectors. The large number of modes occurring in (a) is reduced in (b) by decreasing the ratio  $n_L/n_0$ .

been able to obtain single mode lasing using a simple rectangular cavity surrounded by air.

We must now consider the constraints on output coupling. We have already noted that as  $\theta \rightarrow 45^\circ$  the wave-vector component  $k_z$  for the laser mode approaches  $n_0 k_0$ . Reference to Fig. 5.2 shows that if we are to couple to a thin film waveguide mode we must have  $n_2 \rightarrow n_0$ , so that if  $n_0 = 1$  we can only couple to a thin film on an air substrate! Thus, for the configuration under consideration, the attempt to achieve a direct phase match between a laser mode and a guide mode is frustrated by very practical considerations. However, coupling can be achieved by introducing a grating structure between laser and guide. The issues involved in this problem are discussed in section 5.2 which follows.

However, we need not completely surrender the attempt to use direct coupling schemes, for there is a cavity design procedure that allows us to overcome the restriction that the laser mode angle lie near  $45^\circ$ . The design approach involves the partial cladding of the cavity surfaces by dielectric coatings of controlled refractive index.

In Fig. 5.4a we show a dielectric cavity cladded on its top surface with a thick film (index  $n_c$ ). The allowed mode angles can be obtained from the geometric construction shown in Fig. 5.4b. As  $n_c$  is increased, the point A moves toward B and the number of allowed modes decreases progressively, vanishing in the limit as the two points coalesce. In this limit the mode angle is given by  $\theta = \tan^{-1} (n_c/n_0)$  with  $n_c = \sqrt{n_L^2 - n_0^2}$ . Note that, by top cladding, the mode angle has been increased from the  $45^\circ$  angle value it had for the unclad case, and  $k_z$  is increased from  $n_0 k_0$  to  $n_c k_0 = \sqrt{n_L^2 - n_0^2} k_0$ . Thus, the laser mode can be phase matched to a guide deposited on a substrate having an index with upper bound  $\sqrt{n_L^2 - n_0^2}$ . If

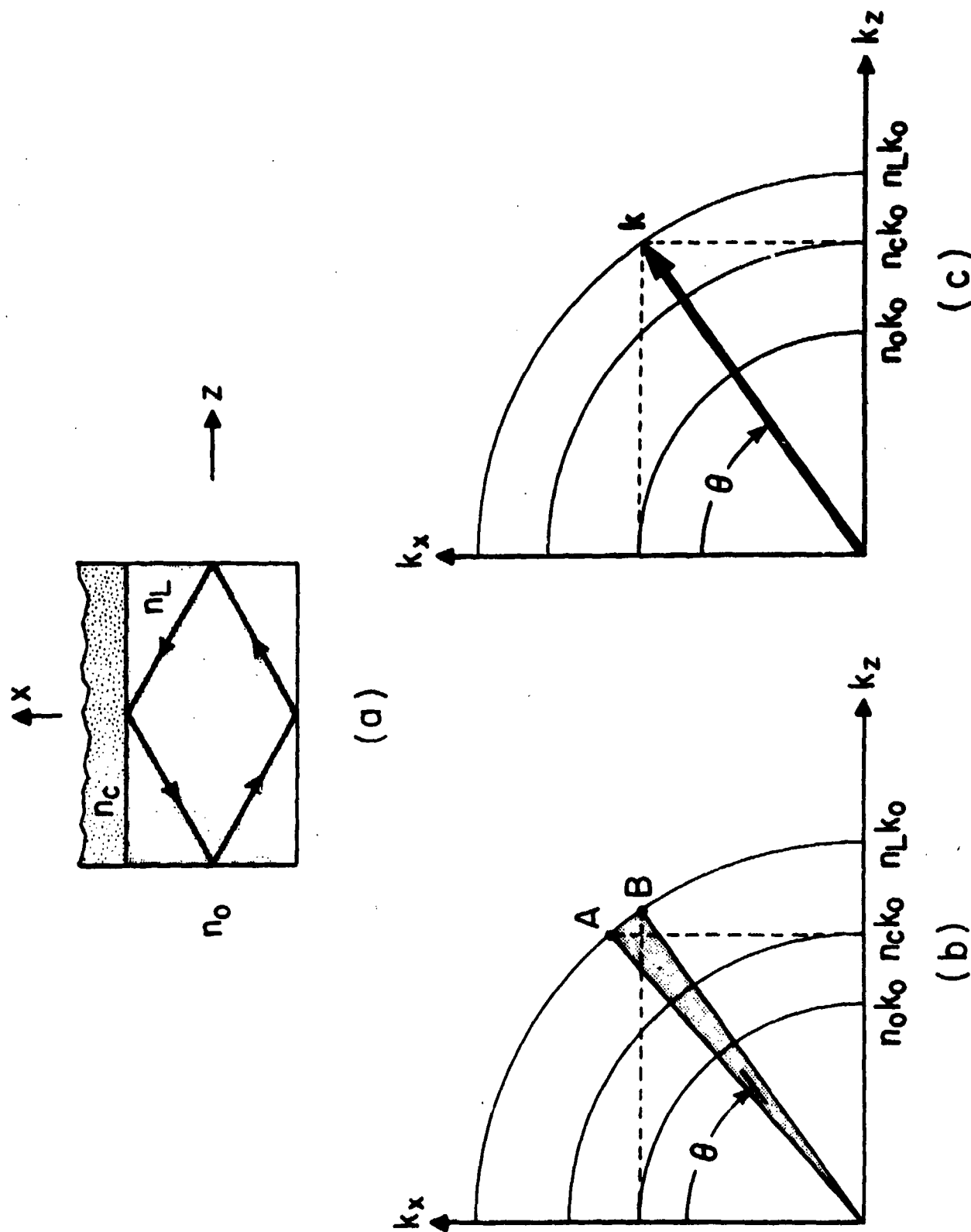


Fig. 5.4 Top cladding: (a) the dielectric cavity; (b)  $n_c$  adjusted to produce a narrow range of mode angles; (c) the "single mode" condition.

we now also apply side cladding (Fig. 5.5) we can phase match to guides on substrates between this upper bound and a lower bound  $n_o$ . We need only pick the desired  $n'_c$  in the range  $n_o < n'_c < \sqrt{n_L^2 - n_o^2}$  and then determine the required  $n''_c$  from the relation  $n''_c = \sqrt{n_L^2 - n'^2_c}$ . It is evident that the larger the index  $n_L$  of the laser host material the greater the phase match range.

While cladding introduces a significant design flexibility there will always remain situations where direct phase matching is not possible and where it is consequently necessary to employ some other coupling scheme, e.g., a grating.

## 5.2 General Considerations for the Grating Coupler

The conventional grating coupler is used in a situation where one desires to transfer energy between a beam in free space and a waveguide mode. The design goal for this problem is to choose a periodicity, depth and length of grating which maximizes the energy transfer. In our situation we still desire to couple to a guide but the excitation rather than being a beam is the evanescent field associated with a laser mode in a dielectric cavity. There are some circumstances in which this coupling can be effected without exciting a substrate mode and in such a case the design requirements for coupling strength and length are not particularly critical. If, however, excitation of a substrate mode is unavoidable, the design, if it is to be efficient must maximize the ratio of guide to substrate power. In either of these cases it is important first to choose a proper periodicity for the grating. If too large a periodicity is chosen the grating will excite unwanted diffracted beams which needlessly carry away energy. As shown in Fig. 5.6, the desired choice is one that couples a laser mode into a waveguide mode propagating in the opposite direction. The only unwanted

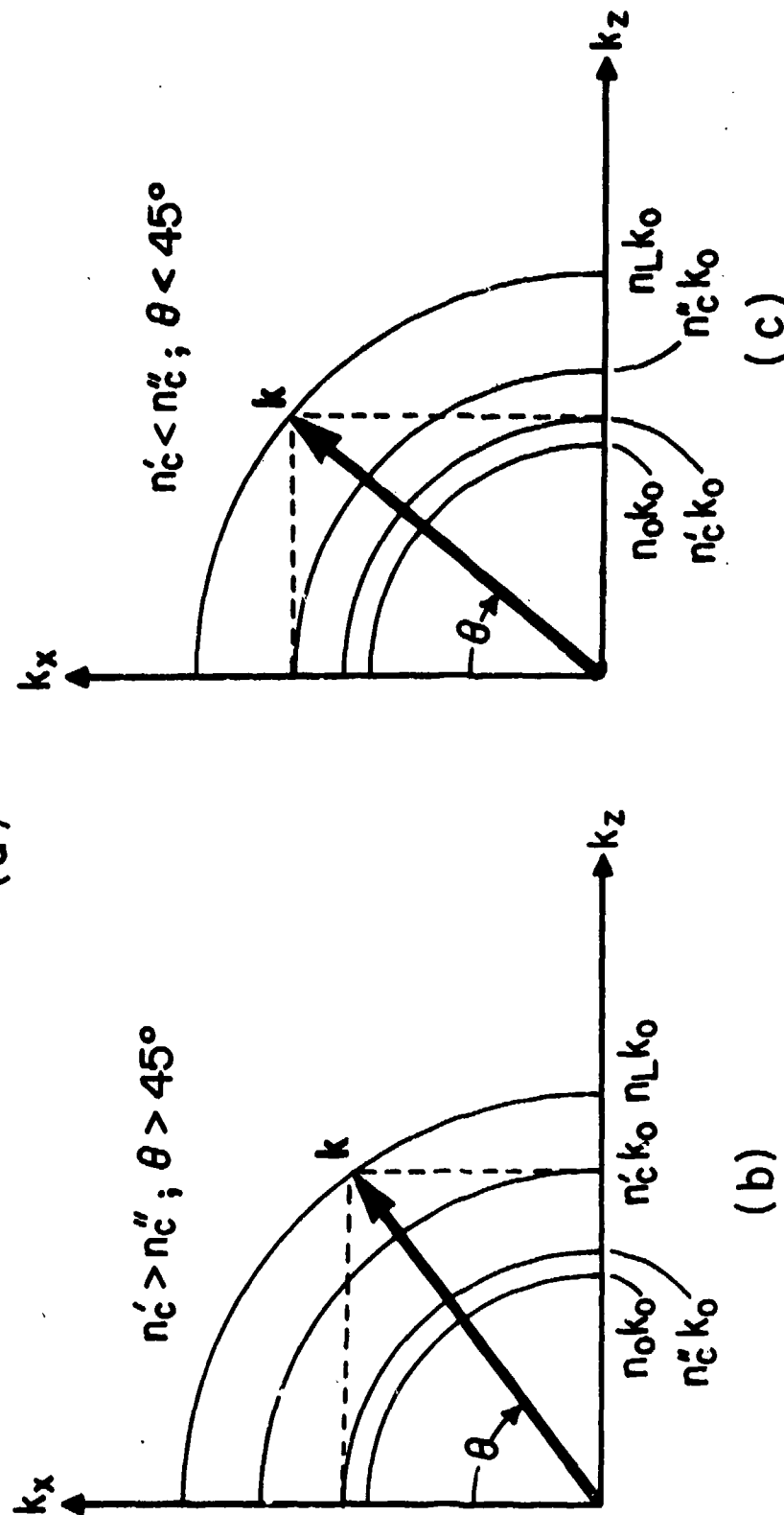
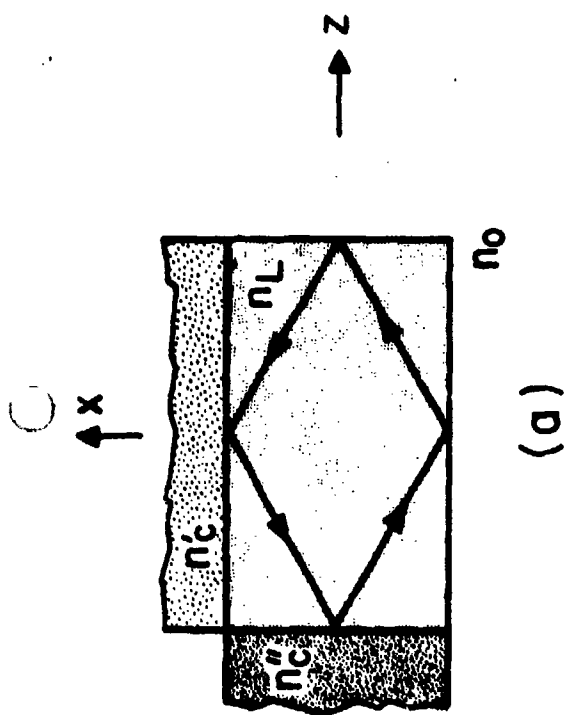


Fig. 5.5 Top and side cladding: (a) the dielectric cavity; (b) "single mode" condition with  $\theta > 45^\circ$ ; (c) "single mode" condition with  $\theta < 45^\circ$ .

mode that will then exist is a substrate mode which could, of course, be eliminated if  $n_L$  were greater than  $n_2$ . In this case, however, we could dispense with the grating and use the prescription of Section 5.1 to couple to the guide without using a grating. In the analysis given below we assume that a substrate mode cannot be avoided.

### 5.2.1 Power in the Waveguide Mode

If the magnitude of the electric field of the incident wave in the laser crystal is  $A_L$ , the field at the grating surface will be approximately

$$A_o = A_L e^{-\sigma g} \quad (5.1)$$

where

$$\sigma = k \sqrt{n_L^2 \sin^2 \theta - 1} \quad (5.2)$$

The power in the waveguide mode builds up as<sup>9</sup>

$$P_g(z) = \frac{A_o^2 n_L k \cos \theta \alpha_{ma}}{\omega \mu_o} \frac{(1 - e^{-\alpha_{ms} z})^2}{\alpha_m^2} \quad (5.3)$$

where

$$\alpha_m = \alpha_{ma} + \alpha_{ms} \quad (5.4)$$

and  $\alpha_{ma}$  and  $\alpha_{ms}$  are the coupling coefficients between the waveguide wave and the air and substrate, respectively. Expressions for  $\alpha_{ma}$  and  $\alpha_{ms}$  can be found in the literature.<sup>9,10</sup> Harris et al.<sup>10</sup> for example, give expressions that can be simplified (when  $n_1 \approx n_2$ ) to

$$\alpha_{ma} = \frac{\delta^2 h_o^2 (n_1^2 - 1)k}{16 t n_L |\cos \theta| \pi^2 \beta m^2} \quad (5.5)$$

$$\alpha_{ms} = \frac{\delta^2 h_o^2 (n_1^2 - 1)k}{8t \pi^2 \beta_m^2 \sqrt{n_2^2 - n_L^2} \sin^2 \theta} \quad (5.6)$$

where  $h_o^2 = n_1^2 k^2 - \beta_m^2$ , and  $\beta_m$  is the wavevector of the waveguide mode.

### 5.2.2 Transmitted Power

The important design goal is to minimize the ratio of the transmitted (substrate mode) power to the waveguide mode power. As already noted, this design goal is quite different from that of the conventional grating couplers.<sup>9</sup> There one tries to maximize the ratio of the waveguide power to the incident power and finds an optimum coupling length  $L$  given by  $\alpha_{ms} L = 1.25$ .

The field, and hence power, in the transmitted beam is determined by the phasor sum of two main field components. One is the transmitted wave field in the absence of the grating,  $A_o T$ , where  $T$  is a complex transmission coefficient. This component is represented by the solid arrow in Fig. 5.6. The other component (dashed arrow) is the field scattered into the same direction from the waveguide mode by the grating. Since this scattering is responsible for the loss coefficient  $\alpha_{ms}$ , the magnitude of the scattered field can be related to the waveguide mode field and is found to be

$$A_t(z) = A_o a (1 - e^{-\alpha_{ms} z}) \quad (5.7)$$

$$a \equiv \sqrt{2\alpha_{ma}/\alpha_{ms}} \quad (5.8)$$

The phase of this field component, however, can only be found from some more detailed analysis. We are currently trying to solve this

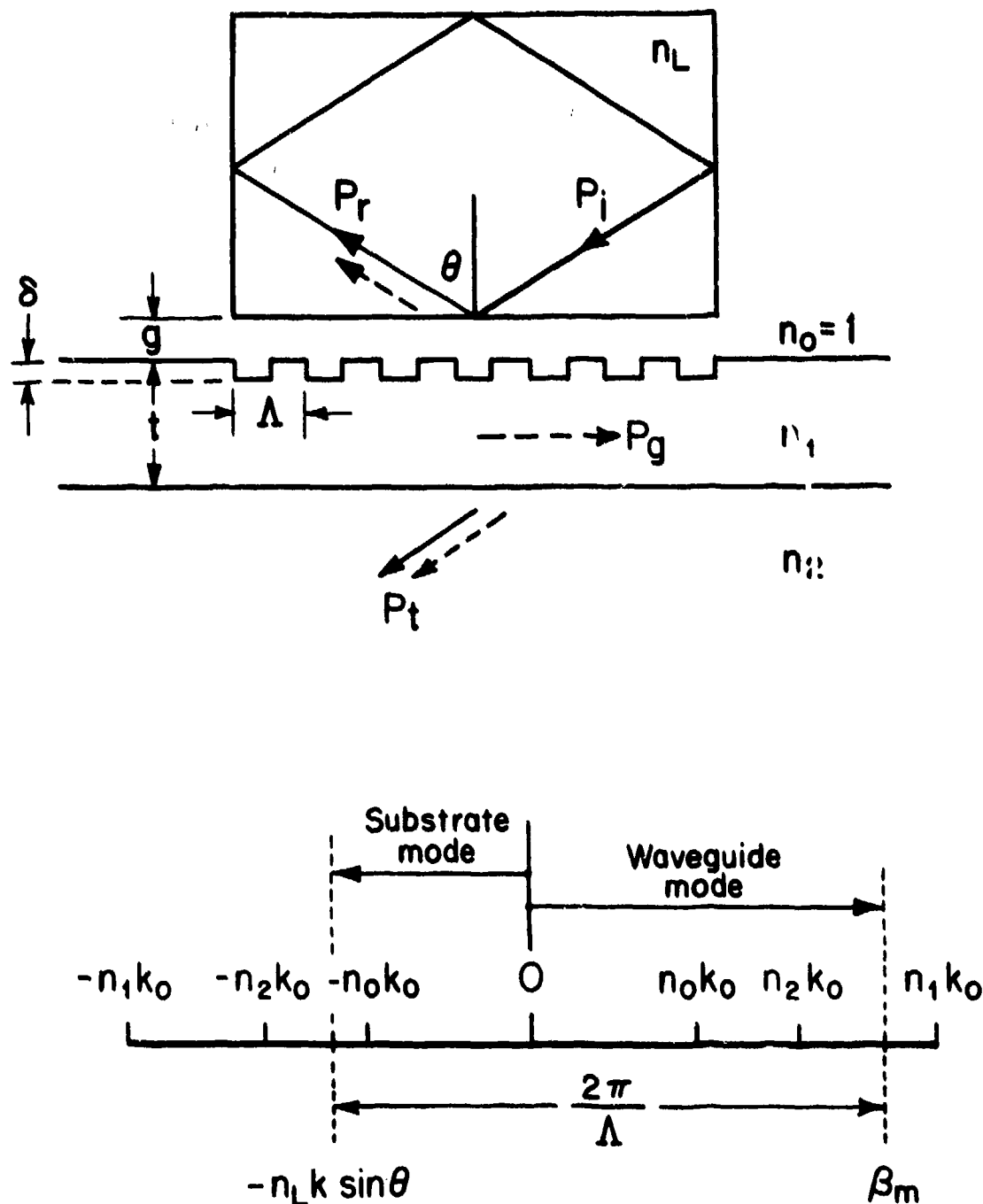


Fig. 5.6 Laser cavity coupled to guide by a grating. As shown in the lower part of the figure, the laser mode traveling to the left is coupled to a waveguide mode traveling to the right; the laser mode also excites a substrate mode traveling to the left.



problem.

### 5.3 Tolerance in Grating Periodicity

As in any other coherent interaction the phase mismatch tolerance is  $\Delta k < \pi/L$ , or

$$\frac{2\pi}{\Lambda} - n_L k \sin \theta - \beta_m < \pi/L \quad (5.9)$$

Using typical numbers ( $\Lambda = 0.5 \mu$ ,  $L = 250 \mu$ ), we see that  $\Lambda$  has to be fabricated to within a tolerance of one part in a thousand, provided that  $n_L k \sin \theta$  and  $\beta_m$  are known exactly. An even more difficult problem is that we are not likely to know  $\beta_m + n_L k \sin \theta$  to better than one part in a hundred. Therefore, one or both of  $\Lambda$  and  $\beta_m$  must be designed to have a continuous range of one part in a hundred. This can be done by making  $\Lambda$  or  $\beta_m$  functions of  $z$ , i.e.,  $\Lambda = \Lambda(z)$  (chirped grating) or  $\beta_m = \beta_m(z)$  (tapered waveguide). Or we can make  $L$  very small. In all these schemes the effective length of the coupling region become smaller than the laser crystal length, and the ratio of  $P_t/P_g$  will increase. Another method is to make the grating structure on a thick enough film so that  $\beta_m$  has a semi-continuous spectrum. Once outside of the coupling region, the film may be tapered down to a lesser thickness if desired. The problems here are that it may be difficult to obtain large coupling coefficients in thick films and that there will be mode conversion loss if the waveguide mode excited is not the mode wanted.

### 5.4 Grating Fabrication

The standard method of creating fine gratings such as those discussed here is to generate a photoresist grating by exposing to the interference pattern of two laser beams (an interferometer) and subsequently transferring the grating into the sample surface by either ion milling or

chemical etching. If the ratio  $\delta/\lambda$  is small, chemical etching is an easier method. If the sample is coated with a film of an easily dissolvable material before the photoresist grating is made and etched, the resultant grating depth  $\delta$  will be just the thickness of the film coating, a quantity that is easily controllable.

We have undertaken construction of a system to expose very fine gratings in photoresist by holographic methods. The general physical arrangement is shown in Fig. 5.7. The beam from a helium-cadmium laser which can operate at either 4416 Å or 3250 Å is partially filtered, expanded, and re-collimated. To produce a  $\approx 1$ " diameter beam with a uniform phase front, the beam is split by a 50-50 beam splitter and the two beams are allowed to interfere on a sample coated with photoresist. In order that the interference fringes stay fixed with respect to the sample during exposure, it is necessary to place the entire set-up on a vibration isolation table. The system should be capable of generating gratings with periods of  $\approx 5 \mu\text{m} - 0.18 \mu\text{m}$ . If prism techniques were used, gratings with periods as small as  $0.1 \mu\text{m}$  could be made. Such a system has recently been completed and Fig. 5.8 shows the electron-micrograph of a Shipley photoresist grating so produced on a silicon substrate. The periodicity is 4750 Å. The "pincushion" distortion that is apparent when the Figure is viewed in a direction parallel to the grating lines is not a property of the grating; it arises in the SEM optics.

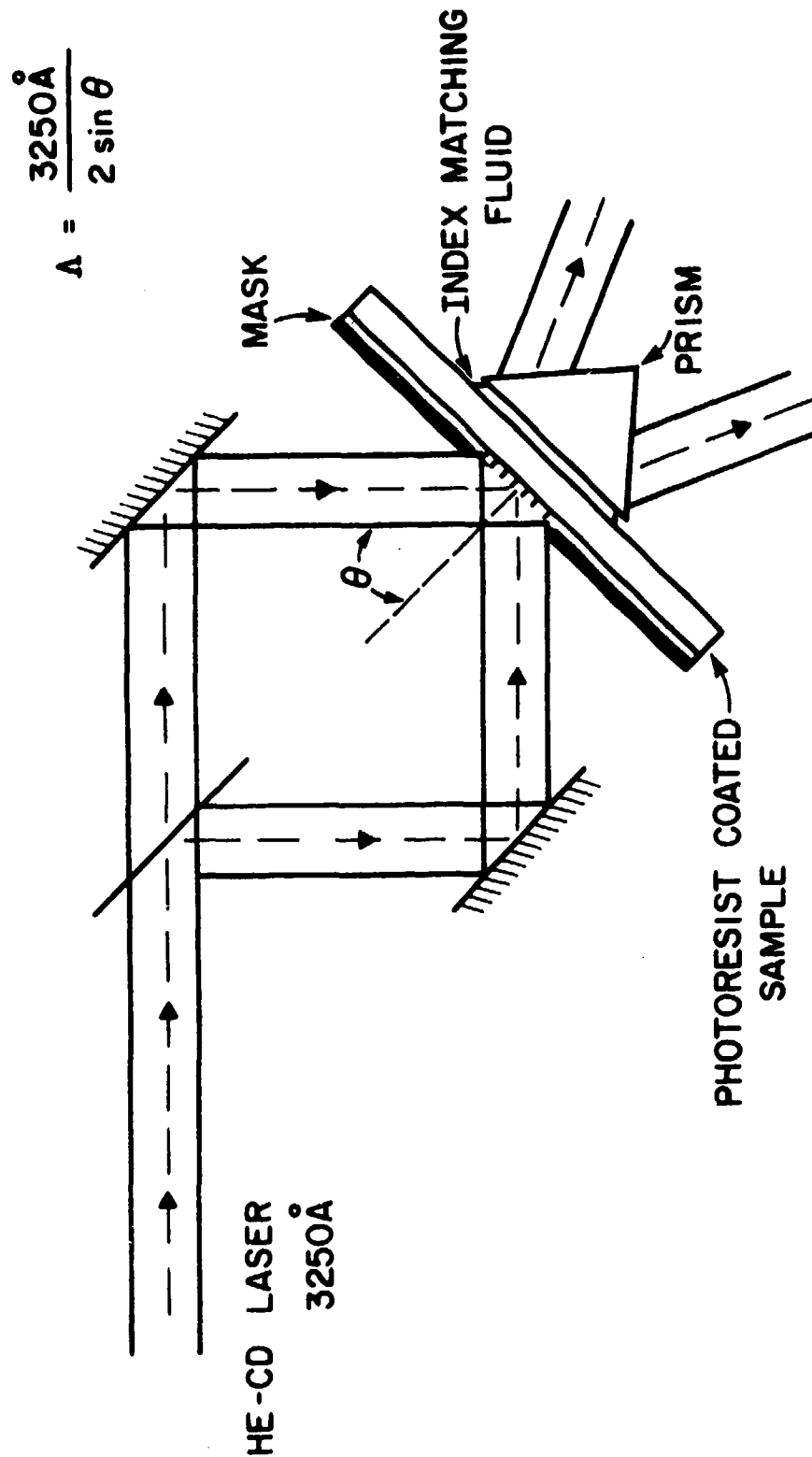


Fig. 5.7 Interferometer arrangement for producing gratings.

Reproduced from  
best available copy.

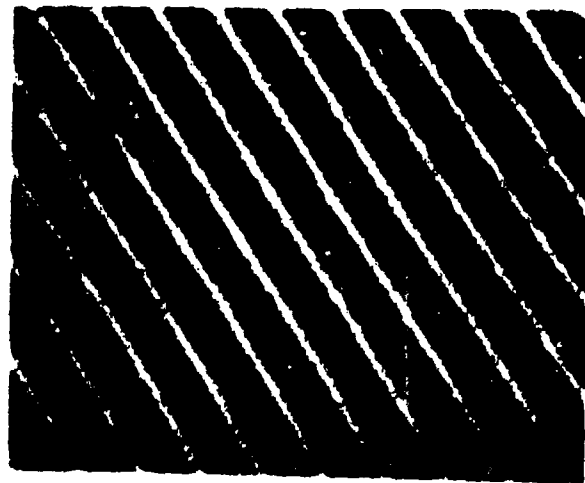


Fig. 5.8 SEM photograph of grating produced on photoresist. Grating period is  $4750 \text{ \AA}$ .

## VI. PREPARATION OF FEED MATERIALS FOR CRYSTAL GROWTH

Two important properties of laser materials affected by impurities are fluorescent lifetime of the active species and susceptibility of the host crystal to damage by the pump and laser radiation. To achieve the required improved purity levels, nearly all of the feed materials for crystal growth must be purified. In addition, almost all of the auxiliary chemicals used in the processes, as well as equipment and laboratory air, must be specially cleaned.

### 6.1 Clean Room

The fundamental requirement of a contaminant-free work area has been met through use of the Class 100 Clean Chemical Laboratory for as much of the processing as is possible. All of the air entering this laboratory is filtered and maintained at a positive pressure with respect to the outside. The work areas are semi-enclosed and are further protected from inboard contamination by the flow pattern of the filtered air. Great care is taken to maintain the integrity of the room by restricting contaminant-shedding equipment to the barest minimum and by limiting access to the users. Clean room operation was recently disrupted by equipment failure caused by premature aging of the air filter<sup>\*</sup> sealant, which resulted in a complete loss of filtration capacity. The problem has been corrected and the experience has heightened our awareness of the frailties of clean room operation.

### 6.2 Chemicals: Purification and Synthesis of Oxide Feeds

Purified feed for both oxide and fluoride crystals has been synthesized and the procedures share many common features. The following

---

<sup>\*</sup> Manufactured by Flanders Filters, Inc.

discussion will deal with oxide preparation while the special details of fluoride synthesis will be the subject of another section. Typically, each component of the oxide melt from which crystals are grown is made separately as either an oxide or a carbonate which decomposes to the corresponding oxide at elevated temperatures.

#### 6.2.1 Water, Acids and Ammonia

We have at our disposal a source of ultra-high-purity water, prepared from distilled water feed by an ion exchange-organic removal-membrane filtration system in a tin and Teflon system. This water is used in virtually all operations where water is required except in preliminary washing of dirty glass and plastic ware. Hydrochloric and nitric acids and aqueous ammonia are sufficiently pure for the current applications. Carbon dioxide and hydrogen fluoride are obtained from cylinders as gases.

#### 6.2.2 Calcium Carbonate

Commercial reagent grade calcium salts are typically contaminated with alkali metals, other alkaline earths and heavy metals. The main purification effort was directed at the heavy metals; the alkali metals are separated when the final product calcium carbonate is precipitated and filtered; and the alkaline earths were considered not to be impurities - magnesium, of course, is another component of CAMGAR.

A convenient starting material is reagent grade  $\text{CaCl}_2 \cdot 2\text{H}_2\text{O}$ . This is dissolved in water at the rate of  $\sim 450$  g/l. An insoluble residue consisting of fibers, paper, black specks and iron oxide is removed by filtration. The solution is then further purified by solvent extraction at pH1, then 7 and finally  $\sim 10-11$  with diethylammonium-diethyldithiocarbamate (DDDC) dissolved in chloroform. This reagent forms chloroform soluble chelates with a broad spectrum of heavy metals, and in combination with

distribution equilibria strongly favoring the chloroform phase allows rapid and extensive purification of the  $\text{CaCl}_2$  solution. The next step, synthesis of  $\text{CaCO}_3$ , is done by precipitation with ammonia carbonate solution. Reagent grade ammonium carbonate is used and must be pre-purified by coprecipitation with  $\text{CaCO}_3$  as the collector which is formed in situ by adding a few ml of purified  $\text{CaCl}_2$  solution to several liters of nearly saturated  $(\text{NH}_4)_2\text{CO}_3$  solution. The small amount of precipitate is filtered off and tested for heavy metals. Coprecipitation is repeated until tests do not indicate metallic contamination.

Formation of  $\text{CaCO}_3$  is accomplished by slowly adding purified  $(\text{NH}_4)_2\text{CO}_3$  to the well stirred purified  $\text{CaCl}_2$  solution until precipitation is complete. The precipitate is collected on an acid washed PTFE filter disc in a plastic Büchner funnel. Care is taken not to suck the filter cake dry. Rather, separation of the aqueous phase is accomplished by centrifugation of the filter funnel basket. An ICE type K centrifuge equipped with a four place head with one-liter cups is used. The plastic bottles designed for these cups are cut off below the shoulder and serve as containers for the funnel basket which is supported on an inverted plastic beaker which has a vent hole in its bottom. Saran wrap secured with a rubber band is used to cover the container. This assembly must be dynamically balanced with a similar unit. Thus two funnels full of precipitate are simultaneously centrifuged dry. The  $\text{CaCO}_3$  precipitate is then washed while on the funnel, using centrifugal action, until the washings are chloride-free. The centrifugal method results in a considerably better separation of precipitate from the supernatant liquid than does conventional vacuum filtration.

As a final step, the  $\text{CaCO}_3$  is dried to a constant weight in a heated

vacuum desiccator. The product, anhydrous  $\text{CaCO}_3$ , is assayed by decomposing it at  $1000^\circ\text{C}$  and weighing it as the oxide. A purity check is also made by dissolving a 10-gram sample in concentrated  $\text{HCl}$ , noting the color of the solution. Fe and Cu--likely recontaminants--give yellow solutions, even when present in trace amounts. Extraction tests with DDDC are also performed.

#### 6.2.3 Magnesium Carbonate

The procedure for magnesium follows closely that for  $\text{CaCO}_3$ . Reagent grade  $\text{MgCl}_2 \cdot 6\text{H}_2\text{O}$  is the starting material and the ammonium carbonate used is purified by coprecipitation with  $\text{MgCO}_3$ .

The magnesium carbonate formed in this process, however, has a tendency to be sticky, to cake when dried, and has a very low bulk density. Recrystallization from bicarbonate solution formed under  $\text{CO}_2$  pressure has been used to improve its physical characteristics. Very well crystallized single phase  $\text{MgCO}_3 \cdot 3\text{H}_2\text{O}$  was obtained.

#### 6.2.4 Rare Earth Oxides

The purity of commercial rare earth oxides as stated by the manufacturer (6 - 9's, 5 - 9's, etc) refers only to the other rare earths, and purification of these oxides is, therefore, necessary. The starting materials are commercial rare earth oxides. About 100 grams of oxide are dissolved in concentrated  $\text{HCl}$  to form a solution of the chloride. This is diluted to about one liter, the acidity adjusted to about pH1, and extraction is performed with DDDC in chloroform. The extraction is repeated from a less acidic solution at the pH bounded by  $\text{RE}(\text{OH})_3$  formation (pH 3.5 - 4).

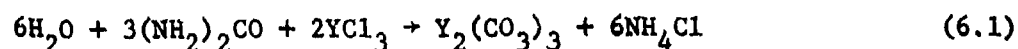
The combined DDDC extracts from 100 grams of  $\text{Er}_2\text{O}_3$  were analysed by x-ray fluorescence and were found to contain Fe, Cu, Pb and Zn as major



constituents. It is expected that other rare earth oxides are similarly contaminated.

Conversion to the oxide goes via the rare earth oxalate which is easily precipitated with oxalic acid in a dense, easily filtered form. Reagent grade oxalic acid is purified by solvent extraction with DDDC in chloroform. The rare earth oxalate precipitate is filtered and washed, using the centrifuge. Calcining the oxalate in an acid-washed silica tray at 1000°C in a clean muffle furnace effects conversion to the oxide. Avoidance of recontamination during the conversion of oxalate to oxide is difficult and direct use of an oxalate as crystal growth feed (as is done with carbonates) sometimes leads to attack of the Pt crucible, probably by the decomposition products C and CO. A rare earth carbonate would be a more desirable feed material, but simple mixing of ammonium carbonate and rare earth chloride solutions yields a poorly crystallized difficultly filtered product which is not reliably improved when digested under CO<sub>2</sub> pressure.

Very well crystallized yttrium carbonate has been synthesized by a homogeneous precipitation method using urea under CO<sub>2</sub> pressure. The overall reaction is



The reaction rate is low; therefore, the nucleation rate and free CO<sub>3</sub><sup>2-</sup> concentration are low, favoring formation of large crystallites. By running the reaction at about 12 atm CO<sub>2</sub> pressure, alkaline earth carbonates which form appreciably soluble bicarbonates should be efficiently separated from the rare earths.

Yttrium carbonate prepared by this procedure was dense and showed no trace of stickiness. The crystallites were on the order of 0.02 mm in

size, transparent, and gave an X-ray powder pattern with sharp, well-defined lines, which showed resolution of  $\text{CuK}_{\alpha_1}$  and  $\text{K}_{\alpha_2}$ . Agreement with published data was excellent.<sup>11</sup> Regarded as significant is the formation of this precipitate from 0.5 molar  $\text{YCl}_3$  solution, which means that yield and throughput need not be sacrificed to obtain a well crystallized product. Previous work<sup>11</sup> on homogeneous precipitation used 0.0002 to 0.0010 mole % solutions. When fully developed the carbonate process will replace the oxalate route for production of rare earth carbonates.

#### 6.2.6 Nickel Carbonate

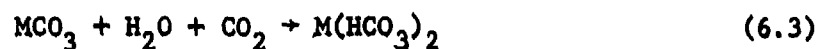
High purity nickel carbonate was synthesized from commercial high purity nickel metal. A nitrate solution prepared by dissolving the metal in reagent grade nitric acid was made basic with an amount of ammonia equivalent to the formation of  $\text{Ni}(\text{OH})_2$ . Reaction of this solution with  $\text{CO}_2$  under pressure produced crystalline nickel carbonate in moderate yield. Almost all of the nickel remaining in solution was in the form of nickel-ammonia complex ions, while a small fraction was in the form of nickel-bicarbonate species. Nickel ions are completely soluble in ammonium carbonate as nickel-ammonia complexes. Pressurization with  $\text{CO}_2$  decreases the pH and the dissolved  $\text{NH}_3$  concentration, allowing precipitation of  $\text{NiCO}_3$ .

#### 6.2.6 Chemical Synthesis under $\text{CO}_2$ Pressure

The solubility of many carbonates in water is greatly increased when the solution is saturated with  $\text{CO}_2$ . Two contributing effects are reduction of the  $\text{CO}_3^{=}$  ion concentration via reaction with dissolved  $\text{CO}_2$ .



and formation by metal ions of soluble bicarbonate complexes.



(M = Mg, Ca, Ba, Ni, etc.)

The actual bicarbonate species predominating will differ from metal to metal. In a solution saturated with  $\text{CO}_2$  at  $\sim 12$  atm, the solubility of  $\text{MgCO}_3 \cdot 3\text{H}_2\text{O}$  appears to be about 40 g/l. At the ambient  $\text{CO}_2$  pressure,  $\text{CO}_2$  loss is quite slow; even vacuum filtration with a water pump does not engender decomposition. When heated to  $50 - 60^\circ\text{C}$ ,  $\text{CO}_2$  is evolved and fine needles of  $\text{MgCO}_3 \cdot 3\text{H}_2\text{O}$  precipitate. This material is still fluffy but considerably denser than directly formed  $\text{MgCO}_3$ , easily filtered and separated from the mother liquor, and forms a free-flowing powder when dry.

Using the  $\text{CO}_2$  reactor, ammonium carbonate is formed in situ, eliminating the need for purifying this compound. Purified  $\text{MgCl}_2$  solution is mixed with an equivalent amount of aqueous ammonia which partly precipitates  $\text{Mg}(\text{OH})_2$ . Carbonation of this mixture yields a precipitate of  $\text{MgCO}_3 \cdot \text{XH}_2\text{O}$  and a solution containing magnesium bicarbonate and ammonium chloride. Heating the solution, after removal from the reactor, precipitates the rest of the magnesium. This raw magnesium carbonate is then separated from the aqueous phase and washed in a pair of 1-liter centrifuge bottles, then returned to the pressure reactor and recrystallized from pure  $\text{CO}_2$  charged water.

It has been observed that DDDC in chloroform will extract heavy metal impurities from a saturated magnesium bicarbonate solution. That commercial reagent grade magnesium carbonate can be purified directly through extraction and crystallization of bicarbonate solutions, avoiding the chloride precursor and use of large amounts of aqueous ammonia, seems entirely reasonable. Such a purification route, by reducing handling and

use of auxiliary reagents should lead to improved purity of the product.

Extension of high pressure  $\text{CO}_2$  chemistry to purification of other substances is feasible. Calcium, Ba and Sr form soluble bicarbonates, while the alkali metals, for example, can be recrystallized by precipitation of the bicarbonate under  $\text{CO}_2$  pressure. It has also been shown that  $\text{CO}_2$  under pressure is an aid to the formation of crystalline rare earth carbonates, and can be used in preparation of nickel carbonate.

### 6.3 Rare Earth Fluorides

Spectroscopic studies in  $\text{LiRbF}_4$  compounds have suggested that trace rare earths can be significant impurities. Zone-refining of  $\text{LiREF}_4$  has proven to be a successful purification technique. For example, repeated zone-refining of  $\text{LiErF}_4$  resulted in a monotonic increase in lifetime of the  $^4\text{I}_{13/2}$  state from 2.3 msec after 5 passes to 8.5 msec after 28 passes. Fluorescence measurements also indicate removal of Ho and Tm as the zone-refining progresses. Wet chemical separation of heavy metals from  $\text{ErF}_3$  has also resulted in an increased lifetime in  $\text{LiErF}_4$ .

Bulk synthesis of  $\text{REF}_3$  compounds from the respective carbonates has been carried out by hydrofluorination in undiluted HF gas at  $300^\circ\text{C}$  in a Teflon reactor. The oxide content of the fluoride produced is roughly dependent on the hydroxy contamination in the starting carbonate. Therefore, well crystallized single phase  $\text{RE}_2(\text{CO}_3)_3$  is essential to successful synthesis of  $\text{REF}_3$ . Purification and synthesis of the required  $\text{RE}_2(\text{CO}_3)_3$  compounds was discussed in the section on rare earth oxides.

### 6.4 Continuing Work

Improvements in purification procedures are always possible. Particulate contamination in solutions is a recognized problem which can be met by filtering all solutions through sub-micron membrane filters.

Such a system will be installed in the near future.

When it becomes necessary, rare earth chlorides will be prepurified by zone-refining to reduce the trace rare earth contamination prior to conversion of the chloride to carbonate.

Come chemical reagents and feed materials ( $B_2O_3$ ,  $GeO_2$ ) are used without purification. As further developments in the growth of high purity crystals are made, these substances, too, will require purification.

## VII. SPECIAL FACILITIES AND STUDIES

### 7.1 Clean Oxide Crystal Growth Furnace

Although we intended from the beginning of our program to work on oxide as well as fluoride laser hosts, a serious start on oxides had to be deferred until completion of our clean air chemistry laboratory and the development of techniques for ultrapurification of oxide feed materials. Now that there has been success in improving feed purity we must take the next important step: the design and construction of new types of furnaces which avoid recontamination of the feed materials from the furnace itself.

The first of these furnaces, now operational, is shown in Fig. 7.1. The proven source is a 20 kW Lepel RF generator coupling to a cylindrical, thick-walled platinum crucible. The furnace consists of a water-cooled metal bell jar, with two viewing ports, mounted on a drill stand base which also supports the pulling and rotation mechanism. The seed rod is accurately aligned so that the rod cannot bind in the bushing during crystal pulling. The base of the unit supports the platinum crucible, which is surrounded by an alumina sheath consisting of protecting alumina tubes and alumina crucibles. The platinum crucible is insulated with high purity alumina powder. The RF energy is led into the furnace from the power supply by means of a water-cooled RF feedthrough. The high voltage side of the RF is insulated from the furnace by a protective Teflon sleeve. A means of raising and lowering the base of the furnace is provided by a jack mechanism. The furnace has been designed to hold a controlled atmosphere of pre-purified gases, of which nitrogen and oxygen will be the principal components.

### 7.2 Refractive Index of $\text{LiYF}_4$

The index of refraction of  $\text{LiYF}_4$  was measured over the wavelength

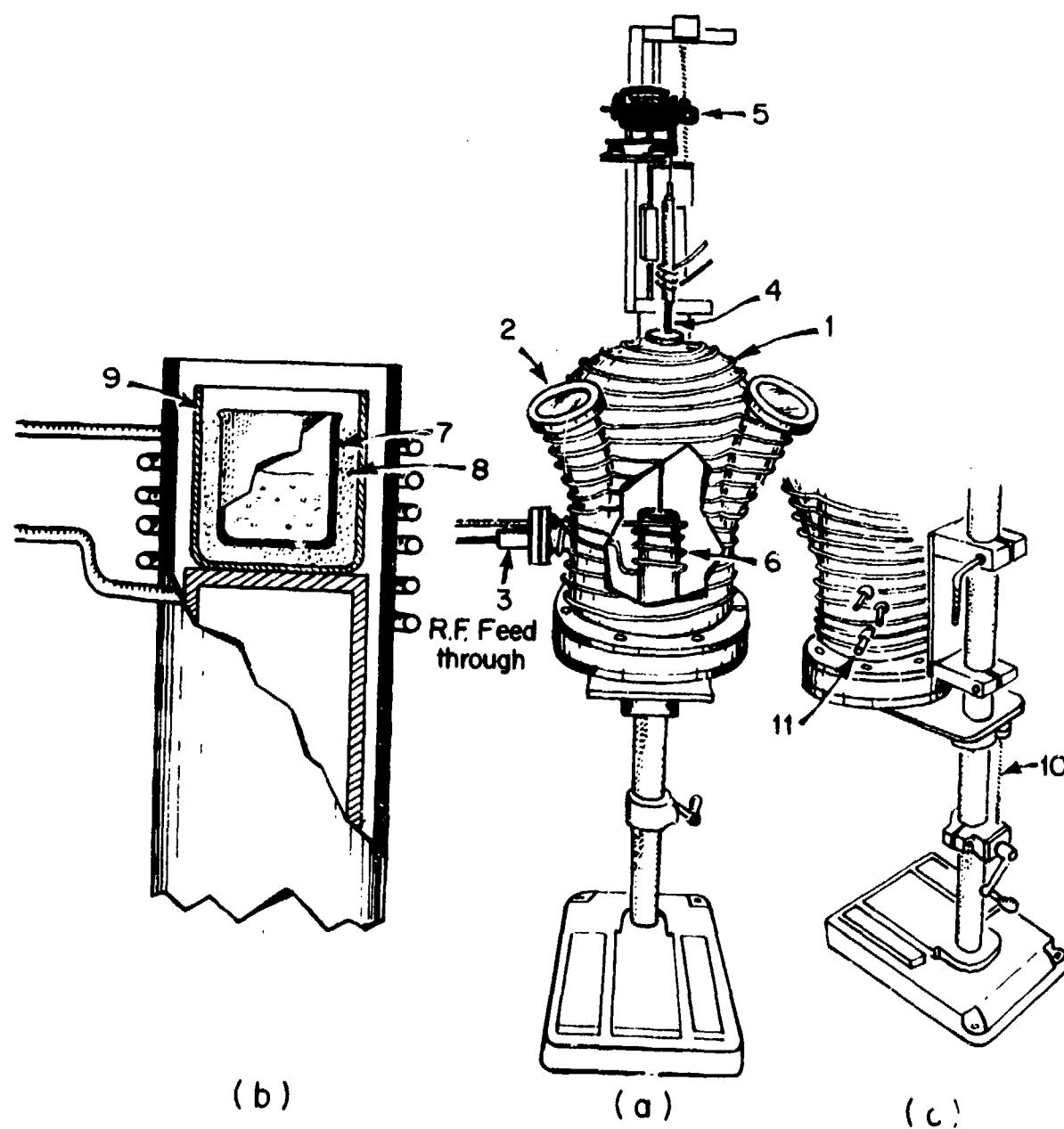


Fig. 7.1 Controlled Atmosphere RF top seeded solution growth furnace.

- (a) Overall view: (1) belljar (2) viewing ports (3) RF feedthrough  
(4) seed rod (5) rotating motor (6) RF coil
- (b) Detail: (7) Pt crucible (8) high purity alumina grog  
(9) alumina crucible
- (c) Detail: (10) crucible lowering (11) gas inlets and outlets

range of  $0.225 \mu$  to  $2.6 \mu$ .<sup>\*</sup> The results are shown in Table 7.1 and Fig. 7.2. The indices were measured by the method of minimum deviation on a spectrometer similar to one described by Bond,<sup>12</sup> A large (1.4 cm side) prism of undoped  $\text{LiYF}_4$  was used. The accuracy of these index measurements is  $\Delta n = 0.0002$ . Previously published<sup>13</sup> index data on the visible index of refraction appear to be in considerable error.

---

\*This work was done in collaboration with Sanders Associates and will also be reported by them under their contract F33615-74C-1194.



Table 7.1  
Refractive Index of YLF  
 Index Tolerance  $\pm 0.0002$

Wavelength $\mu$	$n_e$	$n_o$
2.600	1.4602	1.4381
2.400	1.4617	1.4397
2.200	1.4632	1.4411
2.000	1.4645	1.4424
1.800	1.4658	1.4437
1.600	1.4670	1.4449
1.400	1.4681	1.4460
1.200	1.4693	1.4471
1.000	1.4708	1.4485
.900	1.4716	1.4492
.800	1.4726	1.4502
.700	1.4741	1.4516
.600	1.4762	1.4535
.500	1.4796	1.4567
.450	1.4822	1.4590
.400	1.4858	1.4624
.350	1.4913	1.4674
.300	1.5001	1.4754
.250	1.5156	1.4895
.225	1.5287	1.5014

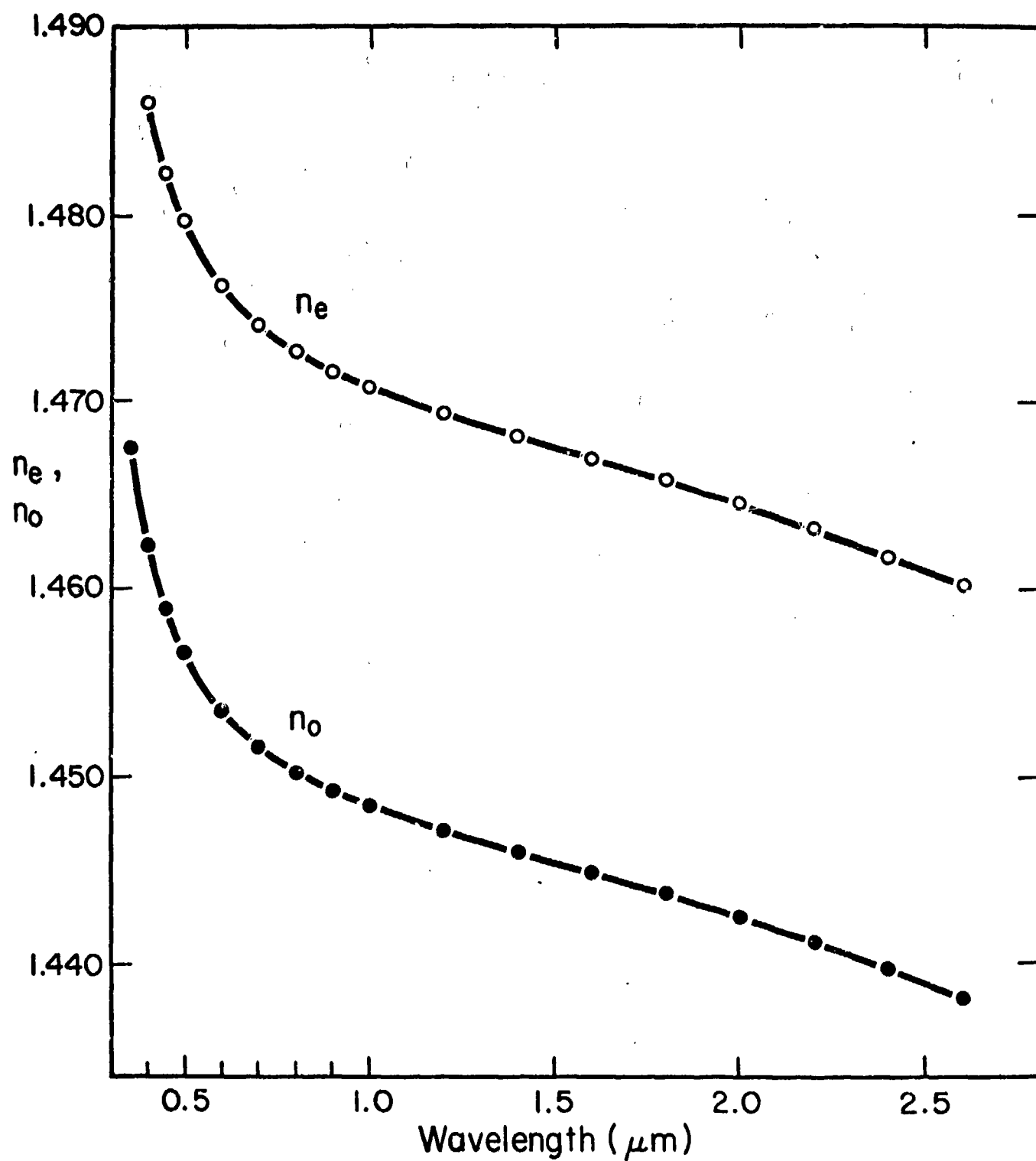


Fig. 7.2 Wavelength dependence of the ordinary and extraordinary refractive index of  $\text{LiYF}_4$ .

VIII. REFERENCES

1. Semi-Annual Technical Report No. 2.
2. F. W. Ostermayer, Jr., et al., Phys. Rev. B. 3, 2698 (1971).
3. L. F. Johnson, R. E. Dietz, and H. J. Guggenheim, Phys. Rev. Letters 11, 318 (1963).
4. W. R. Klein, B. D. Cook, IEEE Transactions on Sonics and Ultrasonics, SU-14, No.3, 123 (1967).
5. F. S. Cher, J. E. Geusic, S. K. Kurtz, J. G. Skinner, S. H. Wemple, J. Appl. Phys. 37, No.1, 388 (1966).
6. S. H. Wemple, D. Kahng, H. J. Braun, J. Appl. Phys. 38, No. 1, 353 (1967).
7. J. H. Van der Merwe, J. Appl. Phys. 34, 123 (1963).
8. S. H. Wemple, "Symposium on Ohmic Contacts to Semiconductors"; Editor, B. Schwartz; Electrochemical Soc. 1969; pp. 128-137.
9. K. Ogawa, W. S. C. Chang, B. L. Sopoior, F. J. Rosenbaum, J. of Quantum Electronics (IEEE) QE9, 29 (1973).
10. J. H. Harris, R. K. Winn, and D. G. Dalgoutte, Applied Optics 11, 2234 (1972).
11. K. Nakashima, et al., Bull. Chem. Soc. Jap. 46, 152 (1973).
12. W. L. Bond, J. Appl. Phys. 36, 1674 (1965).
13. W. A. Shand, J. Crystal Growth 5, 143 (1969).

IX. PUBLICATIONS AND PAPERS PRESENTED AT MEETINGS

1. "Single Mode 2.06  $\mu\text{m}$  Miniature Laser", D. Castleberry, H. P. Jenssen and A. Linz; presented at the Integrated Optics Conference, New Orleans, January 1974.
2. "Growth and Characterization of Silicon Doped  $\text{GaAs}_{\text{x}}\text{Sb}_{1-\text{x}}$  Luminescent Diodes", S. K. Brierley and C. G. Fonstad, Jr.; presented at the 1974 IEEE Specialist Conference on the Technology of Electroluminescent Diodes, November 20-21, 1974, Atlanta, Georgia.
3. "Analysis of the Optical Spectrum of  $\text{Tm}^{3+}$  in  $\text{LiYF}_4$ ", H. P. Jenssen, A. Linz, P. Leavitt, C. A. Morrison and D. E. Wortman; to be published in Phys. Review B, January 1, 1975.
4. "Efficient Silicon Doped  $\text{GaAs}_{\text{x}}\text{Sb}_{1-\text{x}}$  Luminescent Diodes Emitting to 1.06  $\mu\text{m}$ ", S. K. Brierley and C. G. Fonstad, Jr.; to be presented to Applied Physics Letters.
5. "Epitaxially Grown Single Crystal KTN for Thin Film Optical Modulators", R. E. Fontana, D. J. Epstein, A. Linz; submitted for presentation at the 1975 CLEA Conference.

## SEMI-ANNUAL TECHNICAL REPORT #3

Period: July 1, 1974 - December 31, 1974

Title: Research in Materials Sciences

Project Title: Superconducting Transition Metal Alloys

Contract Number: DAHC 15-73-C-0316

ARPA Order Number: 2469

Program Code Number: 3D10

Name of Contractor: Massachusetts Institute of Technology  
Cambridge, Mass. 02139

Principal Investigator: N. J. Grant (617) 253-5638

Project Scientists or Engineers: R. M. Rose (617) 253-3230

M. L. A. MacVicar (617) 253-6261

J. L. Bostock (617) 253-7607

Effective Date of Contract: June 1, 1973

Contract Expiration Date: May 31, 1975

Amount of Contract: \$770,233.

Amount of Project: \$223,834.

Sponsored By

Advanced Research Projects Agency

ARPA Order No. 2469

The views and conclusions contained in this document are those of the authors and should not be interpreted as necessarily representing the official policies, either expressed or implied, of the Advanced Research Projects Agency or the U. S. Government.

## Summary

The objectives of this project continue to be:

- (a) Extraction of the basic parameters for Al<sub>5</sub> superconductivity by the tunneling technique;
- (b) Development of appropriate surfaces and tunneling barriers for the above Al<sub>5</sub> substrates;
- (c) Development of improved surfaces, materials, and surface treatments for superconducting microwave devices.

In this report we describe our progress towards the second objective. Specifically, we present the results of the phase of our work directed towards possible exploitation of thin amorphous carbon film layers as tunneling barriers on Al<sub>5</sub> superconducting materials. This work is in two parts. The first part concentrates on the electronic conduction properties of bulk amorphous carbon films and the relationship of these properties to fabrication history. In the attached thesis by Jimmie Lee Jones, Jr., we present the detailed results of a systematic investigation of the effects of fabrication conditions and variables on the observed resistivity behaviors of arc-evaporated amorphous carbon films. The second part of our work (to be completed in the near future) will comprise the thesis of Keith Milkove and concerns the properties of both arc-evaporated and electron-beam evaporated amorphous carbon films sandwiched between metal electrodes to form a tunneling barrier.

In fabricating acceptable tunneling barriers for application to

superconducting materials of interest, especially the Al5's, we have passed several self-imposed tests. For example, we have obtained superconducting tunneling characteristics for In-C-In thin film junctions; these characteristics yielded good energy gap values for the indium. We have obtained several useable curves on  $\text{Nb}_3\text{Al}$ -Ge bulk and film substrates; a substantial number of very good characteristics on tin film substrates; tantalizing characteristics on three gold film substrates (which suggest that the nature of the metal-carbon interface is important!); and a long sought set of density-of-states data on superconducting lead-impregnated porous glass. This last set of tunneling characteristics is particularly pleasing because we had previously exhausted conventional oxidation techniques on this vycor surface without success. Thus the amorphous carbon barrier facilitated a measurement we were not otherwise able to obtain.

We have established the four general criteria, given below, for predicting when carbon barrier junctions will exhibit acceptable superconducting tunneling characteristics.

1. There is a definite range of film color corresponding to good junctions. This range is narrow and is recognizably brown. (A spectrum color chart is in preparation.)
2. For junction areas of  $\sim 5 \text{ mm}^2$ , junction resistance must fall in the range of 10 - 1000 $\Omega$  in order of magnitude.
3. The temperature behavior of the junction as determined by a four-point probe should be that of a positive 1-V slope at room

temperature changing into a negative I-V slope by liquid nitrogen temperatures.

4. The magnitude of the junction resistance should increase by four or five powers of ten between 77°K and 4.2°K.

This is probably not a complete listing of salient criteria, e.g., an account of electrode oxidation free energy is not yet included. However, these do seem to constitute a necessary set of conditions; that is, we do not observe tunneling in junctions that violate the criteria.

Junctions are still not as rugged as we would like. Whether the reason for this is actual mechanical fragility, aging, electrical and magnetic field dependence effects, or a combination of all three, is not yet known. Quite possibly an improvement could be made by going to a more paracrystalline amorphous carbon; i.e., a more diamond-like layer such as formed by ion-beam deposition.

## I. Introduction

The importance of understanding the A15 group of materials stems from the fact that they have the highest known transition temperatures. Our approach to the problem is to perform high quality tunneling experiments on the A15's with the highest  $T_c$ 's and to develop the computer software appropriate to deconvoluting this data into meaningful A15 phonon spectra. Central to the success of any tunneling investigation on any material is the development of appropriate laboratory expertise and



technology concerning fabrication of high quality tunneling barriers on the substrate of interest. The Al5's are a particularly severe challenge to state-of-the-art surface oxidation technology and understanding. Our approach to barrier fabrication on Al5's has been two-fold in its emphasis. First we have sought to systematically pursue and exhaust state-of-the-art natural surface oxidation procedures, sometimes in new combinations or permutations. Various air and oxygen thermal oxidation procedures, glow discharge oxidation in partial pressures of oxygen under vacuum, anodization, and acid etching techniques are all avenues we have explored and are exploring. (With respect to Nb<sub>3</sub>Al-Ge, in particular, natural oxide barriers seem increasingly more promising when the substrate surface is increasingly less representative of the bulk alloy.) Therefore, in parallel to the natural oxide effort, we have made a significant laboratory commitment to fabricating artificial (or non-natural oxide) barriers on superconducting substrates. It is well known that a semiconductor layer of even substantial thickness (100 - 1000 Å) can perform as an effective and useful tunneling barrier between simple metals (e.g., Cu, Sn, Pb) at cryogenic temperatures<sup>1</sup>. However, the relationships between final properties of the barrier and parameters of fabrication (e.g. deposition rate, thickness, pressure, substrate species) were not at all understood before we undertook to determine them in the case of amorphous carbon film barriers.

We have studied the electronic properties of both arc-evaporated and electron-beam deposited amorphous carbon thin films. In the arc-

evaporated case, we concerned ourselves not only with the behavior of a film as the barrier element in a metal-carbon-metal sandwich configuration system, but also with the behavior of a film as an isolated, individual bulk element (see attached thesis by Jimmie Lee Jones, Jr.). In the electron-beam deposited case, we concentrated extensively on the sandwich configuration and wide application of it to different substrates.

## II. Results

Arc-evaporation rates of  $2 \text{ \AA/sec}$  to  $150 \text{ \AA/sec}$  were used to produce carbon films of thickness ranging from  $\sim 50 \text{ \AA}$  to  $1600 \text{ \AA}$ . It is of particular significance to tunneling barrier applications that the observed film resistivity was inversely dependent on deposition rate below approximately  $10 \text{ \AA/sec}$ , and relatively independent of rate above this threshold. A similar behavior of rates and resistivity was observed in electron-beam deposited films. Fast deposition rate resistivities are too low ( $\sim 1 \Omega\text{-cm}$ ) for observing the tiny superconducting gap structure impressed on the high current contribution from the carbon itself in the junction's I-V characteristics. Slow deposition rate resistivities are often well-beyond the impedance capabilities of laboratory instruments ( $10^5 - 10^6 \text{ ohm}$ ), and make the observation of a superconductor's energy gap edge impossible. An experimenter must, therefore, try for a rate of deposition that falls in the rather narrow band of values, 8 to  $15 \text{ \AA/sec}$ .

A secondary influence on the resulting resistivity value obtained is the vacuum pressure during fabrication. We varied pressure from the

low  $10^{-5}$  range to the high  $10^{-2}$  range during controlled-rate fabrication of arc-evaporated carbon films. Generally, an order of magnitude increase in vacuum pressure (e.g., from outgassing) yielded an order of magnitude increase in film resistivity. For this reason, electron-beam deposition is considerably more advantageous than is arc-evaporation with respect to control of background pressure during fabrication. The final thickness of the carbon film also is a secondary influence on its resistivity, at least for very thin films ( $< 150 \text{ \AA}$ ). Up to some modest thickness value which is higher for electron-beam deposited films than for arc-evaporated films, resistivity varies proportionally to thickness for a given deposition rate.

We further observe that a strong correlation exists between the color of an amorphous carbon film and its electrical conduction properties. This correlation is powerful in its capacity to sort through numerous sample films prepared by varying researchers, by different evaporation procedures, according to different deposition rates and other fabrication parameters, and to predict accurately film resistivity, and indirectly, the temperature behavior of this resistivity.

The amorphous nature of our carbon films is remarkable. TEM studies of our arc-evaporated films show no crystallinity exists even on a scale of  $\sim 20 \text{ \AA}$ . Temperature dependence investigations of the resistivity of our films confirm that  $\rho$  behaves as a Mott-like amorphous semiconductor ( $\log \rho \propto T^{-1/4}$ )<sup>2</sup>. Preliminary Raman scattering studies on sputtered carbon films prepared at IBM-Watson Laboratory for comparison to ours

were equally impressive<sup>3</sup>. (In fact, the scattering profile set a new definition of amorphousness in that laboratory's studies.) Non-crystallinity is particularly prized in tunneling experiments, e.g. anisotropy studies, where it is crucial that k selection rules operating at the substrate-barrier interface be fundamental to the substrate<sup>4</sup>. It was comforting to find that there was essentially no microstructure in carbon films prepared by any of the conventional methods: evaporation, sputtering, and electron beam.

### III. Special Comments

The most intriguing property we observe in our carbon films is a time-rate of change of their resistivities under sustained electric field. In particular, in the sandwich geometry the carbon layer exhibited continuous changes in resistivity over individual testing periods of approximately one to two hours of applied bias. One manifestation of this change was an increasing smoothing of the electrode superconducting density of states as the increasing excess current caused by the changing barrier resistivity began to dominate the signal. There were also other manifestations in the form of structure seemingly related to the barrier itself, not the electrodes. These kinds of behavior were observed for several electrode species, including bulk  $\text{Nb}_3\text{Al-Co}$ <sup>5</sup>. The effect was distinct from aging, which we also observed in both bulk film and sandwich geometries. The field-dependent resistivity behavior seems related to a second property sometimes observed in our sandwich geometries. In these cases, over a few minutes or hours and once even over 46 days, the

barrier experienced "break-up" under applied bias. The term breakdown refers to the sudden decrease in resistivity of a sandwiched dielectric layer. In the case of our carbon, the resistivity suddenly increased. Such behavior was observed in different combinations of electrode species.

Recently we have learned of independent observations of similar behaviors by K. Antonowicz<sup>6</sup> who worked with Al-C-Al sandwiches at room temperature. In these samples he observed a slowly decreasing resistivity under applied bias behavior as we do, and slow time response as well. He observed "break-up" when the resistivity decreased so much as to pass current in excess of a threshold current related to sandwich geometry. The voltages he noted for "break-up" were approximately 2 volts, while our electrode-carbon combinations, tested at cryogenic temperatures, exhibited "break-up" at voltages in the millivolt range. For his voltages, Antonowicz observed that application of a weak magnetic field ( $\sim 1/2$  gauss) resulted in a sinusoidally varying threshold current,  $J_{\max}$  vs.  $H$ . The response time of his junctions was hours. Our junctions were always in the earth's background field; however, our gold substrate carbon barrier junctions did respond to a larger magnetic field with a  $J_{\max}$  growing and diminishing as a function of increasing field. When we applied fields approximately 10x larger than the earth's field, we were able to drive some of our junctions out-of, and into, the break-up resistivity mode by consecutive application and turning off, respectively, of the field. Even with no applied field other than the earth's background, we occasionally observed instabilities in the junction's preferred I-V (or resistivity).

mode.

Sputtered amorphous carbon films of considerable thickness (1000 - 3000 Å) have recently been reported by Morisaki, et al.<sup>7</sup>, to switch differently at room temperature according to whether the electrodes were aluminum or copper, and according to whether a fabrication configuration was Al-C-Cu or Cu-C-Al. The carbon-aluminum interface was much more definitive in producing Morisaki's switching results than was the carbon-copper interface; the latter often exhibited no switching or memory effects, in fact. His conclusions are certainly in agreement with our observations of cryogenic temperature behaviors. We believe that it may be possible to extract from data taken on samples of different electrode species combinations and configurations, definitive information about the presence and significance of carbon-metal interface oxidation.

In summary, indications are that relatively thin amorphous carbon films prepared by one of several conventional techniques between varieties of metal electrodes can exhibit characteristics potentially useful in studying the properties of metals in both the superconducting and normal states by tunneling, and perhaps even potentially useful as hybrid superconductor/amorphous semiconductor devices.

## References

1. I. Giaever, Phys. Rev. Lett. 20, 1286 (1968); I. Giaever and H. Zeller, Phys. Rev. Lett. 21, 1385 (1968); M. L. A. MacVicar, S. M. Freaake, and C. J. Adkins, J. Vac. Sci. Tech. 6, 717 (1969); M. L. A. MacVicar, J. App. Phys. 41, 4765 (1970).
2. N. F. Mott, Adv. Phys. 16, 49 (1967).
3. Private communication, E. Alessandrini (I.B.M. Watson Laboratory).
4. J. E. Dowman, M. L. A. MacVicar and J. R. Waldram, Phys. Rev. 186, 452 (1969).
5. J. A. Gregory, J. Bostock, M. L. A. MacVicar and R. M. Rose, Phys. Lett. 46A, 201 (1973).
6. K. Antonowicz, Nature 247, 358 (1974).
7. H. Morisaki, K. Saigo, S. Shintani, and K. Yazawa, J. Non-Crystall. Sol. 15, 531 (1974).

## CONDUCTION IN AMORPHOUS CARBON \*

by

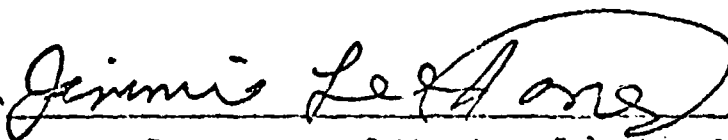
Jimmie Lee Jones

Alabama Agricultural and Mechanical University, B.S.  
(1970)SUBMITTED IN PARTIAL FULFILLMENT  
OF THE REQUIREMENTS FOR THE DEGREE OF  
MASTER OF SCIENCE  
at the

MASSACHUSETTS INSTITUTE OF TECHNOLOGY

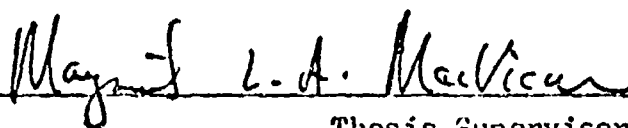
September, 1974

Signature of Author



Department of Physics, July 18, 1974.

Certified by



Thesis Supervisor.

Accepted by

Chairman, Departmental Committee on  
Graduate Students.

- \* This research supported by the National Science Foundation and the  
Advanced Research Projects Agency.



## CONDUCTION IN AMORPHOUS CARBON

by

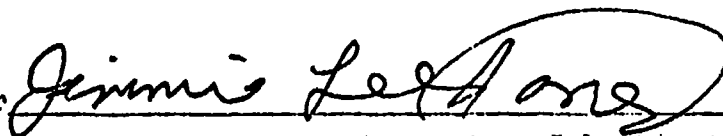
Jimmie Lee Jones

Alabama Agricultural and Mechanical University, B.S.  
(1970)SUBMITTED IN PARTIAL FULFILLMENT  
OF THE REQUIREMENTS FOR THE DEGREE OF  
MASTER OF SCIENCE  
at the

MASSACHUSETTS INSTITUTE OF TECHNOLOGY

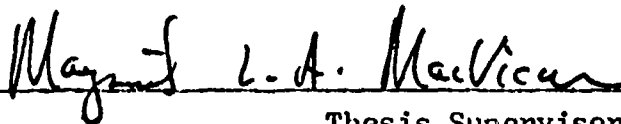
September, 1974

Signature of Author



Department of Physics, July 18, 1974.

Certified by



Thesis Supervisor.

Accepted by

Chairman, Departmental Committee on  
Graduate Students.

## CONDUCTION IN AMORPHOUS CARBON

by

Jimmie Lee Jones

Submitted to the Department of Physics on July 15, 1974  
in partial fulfillment of the requirements for the degree  
of Master of Science.

## ABSTRACT

This thesis reports and comments on resistivity sensitivity to fabrication for arc-evaporated amorphous carbon thin films of thicknesses 50<sup>o</sup>A to 1600<sup>o</sup>A. Films were deposited on room temperature glass substrates in pressures ranging from 5x10<sup>-3</sup> Torr to 5x10<sup>-5</sup> Torr, and deposition rates from 2<sup>o</sup>A/sec to 150<sup>o</sup>A/sec.

Resistivity was independent of deposition rate for films deposited at rates in excess of 10<sup>o</sup>A/sec to thicknesses in excess of 100<sup>o</sup>A. For such films deposited in 5x10<sup>-5</sup> Torr vacuum, resistivities typically ranged from .4 ohm-cm to 4 ohm-cm and were 83% reproducible to these orders of magnitude. However, resistivities varied over eight orders of magnitudes (.1 ohm-cm to 10<sup>7</sup> ohm-cm) for deposition rates less than 10<sup>o</sup>A/sec in higher vacuum pressures. For the same 10<sup>-5</sup> Torr pressure, such deposition rates gave resistivities varying over six orders of magnitude (10<sup>1</sup> to 10<sup>7</sup> ohm-cm).

Resistivity was investigated over the temperature ranges 4.2<sup>o</sup>K to 500<sup>o</sup>K. Resistivity versus temperature curves were reproducible on a given film for temperatures below the fabrication temperature, 300<sup>o</sup>K. For temperatures above this, up to the maximum investigated 500<sup>o</sup>K, hysteresis was observed in the first few heating and cooling cycles and then gradually disappeared. Room temperature resistivity dropped approximately 10 ohm-cm after the first heating and cooling cycle.

$\ln \rho$  vs  $T^{-1}$  was generally non-linear. Samples that exhibited an ill-defined activation energy for intervals in the temperature range investigated, showed linearity in  $\ln \rho$  vs  $T^{-1/4}$  for those intervals. Typical estimated activation energies at 300<sup>o</sup>K and 5<sup>o</sup>K were 50 meV and 3 meV, respectively.

TEM studies showed that all "as grown" films were structurally disordered (i.e. amorphous) on a scale of 2<sup>o</sup>A resolution. Further, the films remained disordered after a heating and cooling cycle. Resistivity, although influenced by impurities as evidenced by the pressure dependence noted, showed no apparent microstructure sensitivity over the temperature range investigated.

Chemical spectrographic analyses of the stock graphite rod and the vacuum-out-gassed rod were made. Also, residual gas analyses were made in situ on the out-gassing and out-gassed graphite rods. These various analyses confirmed the graphite rods to be of high purity, and to be non-contaminating to the vacuum atmosphere.

Many films showed no apparent aging; others, on the other hand, showed small increases as well as small decreases in resistivity. For the observed fabrication parameters, (deposition rate  $\sim 500\text{\AA}/\text{sec}$ , background pressure  $\sim 5 \times 10^{-5}$  Torr, and thickness from  $1000\text{\AA}$  to  $16000\text{\AA}$ ), no apparent relation was observed for aging versus fabrication.

Out-gassing the graphite rods, as well as pre-or post-electrode deposition relative to the carbon film, had no apparent influence on resistivity.

A total of 100 films were fabricated in this investigation, of which 75 were judged to be of suitable technological quality for data analysis. A master data summary was prepared for comparison use by future researchers.

## TABLE OF CONTENTS

Chapter		Page
	ABSTRACT	11
	LIST OF FIGURES	1
	LIST OF TABLES	5
	ACKNOWLEDGEMENTS	6
1.	INTRODUCTION	
	A. Theoretical Background	7
	B. Experimental Background	14
	C. The Current Work	18
2.	MATERIALS AND EQUIPMENT	
	A. Starting Material	19
	B. Carbon Gun And Vacuum System	19
	C. The Sample	24
	D. The Measurement System: Low Temperature	27
	E. The Measurement System: High Temperature	30
3.	EXPERIMENTAL RESULTS	
	A. Resistivity and Aging Versus Fabrication	32
	B. Resistivity as a Function of Temperature	37
	C. Resistivity and Microstructure	42
4.	COMMENTS ON RESULTS	
	A. The Measurements	59
	B. Brief Further Comparisons	65
	C. Summary	69
	APPENDIX A.	71
	REFERENCES	77

## List Of Figures

		Page
Figure 0-1A:	Density of Energy States for an Amorphous Semiconductor.	9
Figure 0-2B:	Density of States and Mobility Gap Width for a Highly Disordered Semiconductor.	10
Figure 0-3A:	Density of Energy States for a Semiconductor Crystal.	11
Figure 0-3B:	Density of Energy States for a Slightly Disordered Semiconductor.	11
Figure 1 :	Mass Spectrum of $4 \times 10^{-6}$ Torr Vacuum Chamber Before Out-Gassing the Graphite Rods.	22
Figure 2 :	Mass Spectrum of $1 \times 10^{-5}$ Torr Vacuum Chamber After Out-Gassing the Graphite Rods.	23
Figure 3 :	Carbon Evaporation Gun.	25
Figure 4 :	Substrate Holder and Slide Masks Mounted on the Pyrex Chimney. The monitor and substrate masks can be pulled along mechanical guides underneath the stationary optical quartz flat and the glass substrate.	26
Figure 5 :		28
A :	Heater for Heating Carbon Sample.	
B :	Carbon Sample Mounted in the Heater.	
C :	Ge Thermometer Mounted in Heater, on the back of the Sample.	
Figure 6 :	Sample Chamber and Cryostat.	29
Figure 7 :	Temperature Versus Time Characteristics for the Thermal Cycle of Samples.	31

- Figure 8-A : Sample # 26. 38  
 $\rho$  (T) Characteristics for Initial Heating and Subsequent Cooling.
- Figure 8-B : Sample # 30. 39  
 $\rho$  (T) Characteristics for Initial Heating and Subsequent Cooling.
- Figure 8-C :  $\ln \rho$  Vs T Characteristics for the First Four Heating and Cooling Cycles of Sample # 1. 40
- Figure 9-B :  $\ln \rho$  Vs  $T^{-1}$  Characteristics for Sample #30. 41  
 The dashed lines are the curve tangents from which the  $\Delta E$  values were estimated.
- Figure 9-A :  $\ln \rho$  Vs  $T^{-1}$  Characteristics for Sample #26. 43  
 The dashed lines are the curve tangents from which the  $\Delta E$  values were estimated.
- Figure 9-C :  $\ln \rho$  Vs  $T^{-1}$  Characteristics for Sample #7. 45  
 The dashed lines are tangents to the curve from which the  $\Delta E$  values were estimated.
- Figure 9-D :  $\ln \rho$  Characteristics for Sample # 7. 46
- Figure 10-A:  $\ln \rho$  Vs  $T^{-1}$  Characteristics for Sample #5. 47  
 The dashed lines are tangents to the curve from which  $\Delta E$  values were estimated.
- Figure 10-B:  $\ln \rho$  Vs T Characteristics for Sample # 5. 48  
 Note:  $10^{12}$  ohm-cm and  $10^{14}$  ohm-cm are Extrapolated Resistivities at 14°K and 4°K Respectively.
- Figure 10-C:  $\ln \rho$  Vs T Characteristics for Sample #17; 49  
 first heated, and then cooled.

Figure 11-A:	Top of Page: Surface of an "As Grown" Film of Thickness 740 Å; Deposited at 123 Å/sec in $5 \times 10^{-5}$ Torr. Room Temperature Resistivity was 3 ohm-cm.	50
Figure 11-B:	Bottom of Page: Diffraction Pattern for this film.	50
Figure 11-C:	Top of Page: Surface of Same Sample after a Heating/Cooling Cycle: $300^{\circ}\text{K} \rightarrow 500^{\circ}\text{K} \rightarrow 300^{\circ}\text{K}$ .	52
Figure 11-D:	Bottom of Page: Diffraction Pattern of this Thermally Cycled Sample.	52
Figure 12-A:	Top of Page: Surface of an "As Grown" Film of Thickness 600 Å Deposited as 2 Å/sec in $5 \times 10^{-5}$ Torr. Room Tem- perature Resistivity was in Excess of $10^5$ ohm-cm	53
Figure 12-B:	Bottom of Page: Diffraction Pattern of this Film.	53
Figure 12-C:	Top of Page: Surface of Same Sample After a Heating/Cooling Cycle.	54
Figure 12-D:	Bottom of Page: Diffraction Pattern of This Thermally Cycled Sample.	54
Figure 9-A:	$\ln \rho$ vs $T^{-1/4}$ Characteristics for Sample #26.	55
Figure 9-B:	$\ln \rho$ vs $T^{-1/4}$ Characteristics for Sample #30.	56

Figure 9-C:	$\ln \rho$ Vs $T^{-1/4}$ Characteristics for Sample # 7.	57
Figure 10-A:	$\ln \rho$ Vs $T^{-1/4}$ Characteristics for Sample # 5.	58
Figure 13 :	Coplanar Configuration of the Carbon Samples.	60
Figure 14 :	Circuit diagram for a Coplanar Configuration.	60
Figure 15-A:	Coplanar Configuration of Al Electrodes.	61
Figure 15-B:	Circuit Diagram for Coplanar Electrodes.	61
Figure 14' :	A Plot of Resistivity Versus Thickness. The Original 40 Data Points are not Included.	72
Figure 15 :	A Plot Of Resistivity Versus Thickness for all Samples.	73



## LIST OF TABLES

	Page
Table 1: Chemical Spectrographic Analysis of Out-gassed (1 and 2) and Stock (3 and 4) Graphite Rods, Respectively.	21
Table 2A: Aging of 600 Å Films. $R_i$ is Sample's Resistance 30 Minutes After Fabrication. $R_i$ is Sample's Resistance measured at $\Delta t_i$ Where $\Delta t_i$ is the Time Elapsed Since the Measurement of $R_i$ ( $i=2,3,4$ ).	33
Table 2B: Aging of Several Film Thicknesses. $R_i$ is Sample's Resistance 30 Minutes After Fabrication. $R_i$ is Resistance measured at $\Delta t_i$ , Where $\Delta t_i$ is the Time Elapsed Since the Measurement of $R_i$ , ( $i=2,3,4$ ).	33
Table 2C: Typical Room Temperature Resistivities for 600 Å Films. $\rho_i$ is Room Temperature Resistivity 30 Minutes After Fabrication. $\rho_i$ is Room Temperature Resistivity 2 Months After Fabrication.	34
Table 2D: Typical Room Temperature Resistivities for Several Thicknesses. $\rho_i$ is Room Temperature Resistivity 30 Minutes After Fabrication. $\rho_i$ is Room Temperature Resistivity 2 Months After Fabrication.	34
Table 3A: Typical Room Temperature Resistivity for 200 Å Films Deposited at Less Than 10 Å/sec.	35
Table 3B: Typical Room Temperature Resistivity for 150 Å Films Deposited at 11 to 20 Å/sec.	35
Table 3C: High Pressure Room Temperature Resistivity.	36
Table 4 : A Master Table for all Fabricated Samples.	74

## ACKNOWLEDGEMENTS

I thank my advisor, Professor MacVicar, for supervising my research and assisting in finalizing this thesis. I am also thankful to Professor John Vandersande for the invaluable assistance he gave in the TEM studies. I was happy to learn of Professor Vandersande's interest in thin carbon film structure and I am pleased with having worked with him.

I thank Mr. I.M. Puffer for aiding in the designing and construction of equipment used in the experiment. I am thankful to Professor J. Bostock for assisting in analyzing and interpreting the data. I am also thankful to Professor J. Bostock for assisting in proofreading the original manuscript. I thank Professor R. Mickens, Professor J. Young and Dr. S. Jackson for their moral support and encouragement. I am particularly thankful to my deceased and gifted teacher, Professor Howard Jerry Foster. Professor Foster is mainly responsible for my study at M.I.T. and is instrumental in my development as a physicist.

I thank my parents, Mrs. Louise Jones and Mr. Joseph Jones for the moral support they gave throughout my college career. I thank Mr. Mida Jones, my uncle, for financial assistance and for being concerned about my future.

## A. Theoretical Background

Although the actual band structure and transport properties of thin carbon films are not yet well known, theoretical band structures and transport mechanisms have been proposed. The most popular band model is one proposed by Mott only a few years ago.<sup>(1,2,3,4)</sup> The Mott band model is not peculiar to amorphous carbon, instead it is thought to characterize the band structures of all disordered solids. Unlike the band theory for crystals, the proposed band structure for disordered solids has no first principle mathematical derivation. The model follows entirely from several assumptions. Mott assumed that the energy eigenvalues in such materials are grouped in bands similar to the way they are in crystalline solids. Isolated systems that do not have overlapping wave-functions will have discrete energies. Discrete energies, however, transform into energy bands if the approximately  $10^{23}$  system wave-functions overlap. Such overlapping is assumed in both crystalline solids and amorphous solids.

Mott also assumed that the band edges for amorphous solids, unlike the band edges for crystalline solids, are smeared. Sharp band edges result from 3-dimensional periodicity. The positioning of ions on a 3-dimensional periodic lattice gives rise to sharp band edges in crystalline solids. Amorphous solids, do not have a 3-dimensional periodic lattice, and thus, no 3-dimensional periodic potential. The randomness in the potential of amorphous solids is the basis of Mott's assumption of smeared band edges. Smearing implies the existence of ill-defined activation energies for amorphous semiconductors, in contrast to the well-defined activation energies of crystalline semiconductors. Smeared band edges mean states exist in the energy gap at energies forbidden in crystals. States of ordinarily forbidden energies are called band "tail" states since they form the tail of the bands. For sufficiently disordered films, according to Mott, states "moving up" in energy because of the valence band edge smearing can overlap states "moving down" in energy because of the conduction band edge smearing.

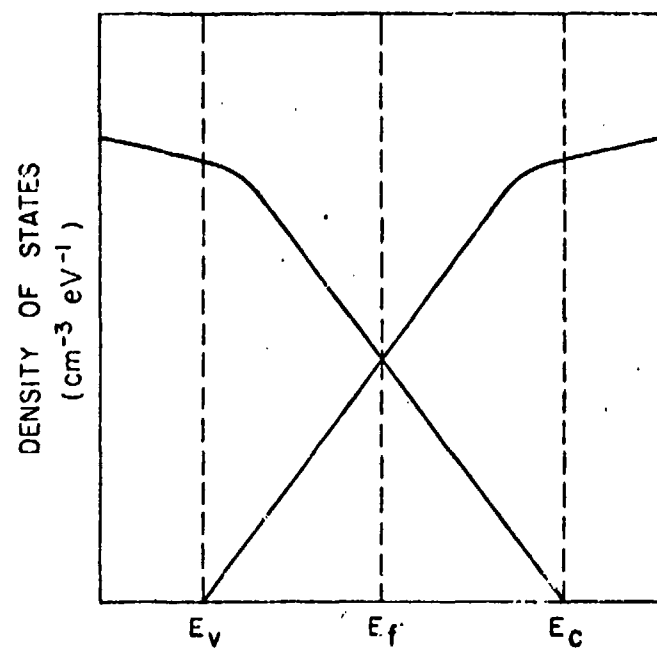
Figures 0-3A, 0-3B, 0-1A, and 0-2B, illustrate smearing for various degrees of disorder.

The tail states differ from the band states in that the tail states have localized wave-functions and vanishingly small mobilities, ie. the carriers are confined about the structural defects and respond negligibly to an applied electric field. This localization is energy dependent: states near the tip of the conduction band tail are highly localized relative to those well inside the tail; and states near the conduction band are only quasi-localized. On the other hand, crystals have energies that mark the positions of valence and conduction band edges. Disordered solids do not have band edges; however, critical energies do exist inside the valence and conduction bands and mark the positions of mobility edges. The mobility is small where the density of states is small, ie. in the tail states and is large where the density of states is large, ie. in the extended state, (refer to figures 0-1A and 0-2B). As disorder increases, the mobility gap increases.<sup>(6)</sup> Figures 0-1A shows a mobility gap width of  $E_C - E_V$  for an amorphous solid. Figure 0-2B shows a larger mobility gap width  $E_C - E_V$  for a more highly disordered solid. For sufficiently disordered solids, all states become localized states and the mobility gap reaches maximum width.

It is generally held that basic features of the band structure of disordered solids do not change during transition from crystallinity to amorphousness. (The basic features, e.g. band width and energy gap width, are a function of the short-range order.) If the short-range order of the disordered phase is the same as the long-range order of the crystalline phase, only blurring of the band edges will occur during the transition, changing only the detailed shape of the band. Deeplying localized states will be induced, but far from the band edges the band structure is only slightly perturbed. Figures 0-3A and 0-3B show the band structures of a crystal, and of a disordered solid with the same short range order as the crystal, respectively. The band structures look the same except in the energy gap region where localized

Figure 0-1A:

Density of Energy States for an Amorphous Semiconductor.



108<

Figure 0-2B:

Density of States and Mobility Gap Width for  
a Highly Disordered Semiconductor.

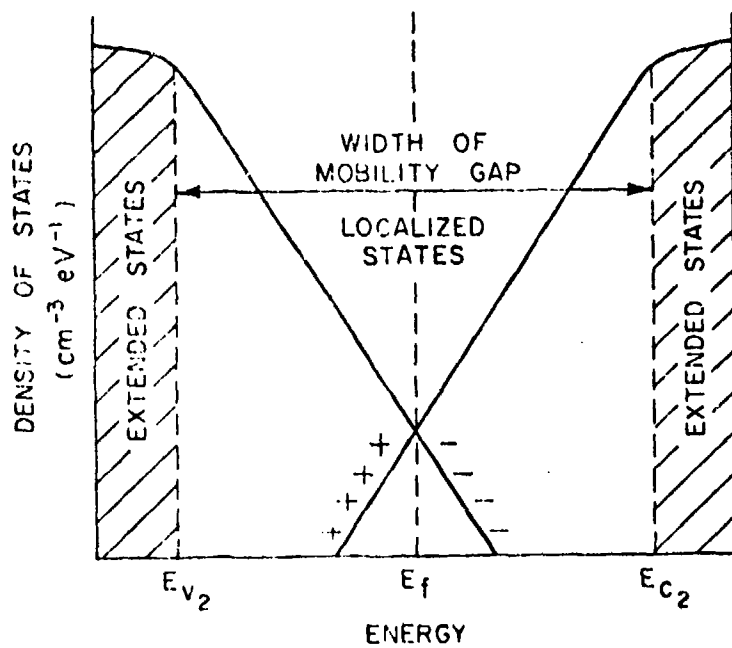
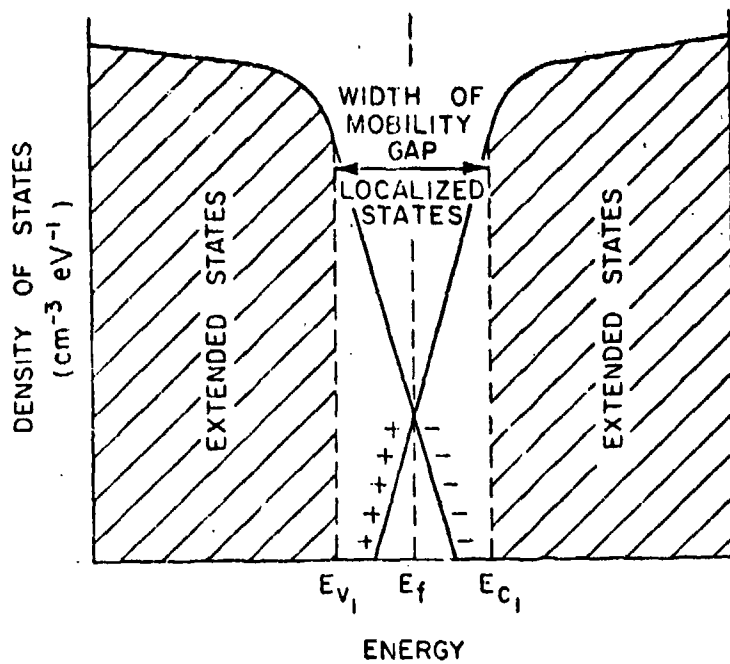
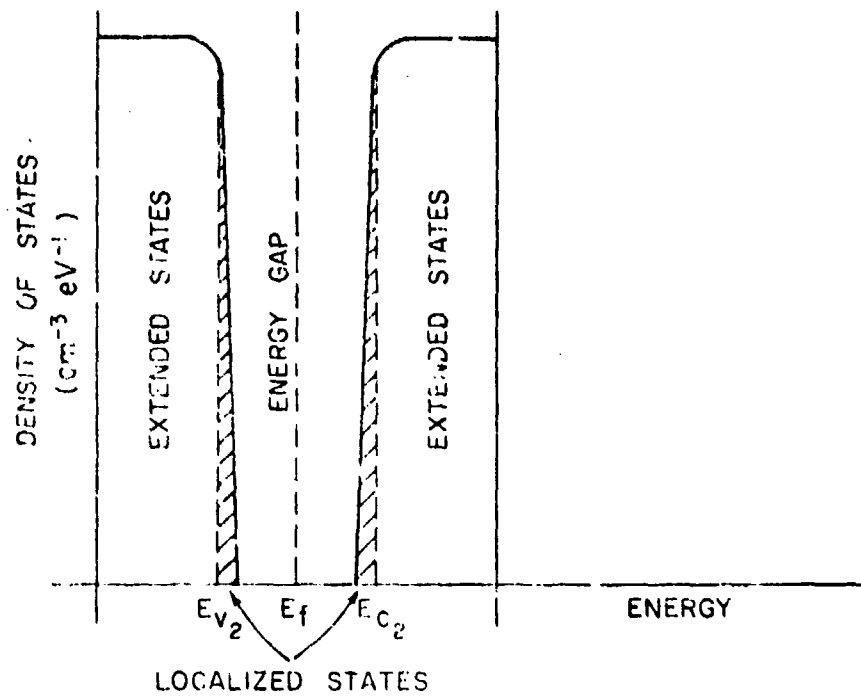
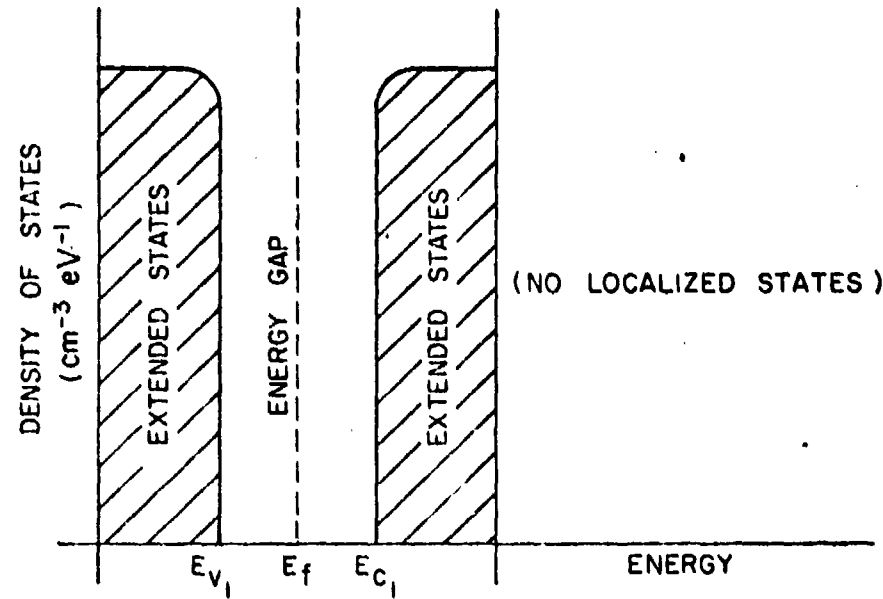




Figure 0-3A: Density of Energy States for a Semiconductor Crystal.

Figure 0-3B: Density of Energy States for a Slightly Disordered Semiconductor.



states are induced. The localized states are closer to the fermi level than the extended states, hence low temperature and low field conductivity ( $< \text{below } 10^4 \text{ V/cm}$ ), will be dominated by these localized states. For sufficiently disordered solids the localized states are dense enough for a carrier's wave function to over-lap several energy states. Hence the carriers can tunnel, or "Mott hop", from one localized state to another. Low temperature and low field ( $\sim 10^4 \text{ V/cm}$ ) hopping is a phonon-assisted conduction mechanism of the form:  $\mu = A e^{-\alpha R} e^{-\Delta E/KT}$  where  $\alpha \equiv$  a constant depending on barrier height,  $R \equiv$  hopping distance between two energy states, and  $\Delta E \equiv$  hopping energy. For nearest-neighbor hopping,  $R = a$ , the nearest neighbor hopping distance, and  $\Delta E = E_a$ . But if the electron hops to a farther neighbor,  $R = na$ , then  $\Delta E = E_a/n^3$ . And,  $\mu = A e^{-(\alpha n a + E_a/n^3 KT)}$

To maximize mobility with respect to hopping distance, one sets

$$\frac{\partial \mu}{\partial n} = 0, \text{ giving } n = \left( \frac{3 E_a}{K \alpha a} \right)^{1/4} T^{-1/4}.$$

At sufficiently high temperatures,  $n$  is of the order of unity or less, in which case hopping beyond nearest neighbors will not occur; band conduction will dominate conduction. But at sufficiently low temperature,  $n$  is large compared to unity and phonon-assisted tunneling to far atoms becomes important. For hopping beyond nearest neighbors, one gets  $\mu = A e^{-B T^{-1/4}}$  where  $B \equiv 4 (\alpha \alpha / 3)^{3/4} (E_a / K)^{1/4}$ .

$$\text{Thus, } \sigma = n e \mu \Rightarrow \ln \sigma \sim T^{1/4}$$

Similarly, the optimum hopping energy,  $\Delta E = E_a/n^3$ , is

$$\Delta E = E_a \left( \frac{\alpha a}{3 E_a} \right)^{3/4} (KT)^{3/4}.$$

If one accepts the phenomenological Mott model, one can account for many phenomena observed in carbon films as well as in other disordered semiconductors, for example, the ill-defined activation energy observed in such films, <sup>(6,7,10,11)</sup> Carriers being activated from traps to the extended states can occupy any empty quasi-localized state near the conduction band.

The model also accounts for the relatively low conductivity experimentally observed at low temperatures and low fields; <sup>(8)</sup> although conduction is dominated by the localized states, these states are small in their densities and mobilities relative to the band states.

The Mott model can explain the experimentally observed low-field ohmic conduction.<sup>(9,7)</sup> The hopping of bound carriers from one localized site to another requires an activation energy. In the limit of a high density of localized states, the activation energy tends to zero, leading to ohmic conduction.

On the negative side, the Mott model cannot account for the many deviations from linearity in  $\ln \rho$  vs  $T^{-1/4}$  experimentally observed below 10°K.<sup>(6,7,11)</sup> Linearity in the  $\ln \rho$  vs  $T^{-1/4}$  for temperatures in excess of 300°K is equally unaccounted for by the Mott model.<sup>(12)</sup> The model further does not explain the better fit to linearity in  $\ln \rho$  vs  $T^{-1/4}$  shown by annealed samples as compared to non-annealed samples.<sup>(13)</sup>

It is generally accepted that the transport properties of thin films produced by the evaporation of graphite are strongly related to the deposition parameters (deposition rate, substrate temperature, background pressure, etc.) and microstructure. Although various workers have investigated the transport properties of carbon films, a comparison of their data is difficult because of the differences in deposition parameters, cryogenic and thermal treatments. The author briefly summarizes past work below. More discussion will be presented in Chapter 4.

The electrical resistivity,  $\rho$ , of carbon films produced by the evaporation of graphite is a very difficult parameter to control. Blue and Danielson, using arc-evaporated carbon films grown at 500Å/sec. in vacuum below  $10^{-4}$  Torr, and a thickness range of 1000Å to 2300Å, succeeded only in reproducing the order of magnitude of  $\rho$  as a function of thickness.<sup>(8)</sup> They suggested that variations in structural defects prevented reproducibility in  $\rho$  as a function of thickness. However, they found that  $\rho$  as a function of temperature was reproducible if the temperature was always less than the temperature at which the film was grown, 300°K. Films that had been heated for a few minutes gave reproducible  $\rho$  as a function of temperature for temperatures in excess of 300°K provided that the film was maintained at temperatures less than the maximum temperature of the heating process.<sup>(9)</sup>

Kupperman, et al, using films of 500Å that were arc-evaporated onto a room temperature glass substrate at 50Å/sec. in a  $10^{-5}$  Torr vacuum, failed to obtain reproducible room temperature resistivities.<sup>(6)</sup> Films that were grown under identical conditions varied more than two orders of magnitude in room temperature resistivities. However, when these films were annealed at 750°C for 2 hours, they had the same resistivities. Kupperman, et al, suggested that the initial difference was obtained because of variations in the concentration of gases that were trapped during the film formation. As above, unannealed films gave reproducible  $\rho$  as a function of temperature for temperatures less than 300°K.

Morgan, using unannealed carbon films deposited by the electron beam at 2-40Å/sec. onto room temperature glass substrates, obtained

reproducible room temperature resistivities as a function of thickness.<sup>(11)</sup> Morgan outgassed his graphite rods and deposited carbon films in a  $2 \times 10^{-5}$  Torr vacuum. Room temperature resistivities increased exponentially for thicknesses less than 500 Å. Adkins et al reported large variations in room temperature resistivities. They suggested that the variations could have resulted from varying grain size and impurity content.<sup>(7)</sup> Samples were prepared by evaporation onto glass substrates from resistance-heated or electron beam heated graphite. A few angstroms per second deposited in a  $10^{-5}$  Torr vacuum was typical.

J. Kakinoki deposited carbon films onto room temperature rocksalt substrates at 50 Å/sec. - 100 Å/sec. in a  $5 \times 10^{-5}$  Torr vacuum chamber.<sup>(12)</sup> An interpretation of his data shows that room temperature resistivity becomes reproducible after many heating and cooling cycles. The difference in room temperature resistivity before and after the heating and cooling cycle was suggested to be the result of a variation in the ratio of graphite-like to diamond-like regions. After many heating and cooling cycles, the ratio stabilized and room temperature resistivities were reproducible as a function of temperature. Films that had not undergone thermal treatment had resistivities on the order of 1 ohm-cm. After many heating and cooling cycles, the room temperature resistivities dropped to  $10^{-2}$  ohm-cm.

Kupperman's thermally untreated films had resistivities varying from .02 ohm-cm to 1 ohm-cm.<sup>(6)</sup> After annealing for 2 hours at 750°C, all films had resistivities  $\sim .03$  ohm-cm.<sup>(14)</sup> Morgan's thermally untreated films had room temperature resistivities  $\sim .1$  ohm-cm, however, when heated to 450°K, the room temperature resistivities were  $10^{-2}$  ohm-cm.<sup>(6)</sup> Blue and Danielson has room temperature resistivities ranging from 1.3 to 6.6 ohm-cm. After heating and cooling through 1239°K, the room temperature resistivities dropped  $10^{-3}$  ohm-cm.

All carbon films, from the very conductive ( $10^{-2}$  ohm-cm) to the very insulative ( $\sim 10^1$  ohm-cm), seen to approach values on the order of  $10^{-2}$ - $10^{-3}$  ohm-cm when heat treated to temperatures 700°K - 200°K. These films may be becoming more graphite-like and approaching  $10^{-3}$  ohm-cm, which is the value of fine-particle carbon blacks.<sup>(8)</sup> Conduction perpendicular to the c-axis of graphite shows a room temperature resistivity of 2.5 ohm-cm.<sup>(8)</sup> This suggests that many of the films are randomly oriented collections of graphite grains with conduction taking place perpendicular

to the c-axis, since c-axis conduction of graphite is  $10^{-4}$  ohm-cm. The ratio of high conduction oriented grains to low conduction oriented grains must increase with heat treated samples. Alternatively, it could mean that the high conduction oriented grains grow faster and larger than the low conduction oriented grains when thermally treated. Some investigators, however, suggest that the increased conductivity upon thermal treatment might be related to outgassing the samples rather than changing the structure of the samples. Heat treating the samples, they suggest, drives gasses from the samples leaving broken bonds behind which will increase the density of acceptor states. Greorhie and Kupperman classified their films as p-type.<sup>(10,6)</sup>

Adkins et al. noticed large variations in room temperature resistivity vs. thickness when they carried out their experiment under vacuum.<sup>(9)</sup> For thicknesses from  $0\text{\AA} - 2500\text{\AA}$ ,  $\rho$  varied from  $\sim .1$  ohm-cm for his thickest films to values  $\sim 10^2$  ohm-cm for the thinnest films. The resistivity was independent of thickness for thicknesses in excess of  $500\text{\AA}$ . For values less than  $500\text{\AA}$ ,  $\rho$  increased exponentially as the thickness decreased. Adkins suggested that the large resistivity resulted from the carriers inability to hop the optimum hopping distance of  $50\text{\AA}$ . Very large resistivities were observed for thicknesses much less than the optimum hopping distance ( $\sim 70$  ohm-cm). For thicknesses much greater than the optimum hopping distance ( $\sim 500\text{\AA}$ ), the resistivity was independent of thickness. Blue and Danielson also saw very large resistivities for very thin films. They suggested that the large resistivity resulted from discontinuities in the films.<sup>(8)</sup>

Boiko et al reported their carbon films resembled highly disordered graphite.<sup>(13)</sup> Blue and Danielson reported their films to have less long range order and therefore to be more truly amorphous than any other form of carbon.<sup>(8)</sup> Kakinoki observed ordered domains less than  $10\text{\AA}$  in size. These domains were randomly distributed and randomly oriented graphite-like and diamond-like regions. They existed in the ration of 1.1:1 (diamond:graphite).<sup>(12)</sup>

Morgan, Adkins and Kupperman observed the relation  $\ln \rho$  vs.  $T^{-1/4}$  for unannealed films in the respective temperature ranges:  $5^{\circ}\text{K} - 8^{\circ}\text{K}$ ,  $10^{\circ}\text{K} - 25^{\circ}\text{K}$ ,  $40^{\circ}\text{K} - 20^{\circ}\text{K}$ .<sup>(6,7,11)</sup> Kupperman also noticed the  $\ln \rho$  vs.  $T^{-1/4}$  relation for films that had been annealed for 2 hours at  $200^{\circ}\text{C}$ .<sup>(6)</sup> As with his unannealed films, the observation was made from  $4^{\circ}\text{K} - 20^{\circ}\text{K}$ . Gheorghiu observed the  $\ln \rho$  vs.  $T^{-1/4}$  relation for films annealed at temperatures  $\sim 725^{\circ}\text{K}$ .<sup>(10)</sup> This observation was in the range  $77^{\circ}\text{K} - 300^{\circ}\text{K}$ . An analysis of the data taken from the annealed samples of Toyoda et al. and McLintock et al.,<sup>(14)</sup> shows Mott hopping above  $77^{\circ}\text{K}$ . Blue and Danielson did not observe Mott hopping in the temperature range  $77 - 1200^{\circ}\text{K}$ .<sup>(8)</sup> Films that had not been thermally treated were well fitted by  $R = AT^{-5}$  from  $77 - 300^{\circ}\text{K}$ . Successive heating and cooling caused the exponent to decrease. After a dozen cycles the curve fitted  $R = \alpha - \beta T$ ;  $\alpha$  and  $\beta$  are constants.

Morgan, Adkins and Kupperman's observations of Mott hopping in the low temperature range for their unannealed samples were in good agreement with Mott's prediction. Debenyl et al. reported a change in structure of amorphous carbon films mainly between  $500 - 700^{\circ}\text{K}$ .<sup>(15)</sup> They suggested that these temperatures resulted in a transformation to a more ordered, polycrystalline type of state with ordering up to  $1575^{\circ}\text{K}$ .

According to Debenyl, Kupperman's films which were annealed at  $473^{\circ}\text{K}$  had not undergone significant ordering. Debenyl suggested this basis for having observed Mott hopping in the temperature range predicted by Mott for a disordered solid. Investigators whose films had undergone significant ordering according to Debenyl either did not observe hopping or observed hopping only in the high temperature region.



### C. The Current Work

Considerable theoretical as well as industrial effort has developed in amorphous semiconductors because of their promise as device materials. Amorphous carbon is of particular interest to our laboratory because of its potential as a quantum mechanical tunneling barrier.

The author first sought to correlate the work of previous investigators. These investigations were carried out with different experimental procedure and different fabrication parameters; thus a comparison of previous data is difficult. The author's study seeks to eliminate the confusion between these sets of data. His major emphasis is the sensitivity of resistivity to fabrication parameters and microstructure. The temperature dependence of resistivity is of particular interest. The intent is always to be able to compare the results of this one investigation to that of previous investigators, and to look for consistency between the experiments.

## CHAPTER 2: MATERIALS AND EQUIPMENT

## A. Starting Material

Thin carbon films were fabricated by the evaporation of 1/4" diameter graphite rods. The purity of the rods was confirmed by a chemical spectrographic analysis and a residual gas analysis. To obtain the chemical spectrographic analysis, two graphite rods were used. The first rod had been used previously in the fabrication of carbon films and the second rod was taken from stock. The first rod was cut into two parts and labelled Sample 1 and Sample 2. The second rod was also broken into two parts and labelled as Sample 3 and Sample 4. Table 1 shows the results of that analysis.

A standard diffusion pump system was used for evaporation of the carbon by sublimation from a laboratory-built carbon gun. Figure 1 shows the mass spectrum of the background gases of the system at  $4 \times 10^{-6}$  Torr while the carbon rods were still cold. Figure 2 shows the mass spectrum of the background gases at  $1 \times 10^{-5}$  Torr in the system following out-gassing of the rods by current heating them to red-hot, but not to evaporation temperature. After this analysis, the rods were heated to just below evaporation, which corresponded to a pressure of approximately  $5 \times 10^{-5}$  Torr. The pressure was then lowered back to  $4 \times 10^{-6}$  Torr and the gases were analyzed. Both of the out-gassed profiles are represented in Figure 2. Figure 1 and figure 2 have peaks at the same mass numbers, therefore the rods do not add new contaminants to the system. Some peaks in the out-gassed profile, however are enhanced.

## B. Carbon Gun And Vacuum System

In the ambient, graphite evaporates at  $3600^{\circ}\text{C}$ . Although the graphite evaporation temperature would be expected to be lowered by lowering the pressure, a material well behaved at high temperatures is still needed in the construction of a graphite evaporation gun. The gun used in the fabrication of samples was constructed from stainless steel.

Table I: Chemical Spectrographic Analysis of Out-gassed (1 and 2) and Stock (3 and 4) Graphite Rods, Respectively.

SAMPLE

1

2

3

4

Al

 $10^3\%-10^{-1}\%$ 

Ca

 $10^{-4}\%-10^{-3}\%$  $10^{-4}\%-10^{-3}\%$  $10^{-4}\%-10^{-3}\%$  $10^{-4}\%-10^{-3}\%$ 

Cu

 $<10^{-4}\%$  $<10^{-4}\%$  $<10^{-4}\%$  $<10^{-4}\%$ 

Fe

 $10^{-4}\%-10^{-3}\%$  $10^{-4}\%-10^{-3}\%$  $10^{-4}\%-10^{-3}\%$  $10^{-4}\%-10^{-3}\%$ 

Mg

 $10^{-4}\%-10^{-3}\%$  $<10^{-4}\%$  $<10^{-4}\%$  $10^{-4}\%-10^{-3}\%$ 

Si

 $10^{-4}\%-10^{-2}\%$  $10^{-4}\%-10^{-3}\%$  $10^{-4}\%-10^{-3}\%$  $10^{-4}\%-10^{-3}\%$ 

Ti

 $10^{-4}\%-10^{-3}\%$  $10^{-4}\%-10^{-3}\%$  $10^{-4}\%-10^{-3}\%$  $10^{-4}\%-10^{-3}\%$ 

V

 $<10^{-3}\%$  $<10^{-3}\%$  $<10^{-3}\%$  $<10^{-3}\%$

122<

Figure I: Mass Spectrum of  $4 \times 10^{-6}$  Torr Vacuum Chamber Before  
Out-Gassing the Graphite Rods.

123<

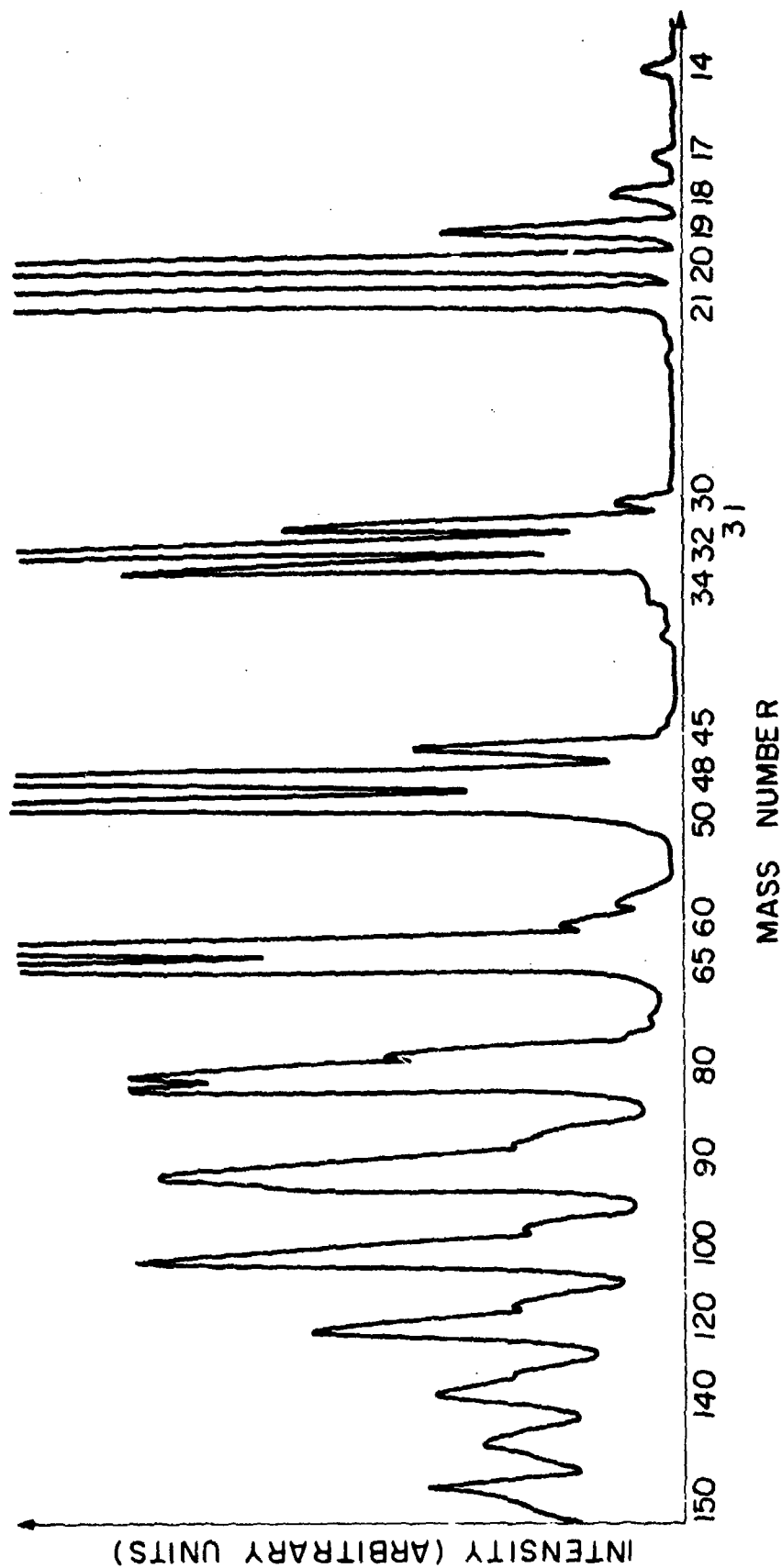
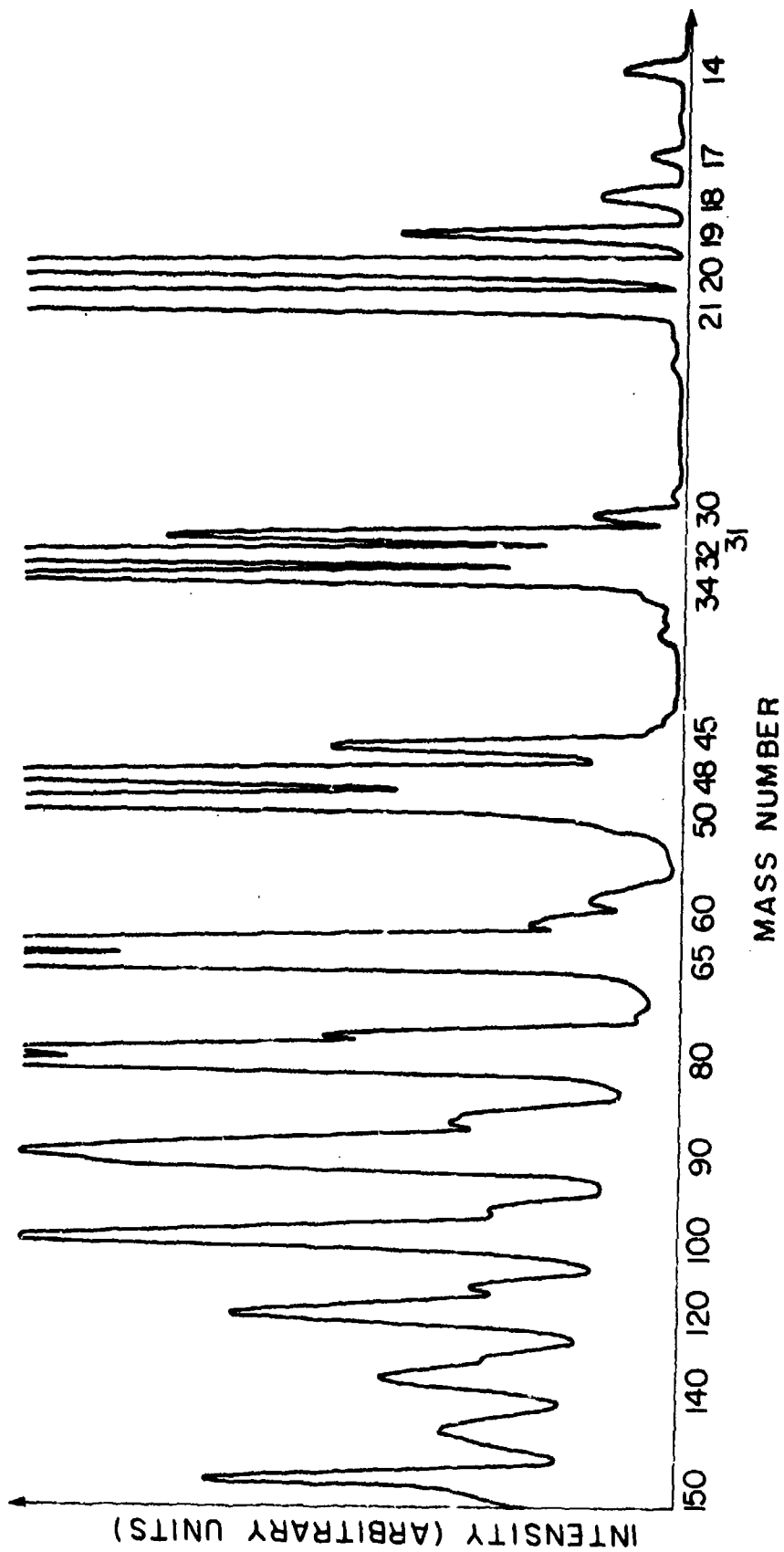


Figure 2: Mass Spectrum of  $1 \times 10^{-5}$  Torr Vacuum Chamber After Out-Gassing the Graphite Rods.

125<





Heavy, conductive electrodes needed to carry the desired current were provided by 1/4" Cu rods on the gun. An external A.C. variable bias was applied through electrical vacuum feed-throughs. The applied voltage spanned 0 to 10 volts. Figure 3 shows the gun mounted on a portable platform which can be moved into and out of the vacuum chamber with ease.

A second A.C. power source powered a W-filament which was used for the evaporation of A<sub>2</sub> electrodes. The W-filament was also mounted on the platform about 1" from the carbon gun. A pyrex "chimney" was used to enclose the evaporation apparatus. This glass cylinder served both to protect the bell jar and to support the substrate holder.

The substrate holder itself was designed and equipped with mechanical feed-throughs so the sample could be completely fabricated in situ. Figure 4 shows the substrate holder mounted on the pyrex cylinder. Both masks can be moved by mechanical feed-throughs. The motion of the mask is confined by mechanical guides located between the slides and a shutter which is also operated by a mechanical feed-through. The vacuum chamber is pumped by a diffusion pump system. Pressures above 1 micron were monitored by a thermocouple gauge; below one micron, the pressure was monitored by an ionization gauge.

### C. The Sample

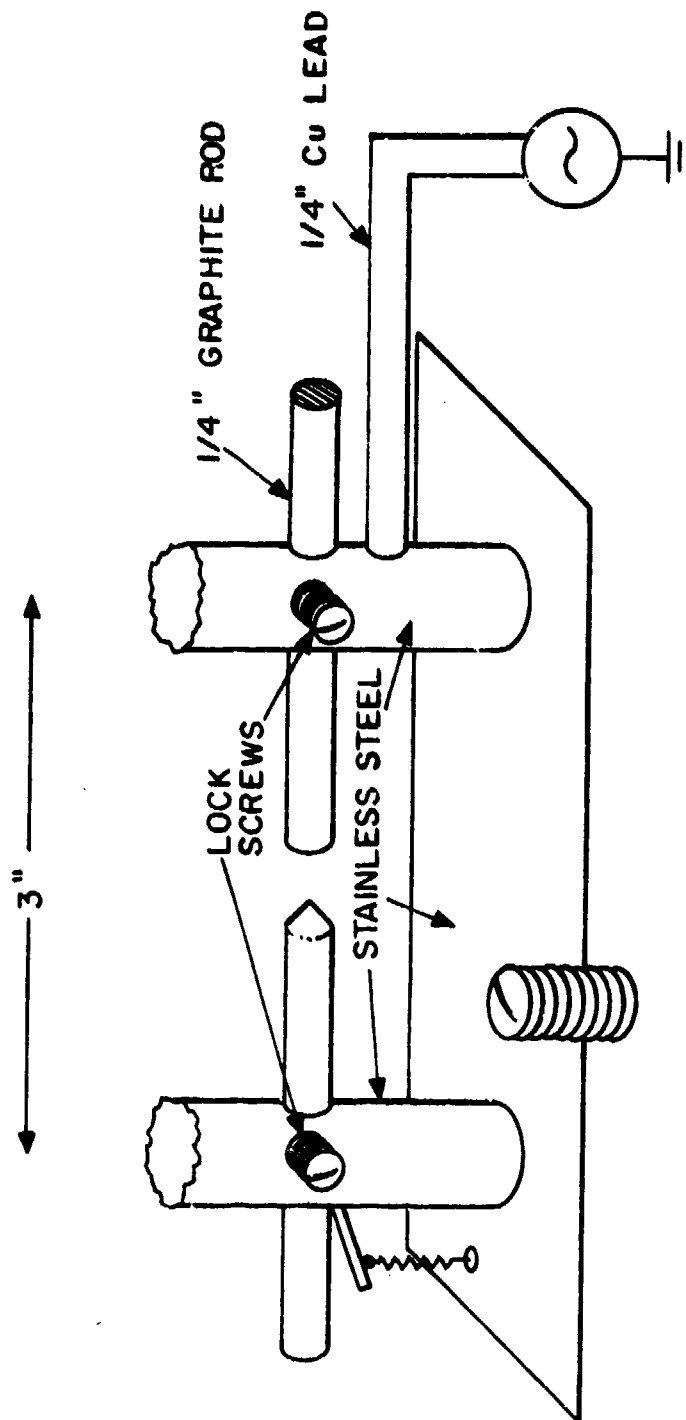
High resistivity substrates must be used to prevent current leakage during measurements of the carbon films. The substrate material used in this experiment was Fisherbrand Procleaned Microscope Slides; a product of the Fisher Scientific Co. The resistance of the slide was measured to be on the order of  $10^{16}$  ohms at  $T=300^{\circ}\text{K}$  by an electrometer whose measuring ability was  $10^{16}$  ohms.

Five mil gold wire was used as leads. Pressed indium served to electrically and mechanically fasten the gold leads to the contacts. The usage of silver paint was abandoned as a contact fastener. In addition

127<

Figure 3:

Carbon Evaporation Gun.

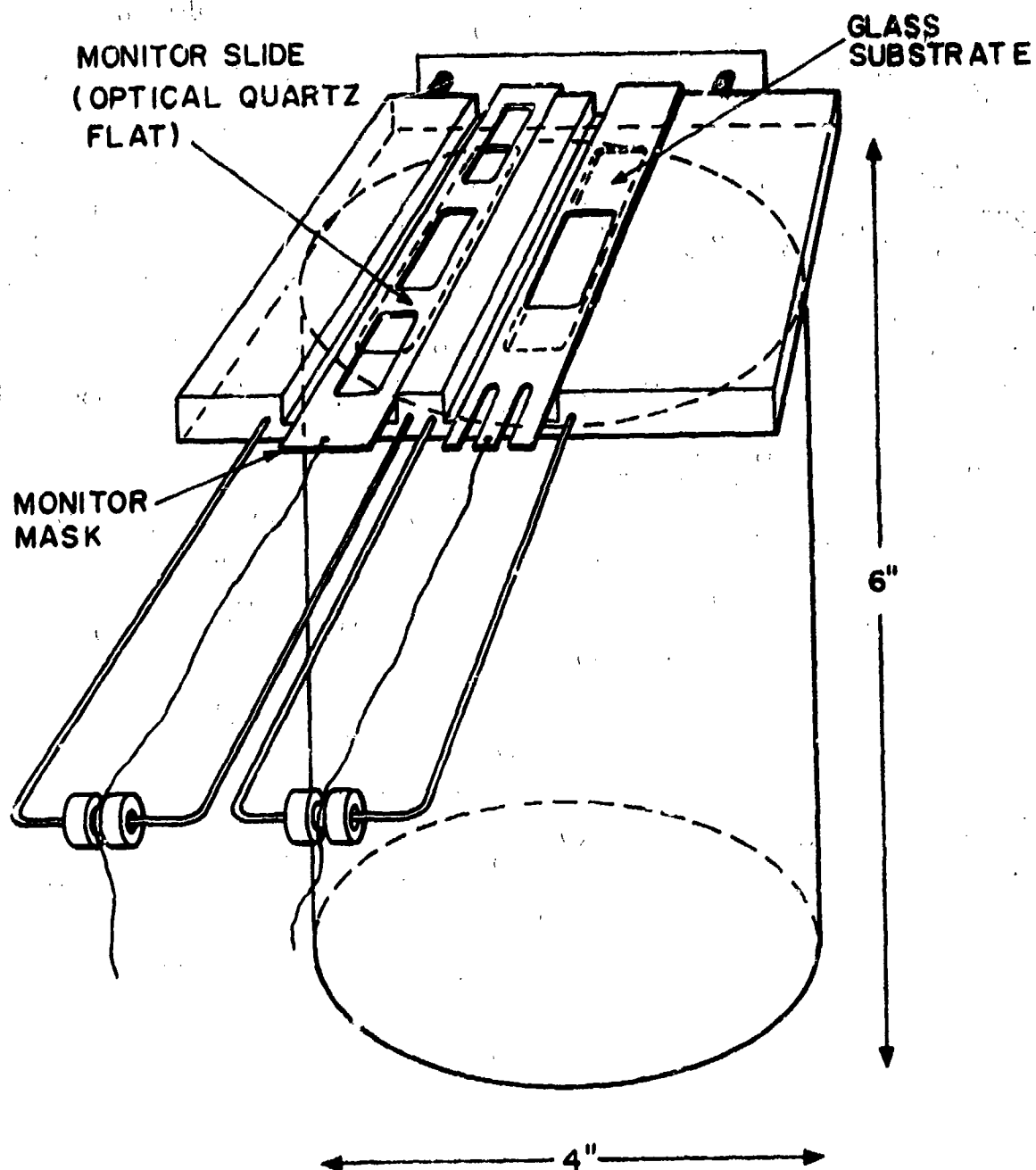


STAINLESS STEEL CARBON EVAPORATION GUN

Figure 4: Substrate Holder and Slide Masks Mounted on the Pyrex Chimney. The monitor and substrate masks can be pulled along mechanical guides underneath the stationary optical quartz flat and the glass substrate.

130<

26



to requiring at least forty minutes to try, it rendered poor mechanical stability. The pressed indium, on the other hand, gave excellent electrical as well as mechanical contact. Moreover, such contacts could be accomplished quickly.

Film thicknesses were measured after fabrication on an M-100 Angstrometer whose resolution was 50 angstroms. Optical flats were used as the thickness monitoring slides; microscope slides could not be used for this purpose. Being too thin for mechanical stability, they bend under applied pressure, and distort the optical fringe field. Optical flats are sufficiently thick to not bend under mechanical pressure, and the fringe field remains intact.

#### D. The Measurement System: Low Temperature

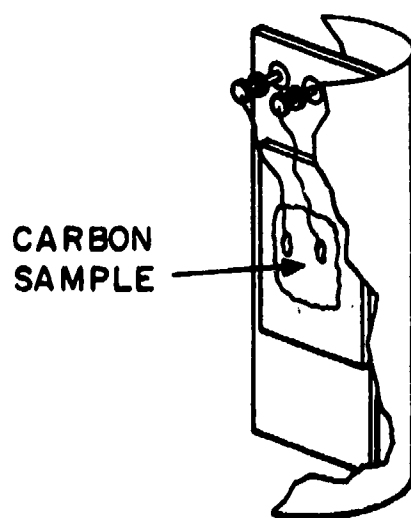
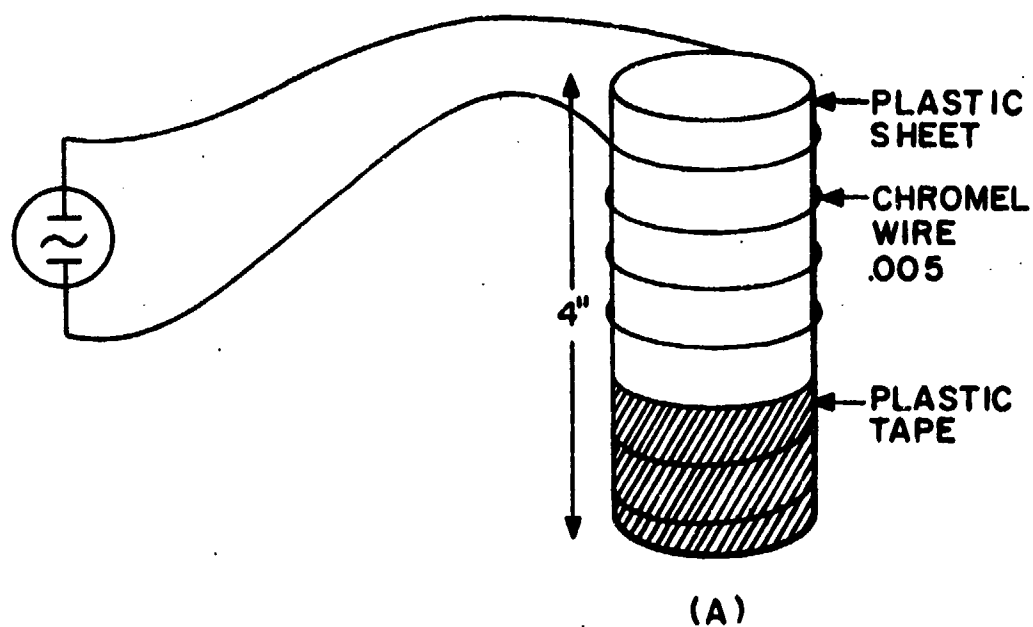
A standard cryostat was used. To heat the sample above the helium bath temperature, a heater was constructed comprised of a sheet of plastic rolled into a right circular cylinder. Plastic tape placed along the lateral seam secured the fixture. Five mil chromel wire was wrapped around the cylinder in a spiral-like configuration. Plastic tape then covered the wire leaving only the ends exposed. Leads connected the chromel wire to a variable D.C. voltage source, 0 to 40 volts. See Figure 5. To measure the temperature, two 4-pt. probe Ge thermometers were used. The first thermometer was accurate in the  $4^{\circ}\text{K}$  to  $30^{\circ}\text{K}$  interval. The second was accurate in the  $15^{\circ}\text{K}$  to  $100^{\circ}\text{K}$  interval. Separate constant current supplies were used for the two thermometers at 10 ma and 0.1 ma, respectively.

To minimize temperature fluctuations and temperature gradients in the vicinity of the sample, He gas was used for heat exchange. A three foot long pyrex tube, fused at one end, and fitted with an air-tight header on the other end, was used as a sample chamber. The header was equipped with electrical feed-throughs and an inlet valve for roughing down and for back-filling with He. gas. See Figure 6.

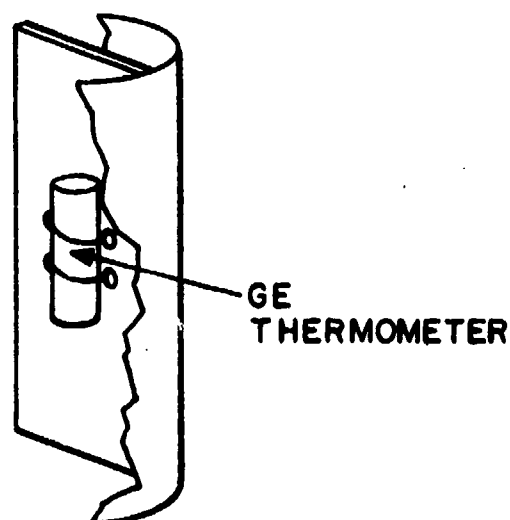
**Figure 5:**

- A: Heater for Heating Carbon Sample.
- B: Carbon Sample Mounted in the Heater.
- C: Ge Thermometer Mounted in Heater, on the back of the Sample.

133&lt;



(B)



(C)



Figure 6: Sample Chamber and Cryostat.

1.35&lt;

CONSTANT CURRENT  
SUPPLY FOR Ge  
THERMOMETER

SAMPLE LEADS

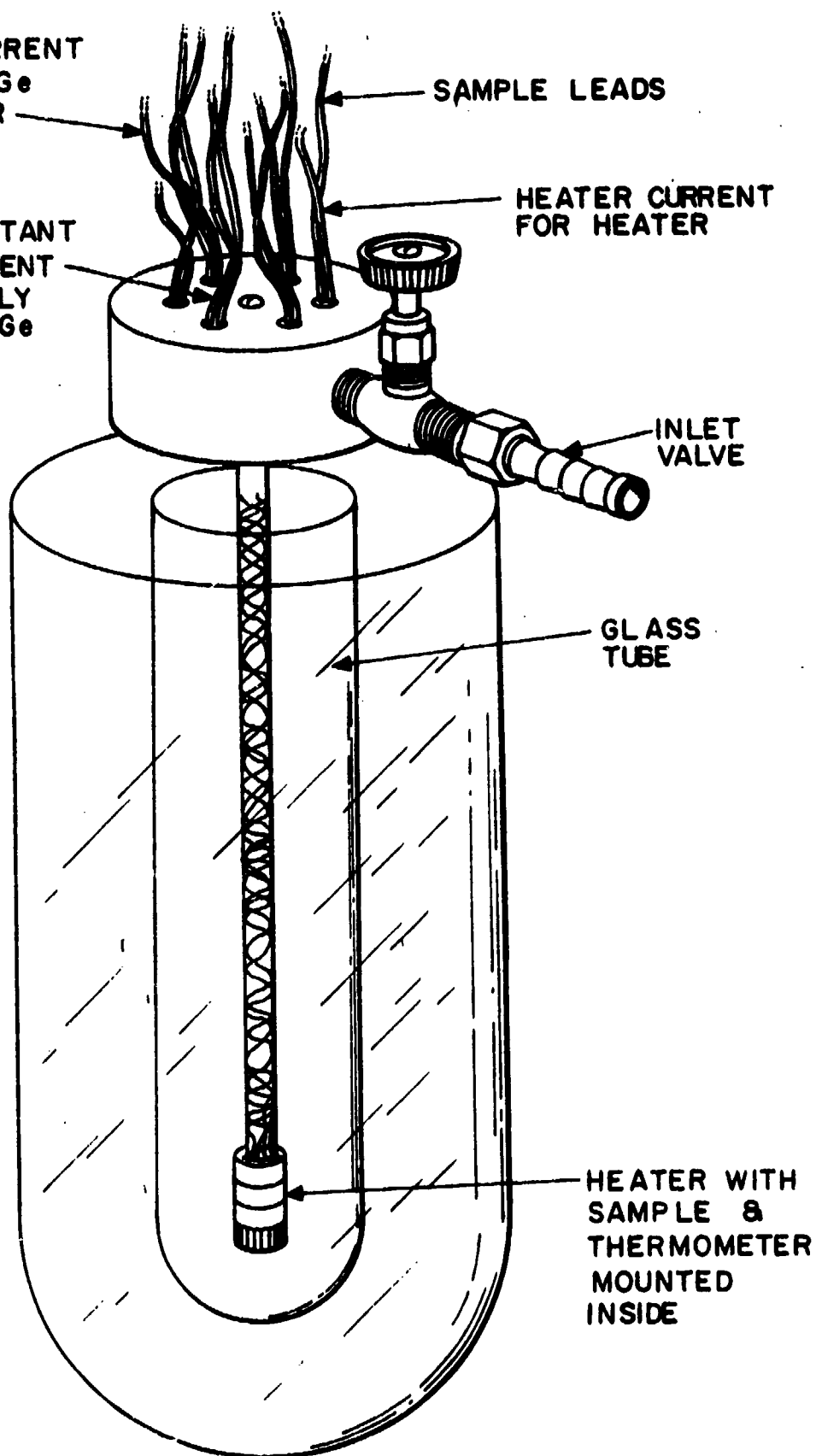
CONSTANT  
CURRENT  
SUPPLY  
FOR Ge

HEATER CURRENT  
FOR HEATER

INLET  
VALVE

GLASS  
TUBE

HEATER WITH  
SAMPLE &  
THERMOMETER  
MOUNTED  
INSIDE

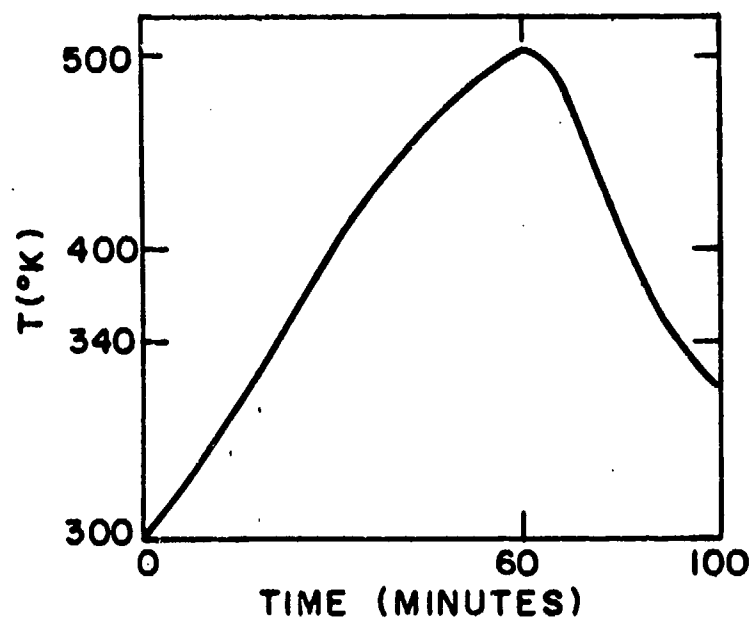


#### E. The Measurement System: High Temperature

The Type 1500 furnace with a 1200°C capacity was used to heat the samples. The temperature Vs. time characteristics for the furnace is shown in figure 7. The furnace's thermometer yielded temperature values within 2°C of a Hg thermometer placed in the over.\*

\* The furnace is a product of the Thermolyne Corporation.

Figure 7 : Temperature Versus Time Characteristics for the Thermal Cycle of Samples.



## CHAPTER 3: EXPERIMENTAL RESULTS

A Master Data Table is Presented in Appendix A.

A. Resistivity and Aging Versus Fabrication:

Many of the films displayed aging effects. Typical behaviors of film resistances with time are shown in tables 2-A and 2-B. These show resistance increases as well as resistance decreases and instances of no change in the resistance. Table 2-A shows aging for films of approximately  $700^{\circ}\text{A}$ . Table 2-B shows aging for films of several thicknesses and deposition rates. Aging effects are observed in extended time durations also. Table 2-C shows long term aging effects for films approximately  $600^{\circ}\text{A}$  in thickness; table 2-D shows long term aging effects for several thicknesses and deposition rates. There seems to be no apparent relation between aging, film thickness and deposition rate.

Tables 2-C and 2-D show typical room temperature resistivities for the entire thickness spectrum. By decreasing the evaporation rate to less than  $10^{\circ}\text{A}/\text{sec}$  while maintaining the other fabrication parameters of pressure and thickness range as in tables 2-C and 2-D, the resistivity can be enhanced by several orders of magnitude. Table 3-A shows typical room temperature resistivity values for films approximately  $200^{\circ}\text{A}$  thick evaporated at less than  $10^{\circ}\text{A}/\text{sec}$ . Table 3-B shows that resistivity values for films of approximately the same thickness are similar to those in tables 2-C and 2-D when deposition rates are in excess of  $10^{\circ}\text{A}/\text{sec}$  are used. It is concluded from tables 2-C, 2-D, 3-A and 3-B that resistivity of films  $200^{\circ}\text{A}$  to  $1600^{\circ}\text{A}$  is independent of the deposition rate for rates in excess of  $10^{\circ}\text{A}/\text{sec}$ , but increases by several orders of magnitude for slower deposition rates.

Table 3-C shows that resistivity can also be enhanced by increasing the pressure while maintaining the ranges of thickness and deposition rate as in tables 2-C and 2-D.

$R_1$ : Sample's Resistance 30 Minutes After Fabrication.

$R_i$ : Samples' Resistance measured at  $\Delta t$ , Where  $\Delta t$  is the Time Elapsed Since the Measurement of  $R_1$ , ( $i=2,3,4$ ).

Table 2A: Aging of 600<sup>o</sup>A Films.

Table 2B: Aging of Several Film Thicknesses.

S#	THICKNESS(Å)	DEPOSITION		R <sub>1</sub>	Δt <sub>2</sub>	R <sub>2</sub>	Δt <sub>3</sub>	R <sub>3</sub>	Δt <sub>4</sub>	R <sub>4</sub>
		RATE (Å/sec)								
56	690	115		45.7 KΩ	26hr	52.6 KΩ	36 hr	69 KΩ		
58	704	118		.163 MΩ	40m:n	.163 MΩ	23 hr	.165 m:n.		
54	710	60		96.7 KΩ	21hr	96 KΩ				
44	644	107		139 KΩ	1 hr	141 KΩ	44 hr	151 KΩ	97hr	155 KΩ
40	735	81		670 KΩ	24hr	1120 KΩ	96 hr	1330 KΩ	126hr	1500 KΩ

TABLE 2-A

48	100	33		.48 MΩ	24 hr	.467 MΩ	48 hr	.467 MΩ	72 hr	.456 MΩ
45	490	81		103 KΩ	1.5 hr	100 KΩ	2.5 hr	95 KΩ	22 hr	93 KΩ
46	818	136		54 KΩ	20 hr	51 KΩ	44 hr	54.4 KΩ	70 hr	54.4 KΩ
42	218	36		417 KΩ	24 hr	740 KΩ	96 hr	1140 KΩ	117 hr	1170 KΩ
57	1050	58		.764 MΩ	7 min.	.652 MΩ	18 min.	.724 MΩ	64 min.	.869 MΩ

TABLE 2-B

1.41^



22:

Room Temperature Resistivity 30 Minutes After Fabrication.  
Room Temperature Resistivity 2 Months After Fabrication.

Table 2C:

Typical Room Temperature Resistivities for  
600<sup>0</sup>A Films.

Table 2D:

Typical Room Temperature Resistivities for Several  
Thicknesses.

SAMPLE #	THICKNESS (°A)	DEPOSITION RATE (°A/sec)	$\rho_1$ (ohm-cm)	$\rho_2$ (ohm-cm)
25	603	121	.14	.13
12	570	57	1.22	1.1
26	693	46	.24	.22
44	644	107	2.39	2.4

Table 2-C

9	786	96	30.7	34.6
13	412	70	2.4	2.0
18	412	40	.25	.22
20	896	75	.33	.30
22	167	42	.40	.33
33	100	20	.45	.52
19	1695	65	.25	.23

Table 2-D

Table 3A: Typical Room Temperature Resistivity for  
200°A Films Deposited at less than 10°A/Sec.

Table 3B: Typical Room Temperature Resistivity for  
150°A Films Deposited at 11 to 20°A/Sec.

SAMPLE #	THICKNESS (°A)	DEPOSITION RATE (°A/sec)	$\rho$ (ohm-cm)
61	245	4	$8 \times 10^7$
62	250	7	7.5
	260	6	$5 \times 10^3$
17	210	5°	67

Table 3-A

33	100	20	.46
47	184	20	1.26
15	130	13	1.2
52	100	11	.29

Table 3-B

Table 3-C: High Pressure Room Temperature Resistivity

SAMPLE #	THICKNESS (°A)	DEPOSITION RATE (°A/sec)	$\rho$ (g./cm. <sup>3</sup> )	PRESSURE (Torr)
65	740	123	17	$5 \times 10^{-4}$
66	350	58	16.4	$5 \times 10^{-4}$
67	490	98	6.2	$5 \times 10^{-4}$
68	980	163	26.5	$5 \times 10^{-3}$
69	980	175	69	$5 \times 10^{-3}$
70	740	74	74	$5 \times 10^{-3}$
71	700	80	70	$5 \times 10^{-3}$

Table 3-C

## B. Resistivity as a Function of Temperature:

### Hysteresis:

All samples showed a temperature dependence over the observed temperature range. For approximately one ohm-cm samples  $4^{\circ}\text{K}$  to  $500^{\circ}\text{K}$  was the observed temperature range. Such samples were ordinarily made at deposition rates in excess of  $10^{\circ}\text{A}/\text{sec}$ , thicknesses in excess of  $100^{\circ}\text{A}$  and residual pressures approximately  $5 \times 10^{-5} \text{ Torr}$ . These examples showed a very strong temperature dependence for temperature less than  $77^{\circ}\text{K}$ . Figures 8-A and 8-B show typical resistivity versus temperature characteristics.

The hysteresis observed in these figures is typical of all samples and is independent of fabrication parameters. The room temperature resistivity invariably drops approximately one order of magnitude during the  $300^{\circ}\text{K} \rightarrow 500^{\circ}\text{K} \rightarrow 300^{\circ}\text{K}$  heating and cooling cycle. Additional cycles will also yield hysteresis loops but no additional changes in room temperature resistivities will occur. Figure 8-C shows typical hysteresis loops resulting from heating and cooling cycles. The first cycle shows a large hysteresis effect and a drop in room temperature resistivity by more than an order of magnitude. The second cycle shows a loop that closes on itself. The third and fourth cycles show loops of smaller area than the first two and are superimposed.

### Functional Dependence:

In general the  $\ln \rho$  vs.  $T^{-1}$  exhibited a non-linear characteristic. However, samples whose room temperature resistivities were on the order of  $10^{-1}$  ohm-cm exhibited extensive low temperature intervals where the behavior was approximated linearity. Using the relation  $\ln \rho = \exp^{-\frac{\Delta E}{kT}}$  where  $\Delta E$  is an effective activation energy,  $\Delta E$  was extracted from the  $\ln \rho$  vs  $T^{-1}$  characteristics. By plotting a tangent to the curve in figure 9-B for sample #30 a room temperature activation energy of  $\sim 69$  meV was noted; similarly, 15.3 meV was noted at  $77^{\circ}\text{K}$ . An

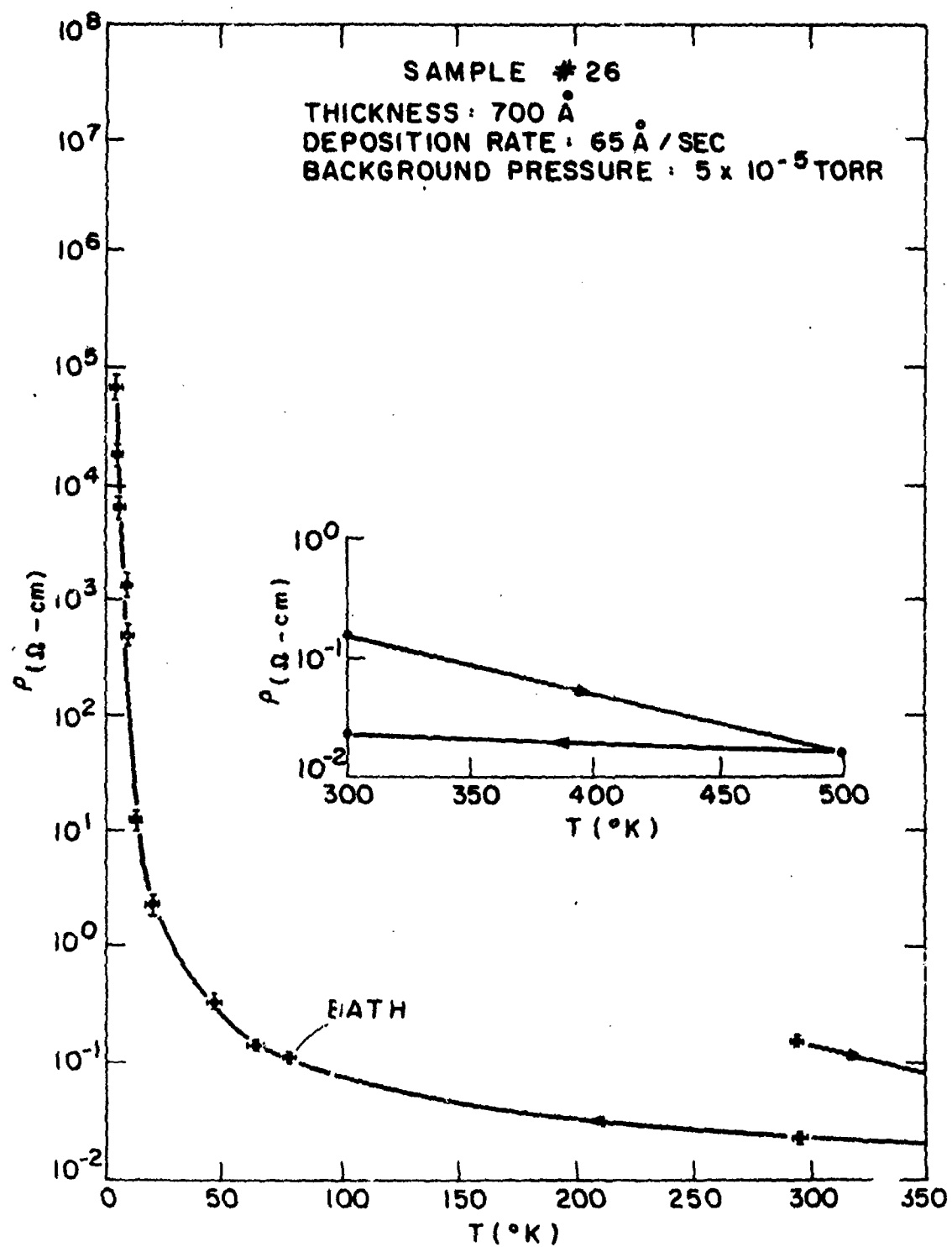
$\rho(T)$  Characteristics for Initial Heating and Subsequent Cooling.

Figure 8-A: Sample #26.

Figure 8-B: Sample #30.



150&lt;



151&lt;

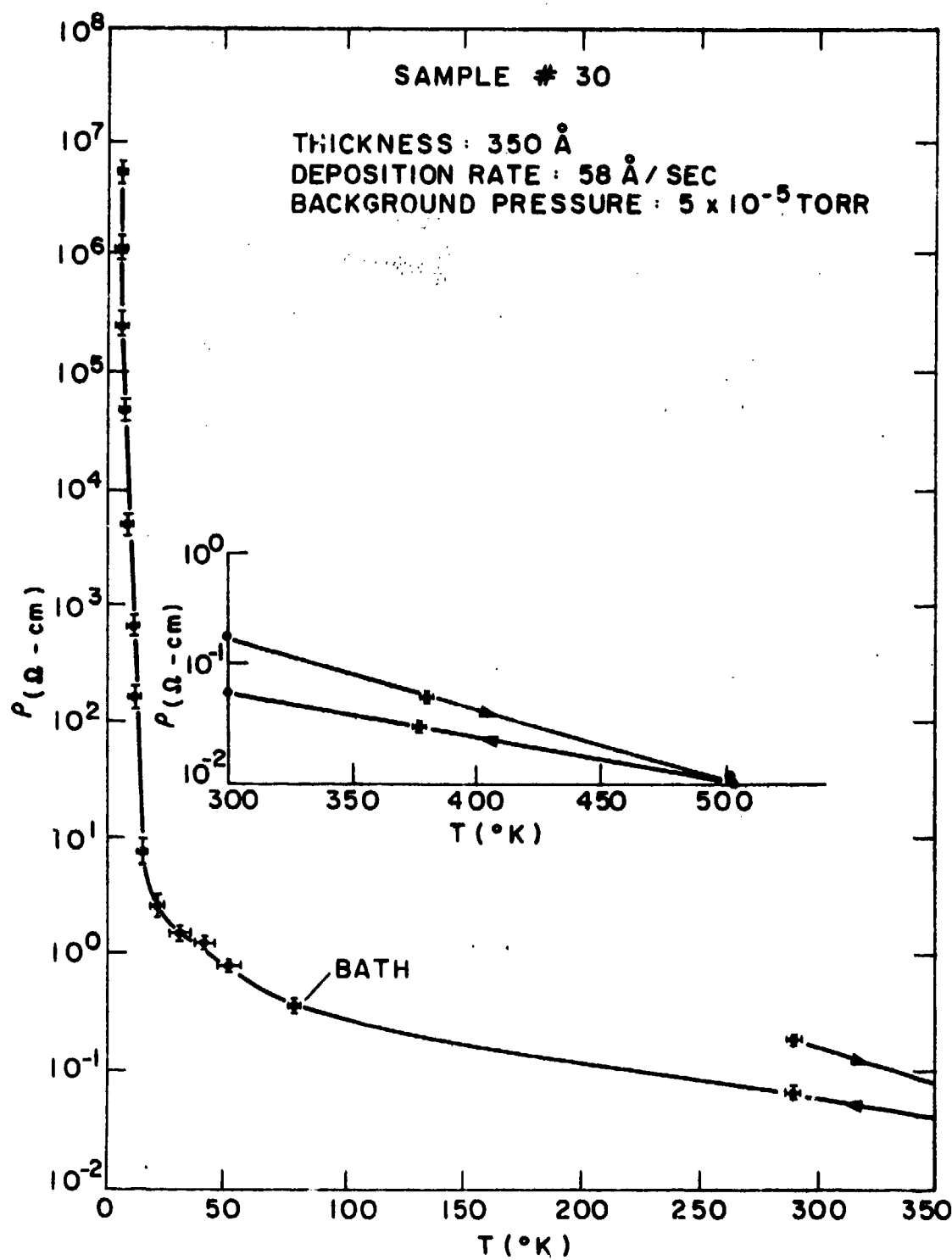


Figure 8-C:

$\ln p$  Vs T Characteristics for the First Four  
Heating and Cooling Cycles of Sample #4.

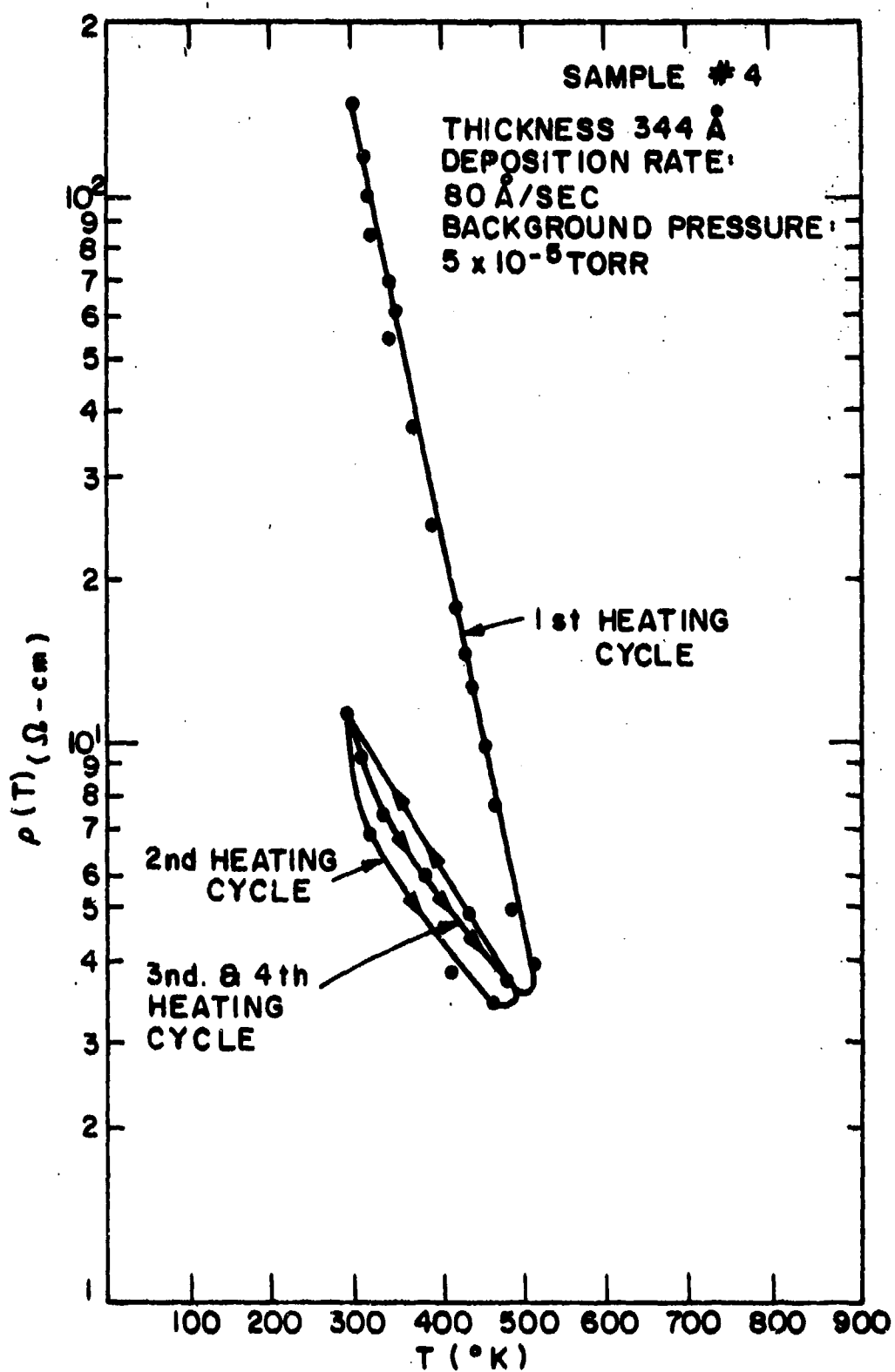
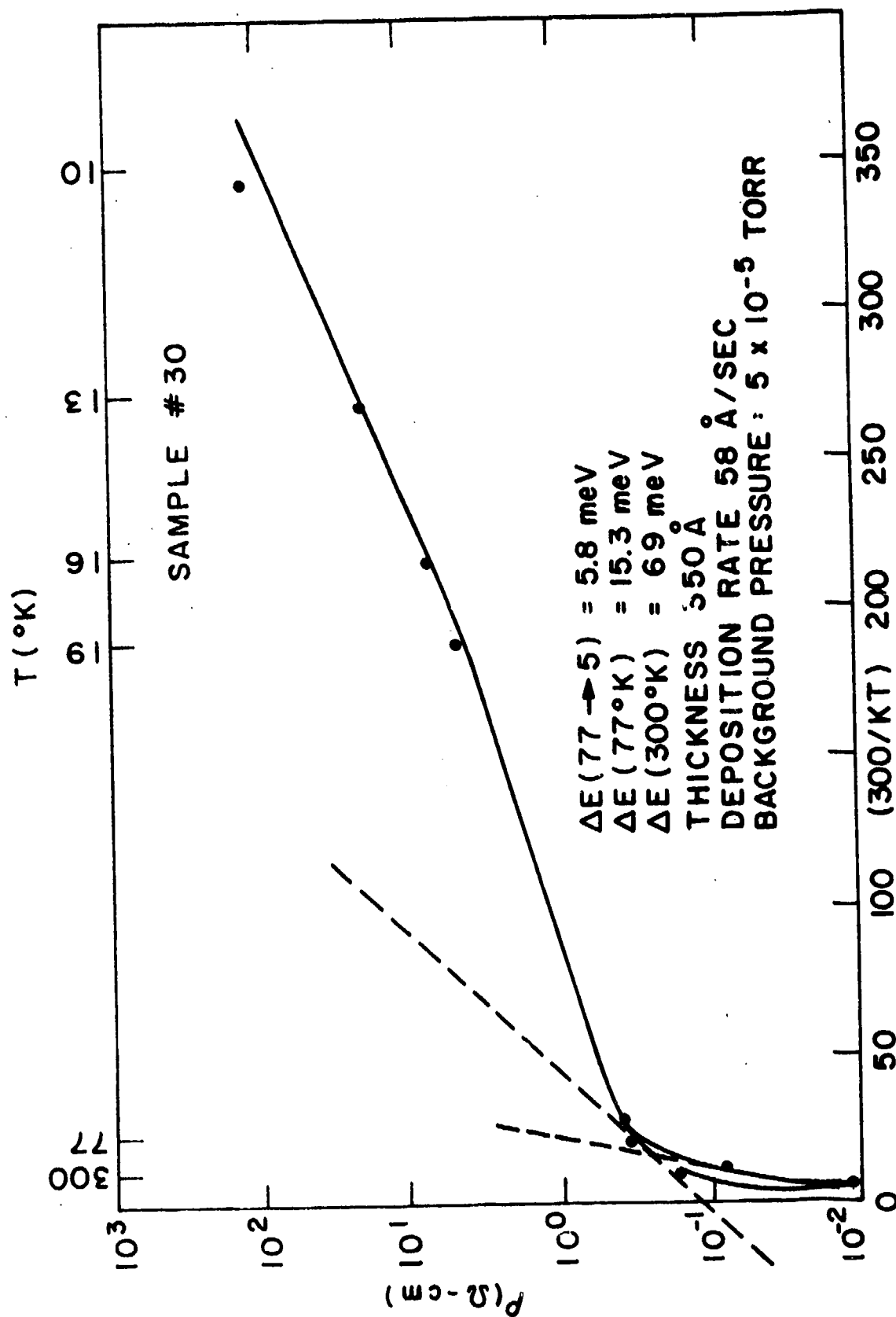


Figure 9-B:

$\ln \rho$  Vs  $T^{-1}$  Characteristics for Sample #30.

The dashed lines are the curve tangents from which the  $\Delta E$  values were estimated.



effective activation energy showing very slight deviation from 5.8 meV was observed in the 77°K to 5°K interval. Figure 9-A shows a  $\ln \rho$  vs.  $T^{-1}$  curve that typically shows minor deviations below 77°K, and a liquid helium temperature activation energy on the order of 3 meV. Samples whose resistivities were on the order of an ohm-cm exhibited shorter temperature ranges of linearity than samples whose resistivities were on the order of  $10^{-1}$  ohm-cm. Figure 9-C shows linearity from 40°K to 13°K. The resistivity independence of the temperature observed in figure 9-D below 10°K is believed to reflect limitations of the experiment rather than reflecting the properties of carbon films. This point will be discussed further in the next chapter. Samples whose room temperature resistivities were on the order of 10 ohm-cm did not show temperature intervals of linearity in the  $\ln \rho$  vs.  $T^{-1}$  characteristics. See figure 10-A; as before, the zero activation energy observed in figure 10-A below 19°K and the independence of the resistivity on temperature observed in figure 10-B below 19°K are not believed to represent carbon film behavior. The extrapolation in figure 10-B is believed to be more representative of carbon film behavior than the low temperature zero slope. Neither the activation energy nor the low temperature resistivity characteristics was obtained from films on the order of 10 ohm-cm or higher. Such films were too high in resistance to obtain reliable measurements. The high temperature  $\ln \rho$  vs.  $T$  characteristics, 300°K to 500°K, showed hysteresis similar to that of films on the order of .1 ohm cm. Also, like the more conductive films,  $\ln \rho$  vs.  $T$  is a linear relationship. See figure 10-C.

### C. Resistivity and Microstructure:

All films, regardless of their fabrication parameters and subsequent thermal cyclings remained amorphous as far as TEM analysis could discern. All films exhibited broad diffuse rings in their diffraction patterns. Figure 11-A shows the surface of a film whose thickness is 740°Å, with an evaporation rate of 123°Å/sec., evaporation pressure of  $5 \times 10^{-5}$  Torr and a room temperature resistivity of 3 ohm-cm. Figure 11-B shows the

Figure 9-A:

$\ln \rho$  Vs  $T^{-1}$  Characteristics for Sample #26.  
The dashed lines are the curve tangents from  
which the  $\Delta E$  values were estimated.



158&lt;

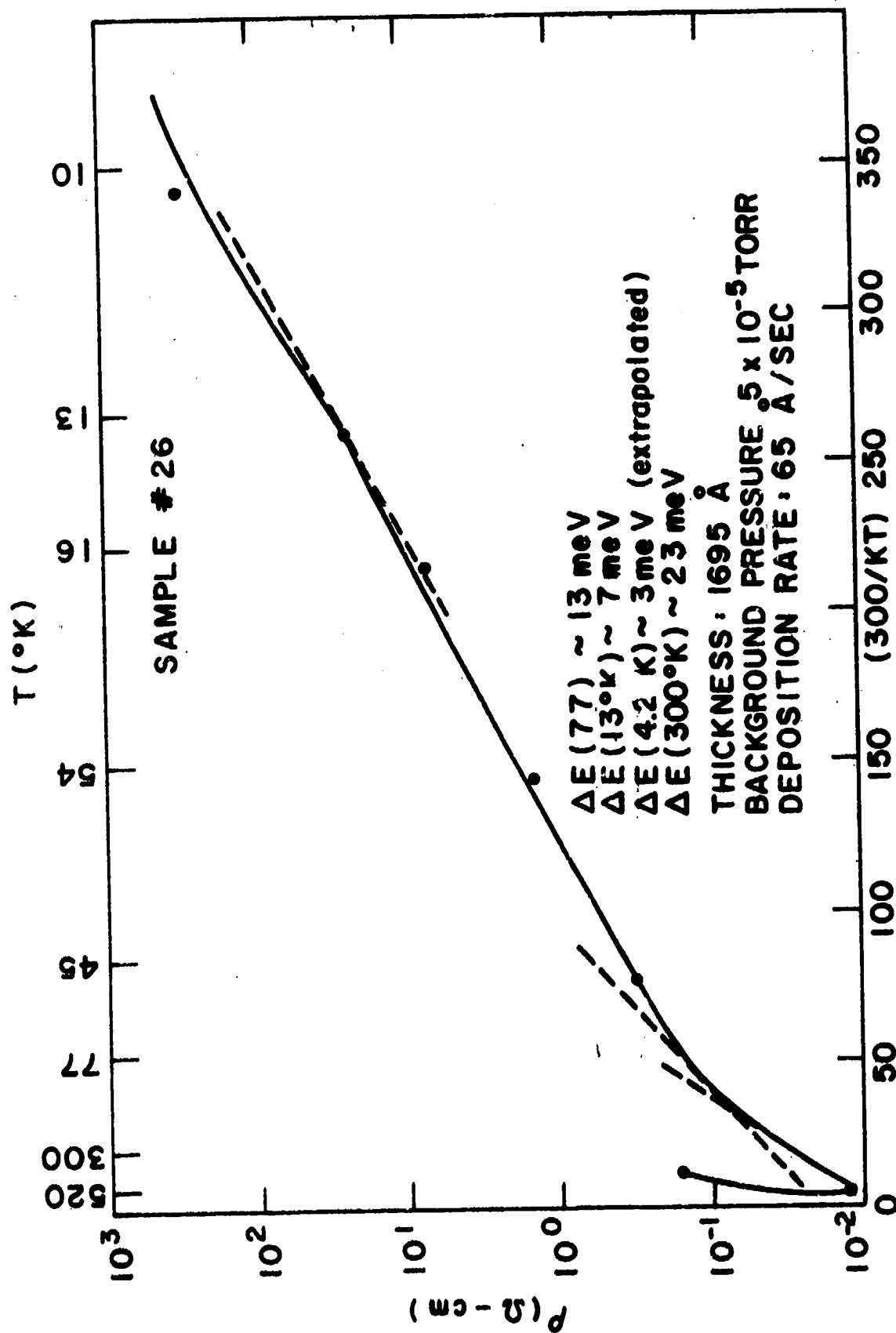
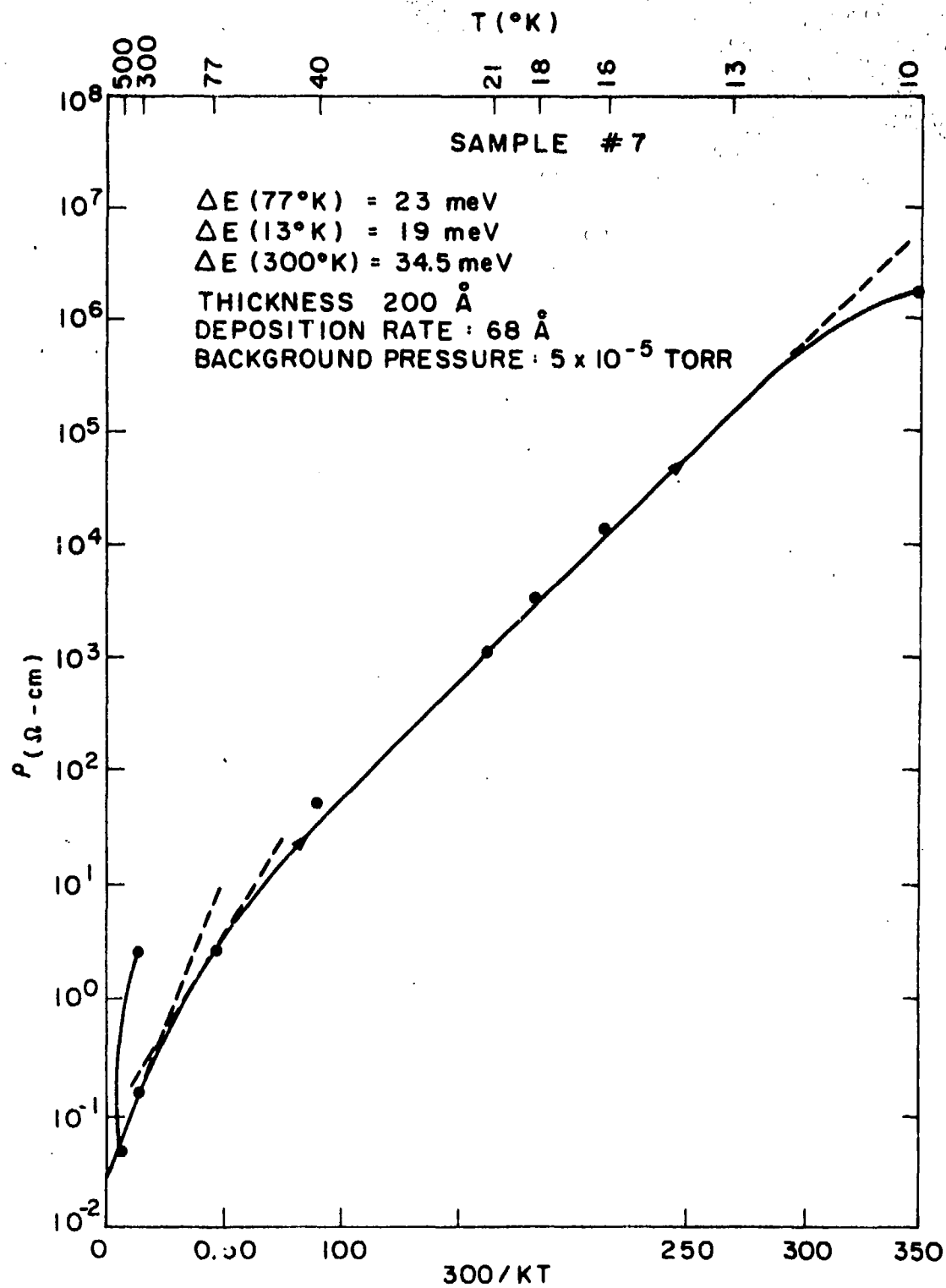


Figure 9-C:

$\ln \rho$  Vs  $T^{-1}$  Characteristics for Sample #7.  
The dashed lines are tangents to the curve  
from which the  $\Delta E$  values were estimated.

160&lt;

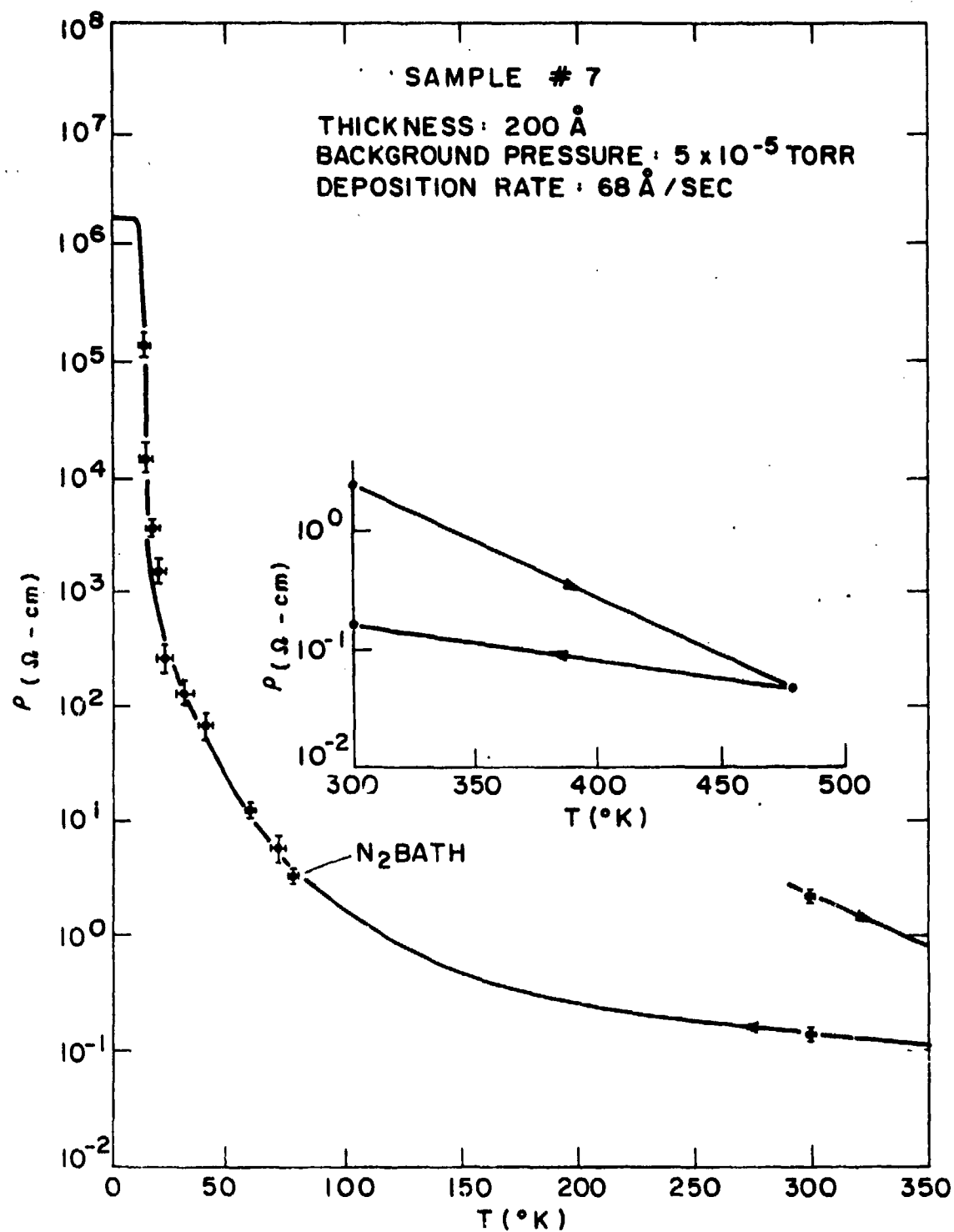


161&lt;

Figure 9-D:

*lnp* Characteristics for Sample #7.

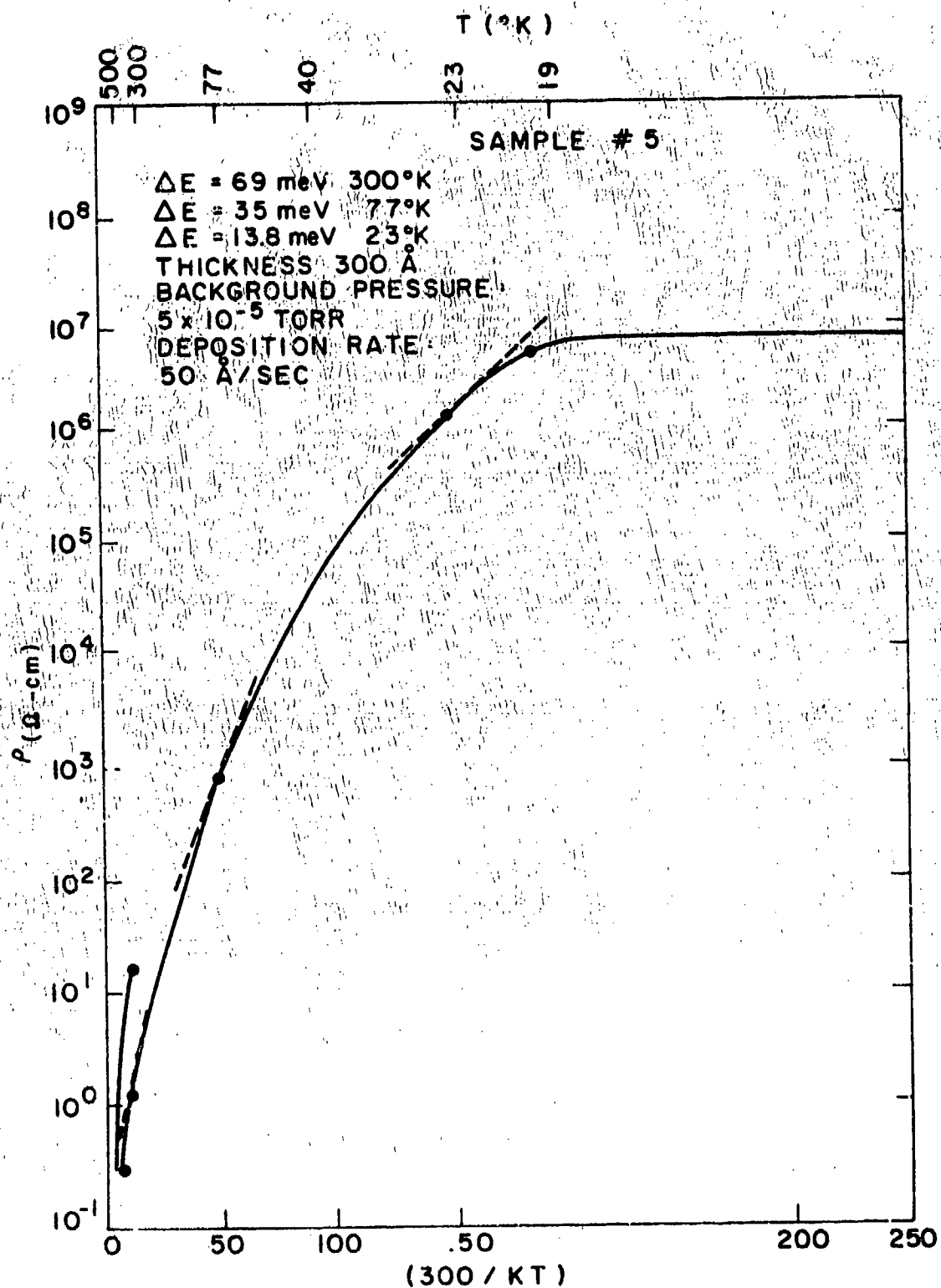
162&lt;



163&lt;

Figure 10-A

$\ln \rho$  Vs  $T^{-1}$  Characteristics for Sample #5.  
The dashed lines are tangents to the curve  
from which  $\Delta E$  values were estimated.



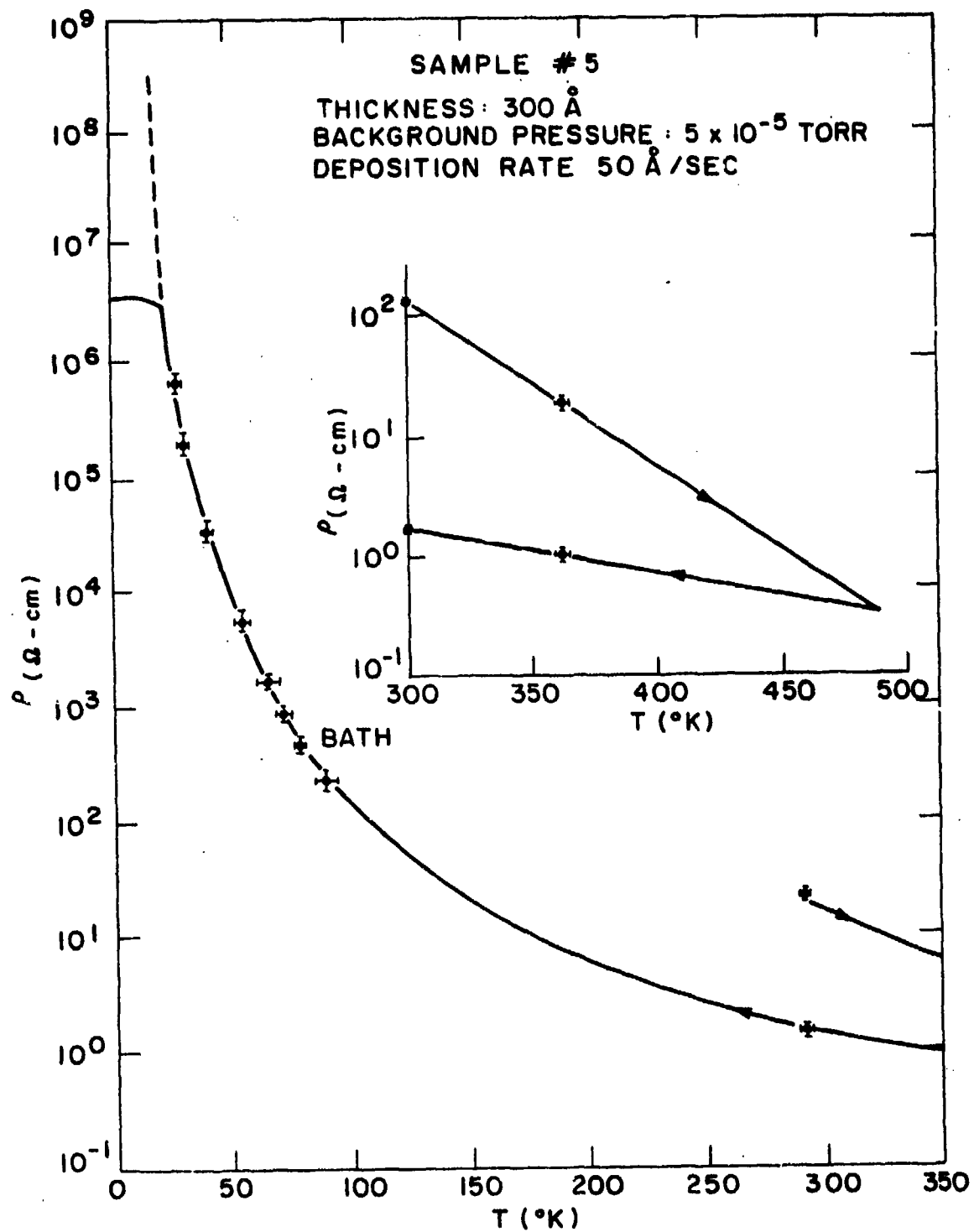
165&lt;

Figure 10-B:

$\ln \rho$  Vs T Characteristics for Sample #5.

Note:  $10^{12}$  ohm-cm and  $10^{14}$  ohm-cm are Extrapolated Resistivities at  $14^{\circ}\text{K}$  and  $4^{\circ}\text{K}$  Respectively.





167&lt;

Figure 10-C:

*h<sub>p</sub>* Vs T Characteristics for Sample #17;  
first heated, and then cooled.

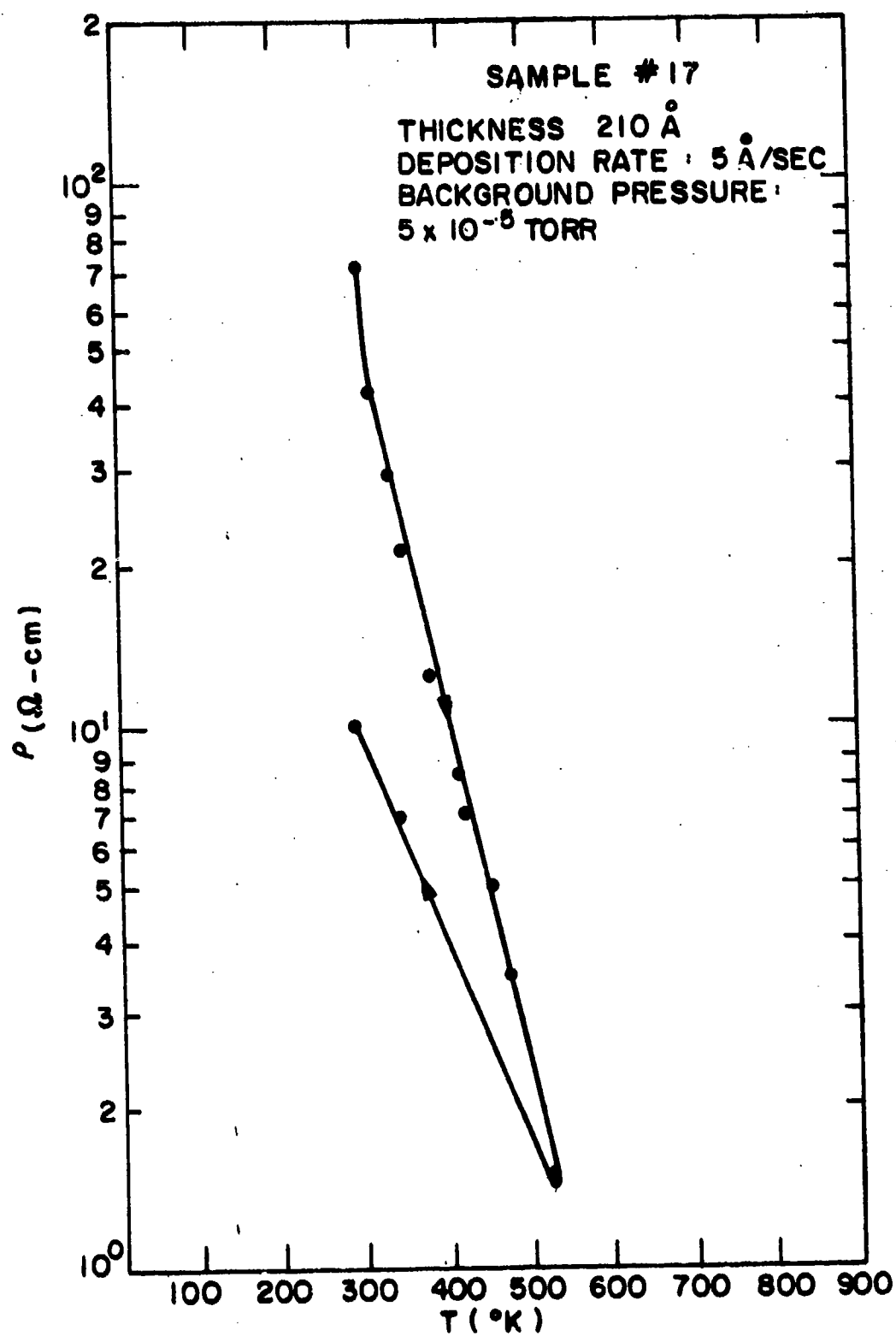


Figure 11-A:

Top of Page:

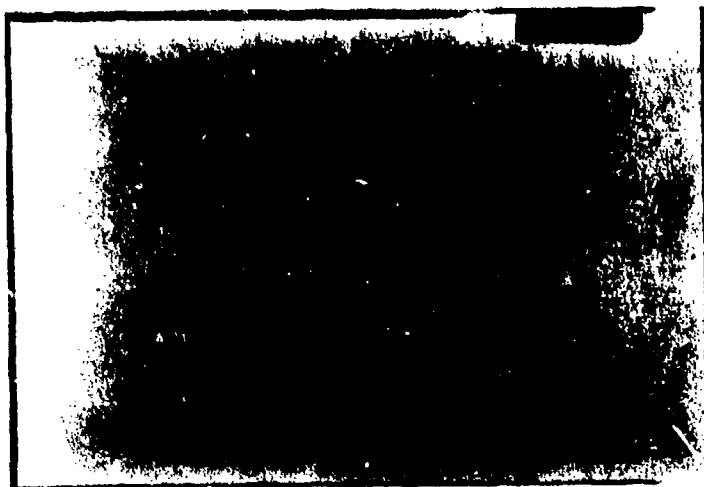
Surface of an "As Grown" Film of Thickness  
740<sup>o</sup>A; Deposited at 123<sup>o</sup>A/Sec in  $5 \times 10^{-5}$  Torr.  
Room Temperature Resistivity was 3 ohm-cm.

Figure 11-B:

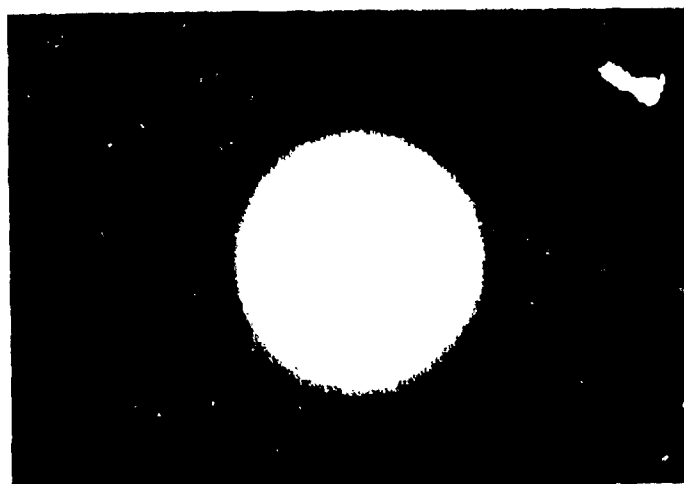
Bottom of Page:

Diffraction Pattern for this film.

170&lt;



Reproduced from  
best available copy.



corresponding diffraction pattern. Figure 11-C and 11-D show the surface, and diffraction pattern, respectively, after heating the sample to 500°K. Figure 12-A and 12-B show the surface and diffraction pattern, respectively, of a film whose thickness is 600°A, deposition rate 2°A/sec, deposition pressure of  $5 \times 10^{-5}$  Torr, and room temperature resistivity in excess of  $10^5$  ohm-cm. Figures 12-C and 12-D show the surface and diffraction pattern after heating.

Although all of the films had an amorphous structure, they did not all show linearity in their  $\ln \rho$  vs  $T^{-1/4}$  characteristics. However, it is of interest to note that samples that exhibited a temperature interval where an activation energy was well defined did not exhibit linearity in  $\ln \rho$  vs  $T^{-1/4}$ . (Compare Figure 9-B and 9-B', 9A and 9-A', 10-A and 10-A' and lastly 9-C and 9-C'.) Notice that the activation energy in 10-A is completely ill-defined; and in 10-A' the data points of that film fit the analytic expression  $\ln \rho$  vs  $T^{-1/4}$  excellently. Figures 9-A, 9-B and 9-C exhibit intervals where the activation energy is defined or deviates slightly from a defined value. The data points from these films do not fit the analytic expression  $\ln \rho$  vs  $T^{-1/4}$ . Only some temperature intervals might be interpreted as being roughly linear in  $\ln \rho$  vs  $T^{-1/4}$ . For example, Figure 9-B' seemingly shows linearity from 13°K to 5°K. Also figure 9-C' seemingly shows linearity from 300°K to 21°K. Samples 26, 30, 7 and 5 have similar fabrication parameters.

Figure 11-C:

Top of Page:

Surface of Same Sample after a Heating/Cooling  
Cycle:  $300^{\circ}\text{K} \rightarrow 500^{\circ}\text{K} \rightarrow 300^{\circ}\text{K}$

Figure 11-D:

Bottom of Page:

Diffraction Pattern of this Thermally Cycled  
Sample.

173&lt;

Reproduced from  
best available copy.

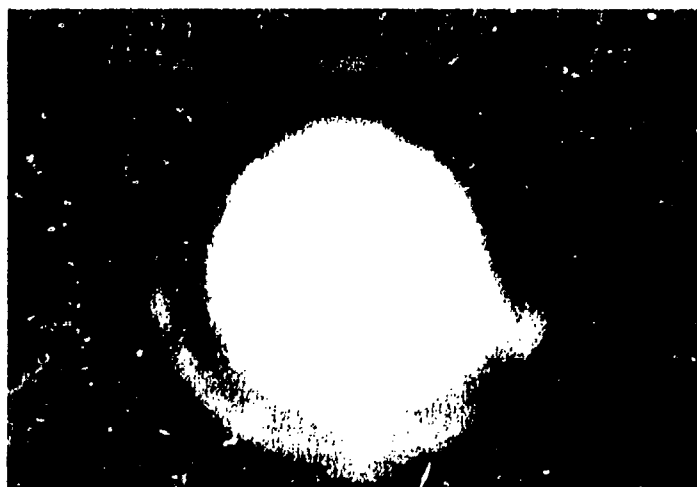




Figure 12-A:

Top of Page:

Surface of an "As Grown" Film of Thickness  $600^{\circ}\text{A}$   
 Deposited at  $2^{\circ}\text{A}/\text{Sec.}$  in  $5 \times 10^{-5}$  Torr. Room  
 Temperature Resistivity was in Excess of  $10^5$  ohm-cm.

Figure 12-B:

Bottom of Page:

Diffraction Pattern of this Film.

175<

53

Reproduced from  
best available copy.

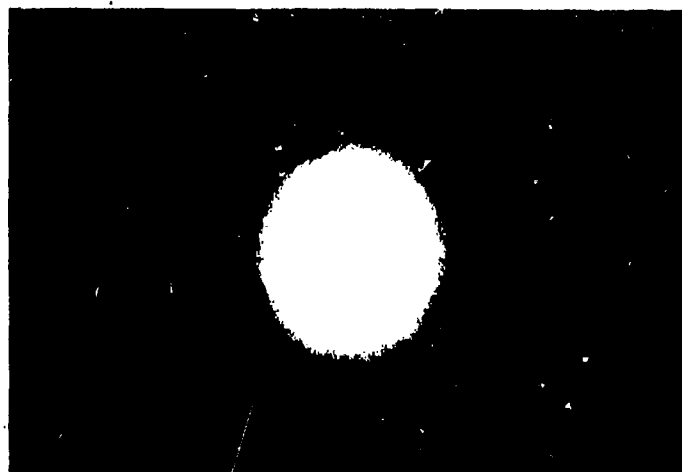


Figure 12-C:

Top of Page:

Surface of Same Sample After a Heating/Cooling  
Cycle.

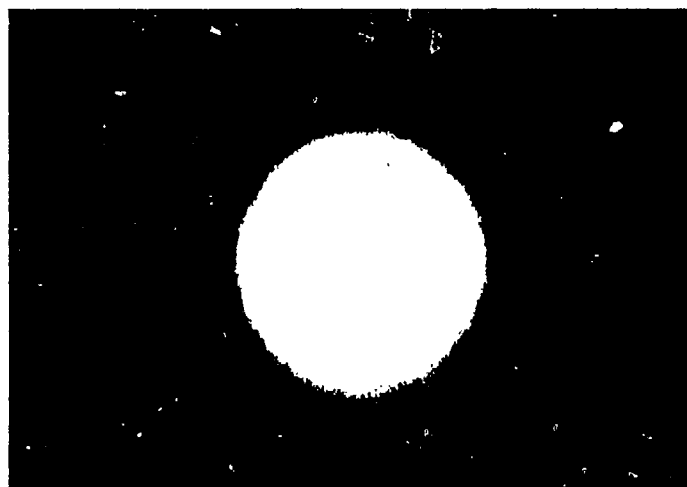
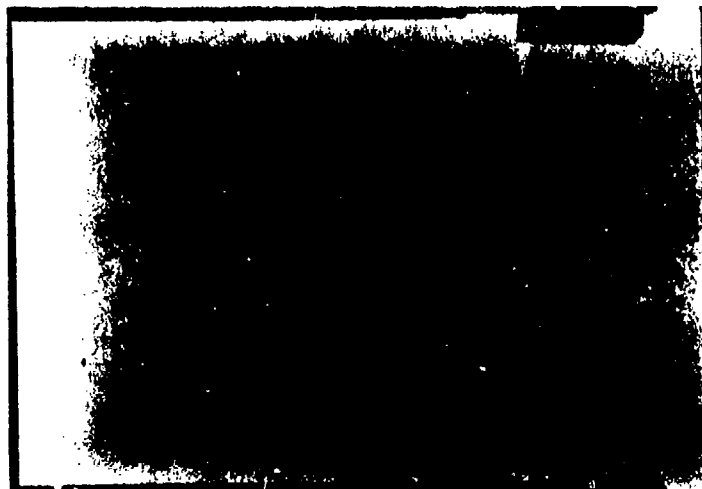
Figure 12-D

Bottom of Page:

Diffraction Pattern of This Thermally Cycled Sample.

177&lt;

Reproduced from  
best available copy.

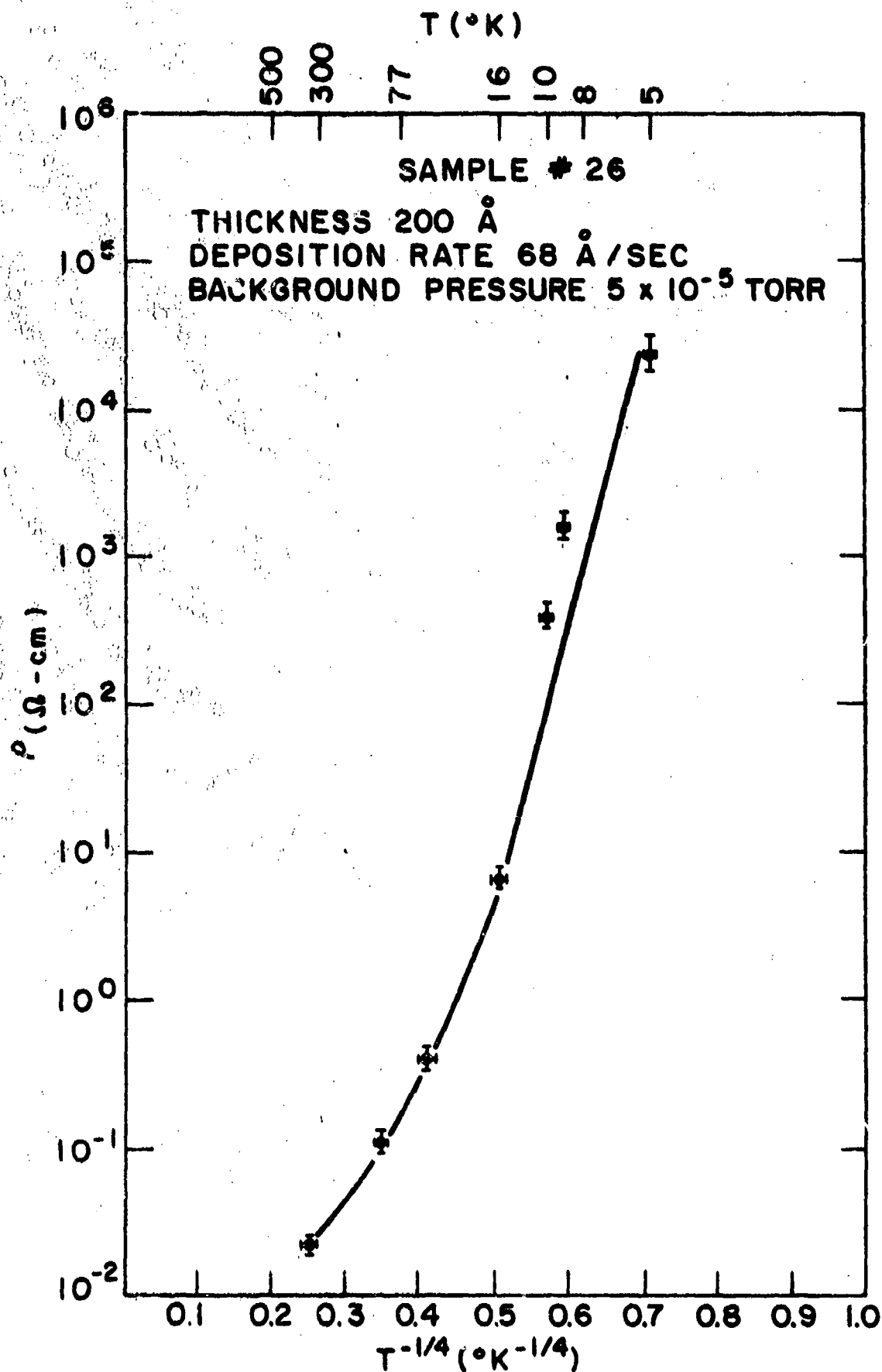


178<

Figure 9-A':  $h\rho$  vs  $T^{-1/4}$  Characteristics for Sample #26

179&lt;

55



180<

Figure 9-B':

$\ln l$  vs  $T^{-1/4}$  Characteristics for Sample #30

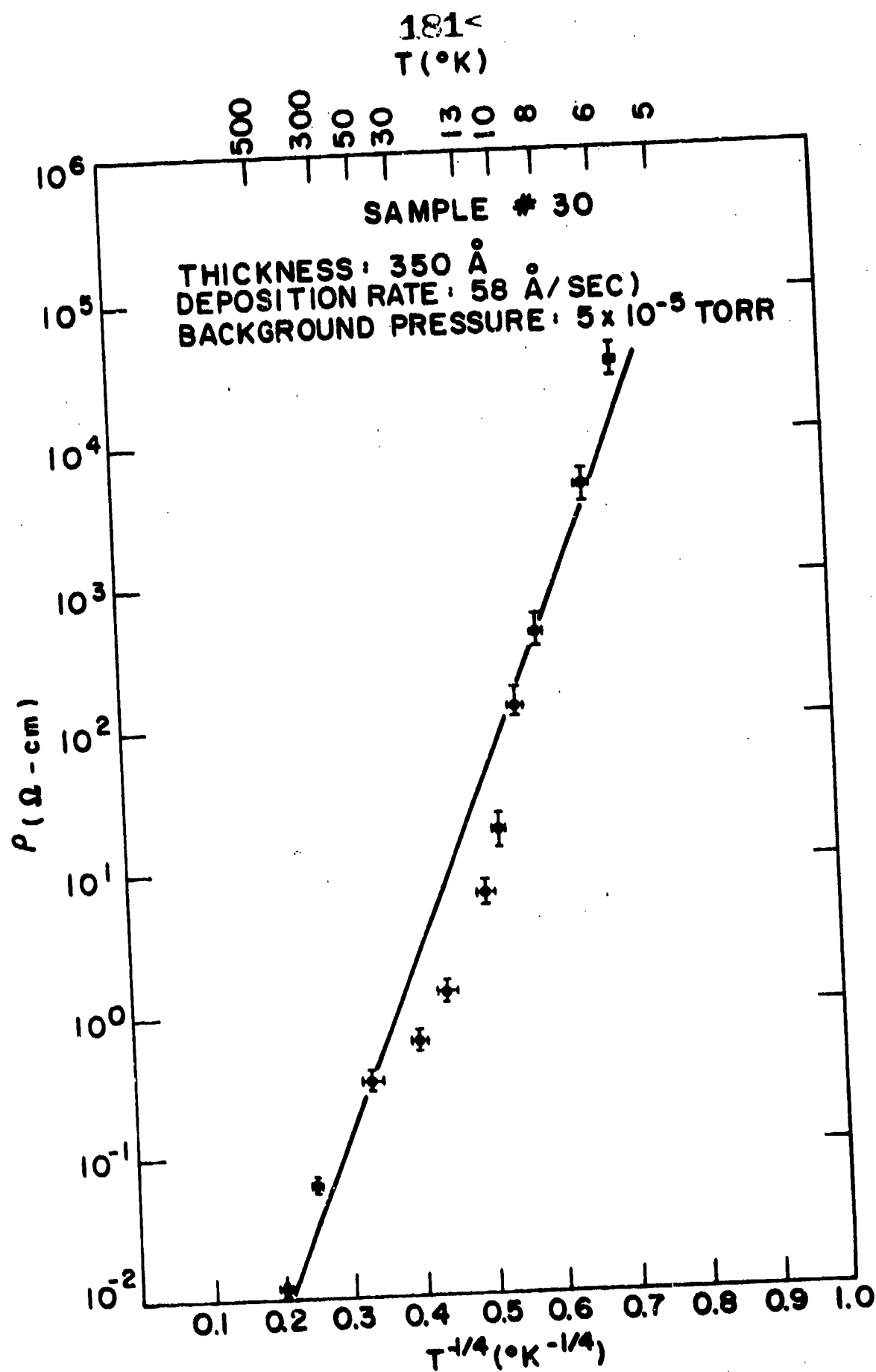




Figure 9-C':

$h\rho$  vs  $T^{-1/4}$  Characteristics for Sample #7

183&lt;

57

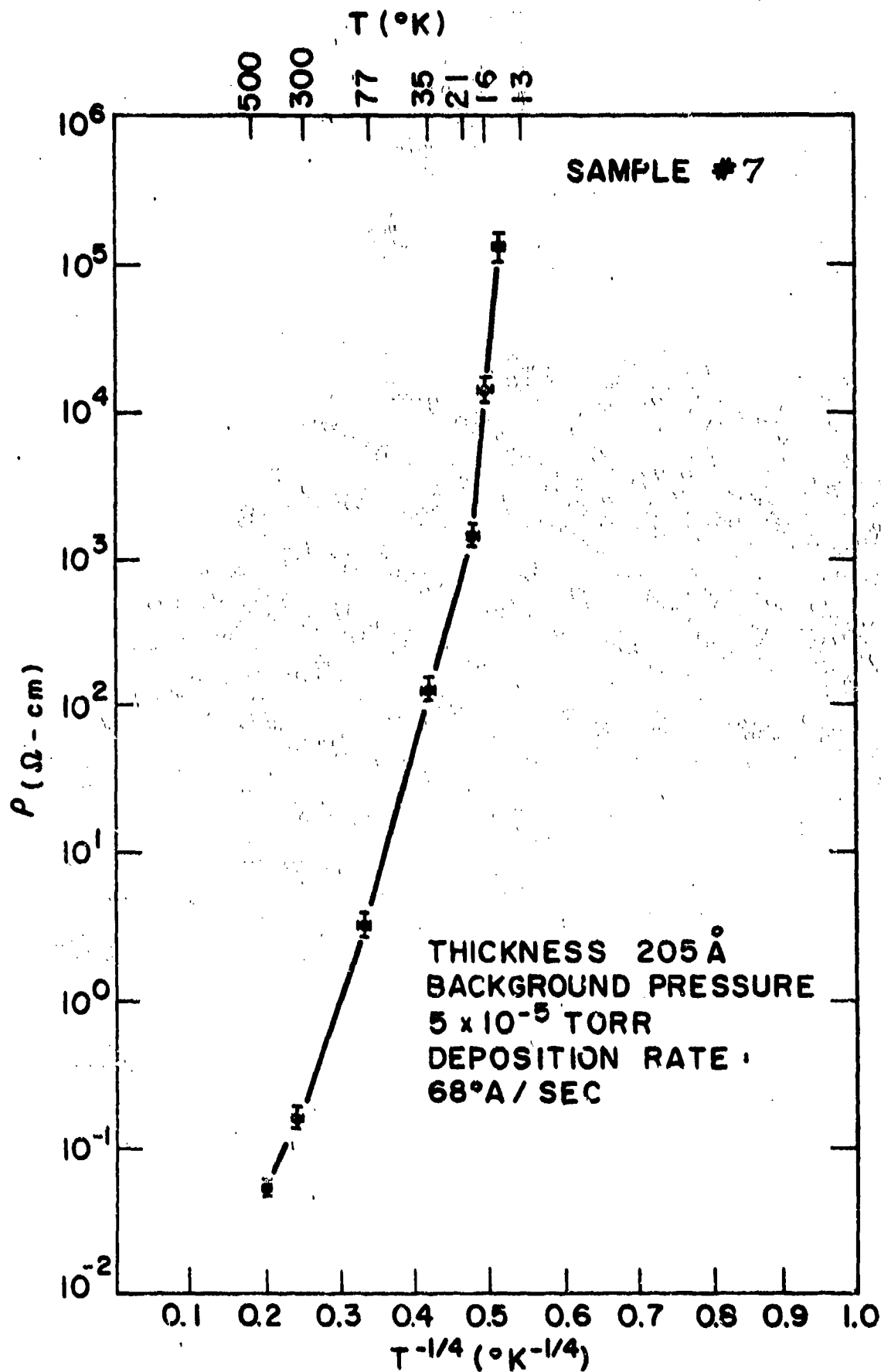
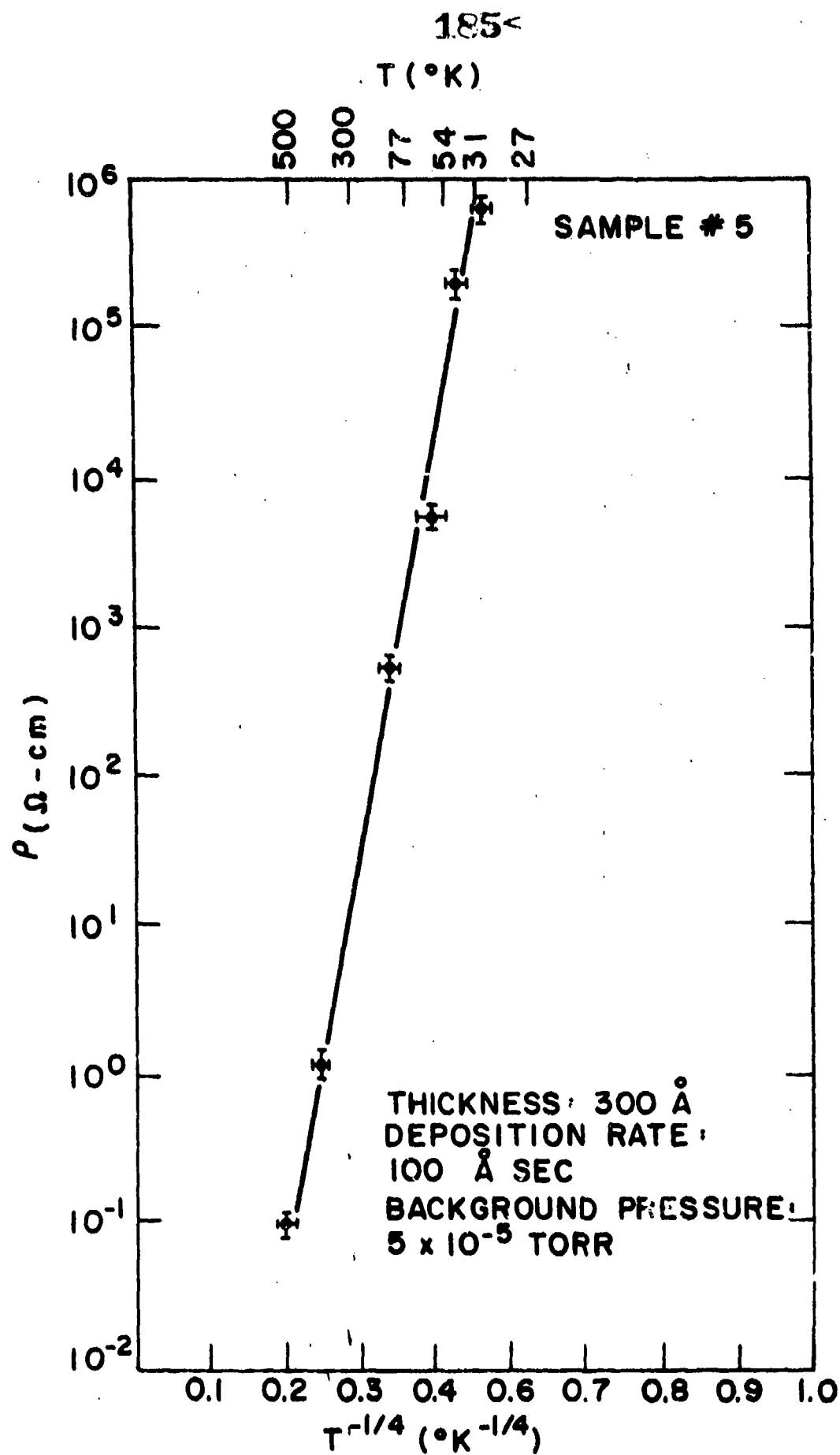


Figure 10-A' :

$h\rho$  vs  $T^{-1/4}$  Characteristics for Sample #5



## A. The Measurements:

Figure 13 shows the coplanar configuration of the carbon samples. Such a configuration lends itself to alternate current routes. The circuit diagrams that follow, figures 14 and 15-B, expose the intrinsic limitation of a coplanar configuration.

Figure 14 is a circuit diagram showing possible current routes.  $R_A$  is air resistance;  $R_C$  is carbon resistance;  $R_S$  is substrate resistance.  $R_A$  was measured by suspending the electrodes of the electrometer in air with a separation equal to the sample's electrode separation.  $R_A$  was measured to be  $10^{13}$  ohm. After determining  $R_A$   $R_S$  was measured by depositing Al electrodes on a glass substrate and attaching gold leads as in figure 15-A; 15-B shows the corresponding circuit diagram. Again, the electrometer read  $10^{13}$  which implies  $R_S \sim R_A$ . When a carbon film was deposited, the electrometer also read  $10^{13}$  ohm for temperatures less than 12°K for many samples. The author believes that an alternate current route explains the temperature independence of resistivity below 12°K observed in many samples. Since reliable data could not be taken generally below 12°K, and not below 4°K for any sample, one could not determine if samples showed hopping, basically a low temperature phenomenon.

The author offers the following comments and suggestions concerning further research on carbon films.

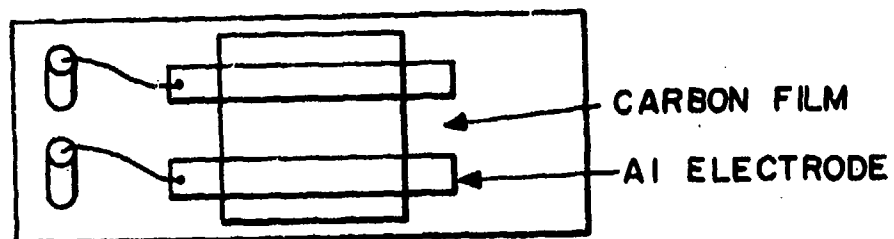
1. "As grown" films as well as films heated to 500°K appeared to remain amorphous. These films were too resistive to yield a  $\ln \rho$  vs  $T^{-1/4}$  characteristics at sub-helium temperatures. However, such films could be made more conductive if they were heat treated at higher temperatures. This would yield an improved low temperature  $\ln \rho$  vs  $T^{-1/4}$  characteristic. It is important that the films do not crystallize. Hence, a parallel study of the microstructure would be necessary.

Figure 13: Coplanar Configuration of the Carbon Samples.

Figure 14: Circuit diagram for a Coplanar Configuration.

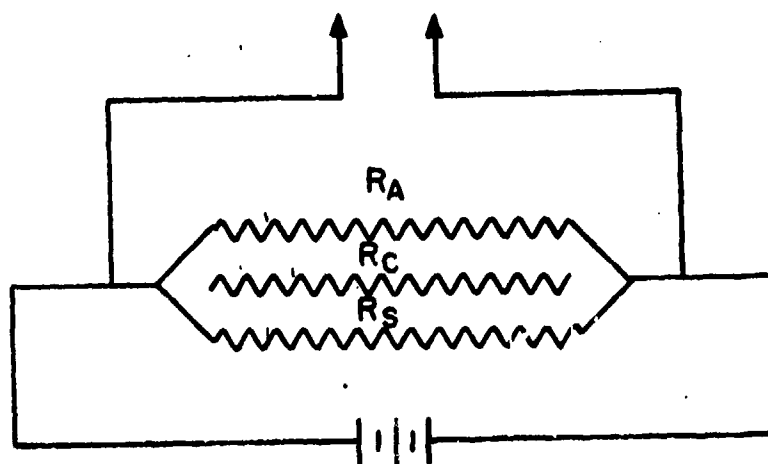
188&lt;

Au .005 WIRE



(C)

TO ELECTROMETER



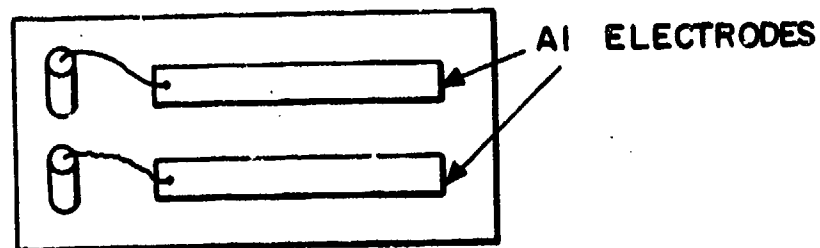
(D)

Figure 15-A: Coplanar Configuration of A<sub>Q</sub> Electrodes.

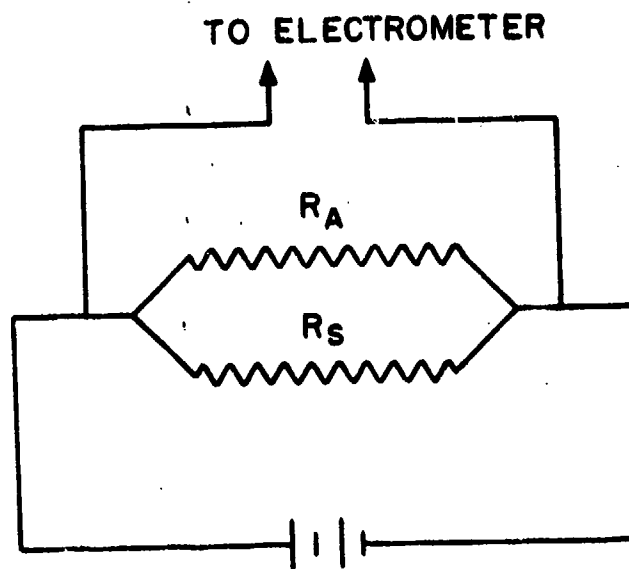
Figure 15-B: Circuit Diagram for Coplanar Electrodes.



190&lt;



Au WIRE .005  
(A)



(B)

2. Many samples did not show a fit to the Mott analytic expression  $\ln \rho \propto T^{-1/4}$  at temperatures where good behavior might be expected. Contrary to Mott's assumption, such samples might not have a uniform density of localized states. Possibly, the mobility is larger than Mott's calculation indicated, or possibly, the density of states does not have over-lapping bands. A study of the band structure would be useful to determine whether or not the criterion for Mott hopping is satisfied.

192&lt;

The accuracy of the resistivity was determined as follows:

$$\rho = \rho' \pm \delta \rho' \quad R = R' \pm \delta R' \quad t = t' \pm \delta t'$$

where

$\rho$  is the actual resistivity;  
 $\rho'$  is the measured resistivity; and  
 $\delta \rho'$  is the experimental error in

Since

$$\rho = \frac{\epsilon_e}{\epsilon_s} (Rt)$$

where

$\epsilon_e$  is the electrode length,  
 $\epsilon_s$  is the electrode separation,  
 $R$  is the sample's resistance, and  
 $t$  is the sample's thickness, then

$$\delta \rho' = \epsilon_e / \epsilon_s [t \delta R' + R' \delta t'],$$

where  $\delta R'$  is experimental error in sample's resistance.

$\delta t$  is experimental error in sample's thickness.

Thus,

$$\delta R' / R = 1\% \quad 10\%$$

$$\delta t / t = 1\% \quad 20\%$$

$$\delta \rho' / \rho' = 10\% \quad 20\%$$

For temperatures in the 4°K to 20°K,  $\delta T(\%)$  was 1°K where  
 is the experimental error in temperature measurement. The ratio  
 $\delta T / T$  was 20% to 5%.

Similarly,  $\delta T / T$  was 10% to 6% for  $T = 20^\circ\text{K}$   $30^\circ\text{K}$ .

Finally,  $\delta T / T$  was 6% 4% for  $T = 30^\circ\text{K}$   $77^\circ\text{K}$ .

Temperatures from 300°K to 500°K (as measured by the oven) were accurate to 2°K by temperature measurement independent from that of the oven.

Activation energies were estimated by extracting tangents to the curve generated by the analytic expression  $\ln P \propto T^{-1}$ . These estimated values are felt to be accurate to  $\pm 15\%$ .

The general conclusion by workers in the field is that the resistivity of carbon films, like the resistivity of other types of amorphous thin films, is determined by impurity content of the films, and microstructure. The author's results do not confirm a dependence of carbon resistivity on microstructure for the observed temperature range, 4°K to 500°K. However, sensitivity to microstructure may well exist above this range. Debenyl et al found in his study that temperature in excess of 500°K were required to induce structural changes.<sup>(15)</sup>

Samples fabricated by the author at deposition rates in excess of 10°A/sec in  $5 \times 10^{-5}$  Torr, exhibited resistivities whose order of magnitude was 83% reproducible for thicknesses greater than 100°A. Samples grown with the same fabrication parameters, except vacuum pressure was in the  $10^{-4}$  Torr or  $10^{-3}$  Torr range, also showed approximately 83% reproducibility. Blue and Danielson's investigation showed, and the author's work confirms in detail, that the order of magnitude of the resistivity is indeed reproducible for films greater than 100°A in thickness and deposition rate in excess of 10°A/sec.<sup>(8)</sup> However, for samples of deposition rate less than 10°A/sec, pressure again  $5 \times 10^{-5}$  Torr, and thickness on the order of 200°A, the author observed over six orders of magnitude variation in room temperature resistivity. There was no evidence of variations in microstructure. Kupperman et al, using arc-evaporated 500°A films deposited on glass substrates at 5°A/sec in  $10^{-5}$  Torr vacuum, observed more than two orders of magnitude variation in room temperature resistivity.<sup>(6)</sup> They suggested that variations in gas concentration during evaporation were responsible for the irreproducible room temperature resistivity. The author feels that such variations in impurity atmosphere during film formation are a likely cause of resistivity irreproducibility in slow deposition rate data.

\*Using arc-evaporated films with thickness between 100°A and 2300°A, background pressure at  $10^{-4}$  Torr, and a deposition rate of 50°A/sec, Blue and Danielson reproduced the order of magnitude of room temperature resistivity as a function of thickness.

Morgan, using an electron beam to sublime his out-gassed graphite rods, obtained reproducible room temperature resistivity as a function of film thickness for deposition rates less than  $10^0 \text{A/sec}$  Torr vacuum.<sup>(11)</sup> The authors' investigation cannot really be compared to Morgan's since a different sublimation procedure was used. However, for arc-evaporated films, the author's investigation showed no relation between out-gassing of the graphite rods and the reproducibility of room temperature resistivity.

Adkins et al, using an electron beam to sublime graphite in a  $10^{-5}$  Torr vacuum, made in situ measurements of resistivity versus thickness during film growth.<sup>(9)</sup> His films had a terminal thickness of  $2500^0 \text{A}$  and a deposition rate of less than  $10^0 \text{A/sec}$ . Samples of the same thickness showed large variations in room temperature resistivity. Adkins et al, suggested that variations in grain size and impurity content caused the irreproducibility. While impurity content, as has been said, most certainly influenced the author's reproducibility of film resistivity (at least for room temperature measurements and slow deposition rates), contrary to Adkins et al, variation in grain size cannot account for the large variations observed in the author's slow rate films since TEM studies revealed no structure even for a resolution of  $2^0 \text{A}$ . Further comparison to Adkins et al cannot be made since the author used neither an electron beam method, nor made in situ measurements because his films were too resistive. The response time of the electronics was too slow to monitor the resistance in its dynamic state.

The author's room temperature resistivity for films deposited at rates in excess of  $50^0 \text{A/sec}$  at  $5 \times 10^{-4}$  Torr to thicknesses between  $490^0 \text{A}$  and  $740^0 \text{A}$  showed resistivities between 6.2 ohm-cm and 17 ohm-cm. Blue and Danielson, also using arc-evaporation, observed resistivities between 1.3 ohm-cm and 6.6 ohm-cm for the same deposition parameters.<sup>(8)</sup>

The author observed room temperature resistivities typically in the .4 ohm-cm to 4 ohm-cm range for films deposited in  $5 \times 10^{-5}$  Torr at  $> 10^0$  A/sec. Using arc-evaporation and similar deposition parameters, J. Kakinoki observed resistivities typically on the order of 1 ohm-cm on NaCl substrates.<sup>(12)</sup> Morgan, using an electron beam, and Kupperman et al, using arc-evaporation, grew films at deposition rates less than  $10^0$  A/sec.<sup>(11,6)</sup> However, Morgan and Kupperman et al obtained resistivities that were much lower than the author's. They obtained values typically on the order of .1 ohm-cm, and between .2 ohm-cm and 1 ohm-cm, respectively; whereas the author obtained values between 67 ohm-cm and  $10^7$  ohm-cm for similar deposition parameters.

Kupperman et al observed in arc-evaporated films at  $5^0$  A/sec that resistivity versus room temperature was reproducible for temperatures below the fabrication temperature,  $300^0$  K.<sup>(6)</sup> The author did not extend his resistivity versus temperature characteristics below  $300^0$  K for slowly evaporated film; they were too resistive in general. However, the author did observe reproducibility in resistivity versus temperature for temperatures  $< 300^0$  K for films deposited at rates in excess of  $10^0$  A/sec. Resistivity versus temperature was reproducible for all films for temperatures above  $300^0$  K, only after several heating and cooling cycles.

The author observed hysteresis in the first few thermal cycles for  $\ln \rho$  vs T. J. Kakinoki also observed hysteresis for similarly prepared films.<sup>(12)</sup> The hysteresis, he explained, resulted from a temperature dependent ratio of diamond-like regions to graphite-like regions. The author, however, believes that the hysteresis results from outgassing of the samples, thereby activating carrier states that had been neutralized by impurities.

The author observed linearity in the  $\ln \rho$  vs  $T^{-1/4}$  characteristics over the observed temperature range,  $500^0$  K to  $31^0$  K, for samples that showed an ill-defined activation energy over this temperature range. Only brief temperature intervals of linearity were observed in the

characteristics of samples exhibiting a region of defined activation energy. However, there were no distinguishing factors of fabrication in samples that showed a well-defined activation energy for the entire temperature range, and samples that showed a well-defined activation energy for only brief temperature intervals. Kupperman investigated resistivity versus temperature for 500 $^{\circ}$ A films arc-evaporated at 5 $^{\circ}$ A/sec in  $\sim 10^{-5}$  Torr vacuum.<sup>(6)</sup> The investigated temperature range was 1.2 $^{\circ}$ K to 1100 $^{\circ}$ K. Kupperman observed Mott hopping from 4 $^{\circ}$ K to 20 $^{\circ}$ K and well-defined activation energies from 550 $^{\circ}$ K to 670 $^{\circ}$ K and 670 $^{\circ}$ K to 1100 $^{\circ}$ K. Although Kupperman used a slower deposition rate than the author, 5 $^{\circ}$ A/sec as opposed to  $> 10^{\circ}$ A/sec for the author, and a longer investigated temperature interval, 1.2 $^{\circ}$ K to 1100 $^{\circ}$ K as opposed to 4 $^{\circ}$ K to 500 $^{\circ}$ K for the author, Kupperman's data, like the author's, exhibited linearity in  $\ln \rho$  vs  $T^{-1/4}$  in a non-extended temperature interval. Morgan, however, observed linearity only below 8 $^{\circ}$ K for films that were electron-beam deposited at 2 $^{\circ}$ A/sec.<sup>(11)</sup> The activation energy, was ill-defined over the observed temperature range, 5 $^{\circ}$ K to 300 $^{\circ}$ K. Neither Adkins nor Blue and Danielson investigated activation energy for phonon assisted tunneling.



### C. Summary

The purpose of the experiment was to investigate conduction in thin arc-evaporated carbon films as a function of fabrication parameters: film thickness, deposition rate, vacuum pressure, and prior out-gassing of the graphite rods. In particular, it was desired to obtain the temperature dependence of conductivity and information on the sensitivity of conductivity to film microstructure. Conductivity is generally independent of thickness for thicknesses in excess of  $100\text{\AA}$ . Films less than  $100\text{\AA}$  usually have resistivities several orders of magnitudes higher than films grown under identical conditions but greater than  $100\text{\AA}$  in thickness.

Resistivity is independent of evaporation rate for rates greater than  $10\text{\AA}/\text{sec}$ . Below this rate, resistivities were as much as five to six orders of magnitudes higher. For the  $5 \times 10^{-3}$  Torr to  $5 \times 10^{-5}$  Torr pressure range, resistivity increased monotonically with increasing background pressure. Films grown at  $5 \times 10^{-4}$  Torr were typically an order of magnitude higher in resistivity than films grown at  $5 \times 10^{-5}$  Torr. By increasing the pressure to  $5 \times 10^{-3}$  Torr, the resistivity typically increased an additional 50 ohm-cm. It is conclusive from the deposition rate and background pressure dependences of the resistivity that background impurities during film function affect the resistivity value.

Chemical spectrographic analysis and residual gas analysis showed that new contaminants were not introduced into the system by out-gassing the graphite rods, consistent with the experimental observation that no changes were observed in resistivity as a result of out-gassing the graphite rods. Pre-or post-deposition of the Al electrodes relative to the carbon film was also immaterial to the carbon film resistivity values measured. This is indicative that the pre-deposited Al electrodes are not damaged by high velocity carbon ions, nor the carbon films affected by post-deposited electrodes.

All samples showed monotonic increases in resistivity with decreasing temperatures. Samples observed from 300°K to 4°K showed increases in resistivity on the order of  $10^6$  ohm-cm. In general,  $\ln \rho$  vs  $T^{-1}$ , as well as  $\ln \rho$  vs  $T^{-1/4}$ , showed non-linear characteristics. Also in general, the activation energy was ill-defined for the observed temperature range (typically 500°K to 15°K). However, many samples exhibited ranges of temperature where the activation energy showed only slight deviation from being well-defined. Samples that did show an ill-defined activation energy for all temperature, exhibited linearity in  $\ln \rho$  vs  $T^{-1/4}$ . Typically, 50 meV activation energy was observed at 300°K; 20 meV at 77°K; and 3 meV at 5°K.

All films showed an amorphous structure to a 20Å resolution on the TEM.

The early steps of the investigation, for no apparent reason, sometimes yielded resistivities that were high relative to values obtained later in the experiment. Since many early values were ill-typically high, the author omitted the first 40 samples data from figure 14. Figure 15 is a plot of resistivity versus thickness for all samples, and Table 4 is a master table of all samples. One can observe from the master table that while many of the 40 original samples had typical resistivities, others did not.

Figure 14:

A Plot of Resistivity Versus Thickness. The Original  
40 Data Points are not Included.

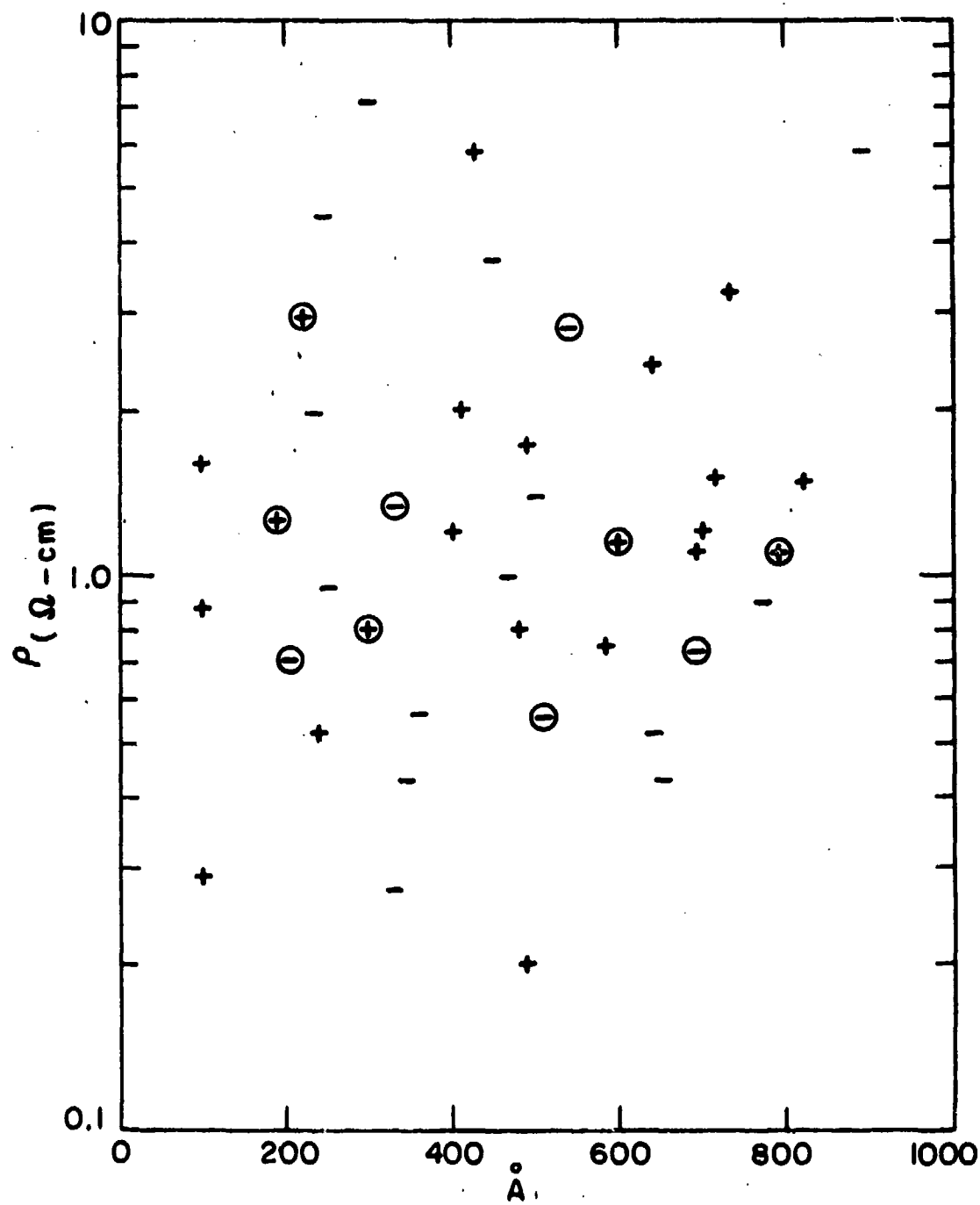


Figure 15: A Plot of Resistivity Versus Thickness for all Samples.

204

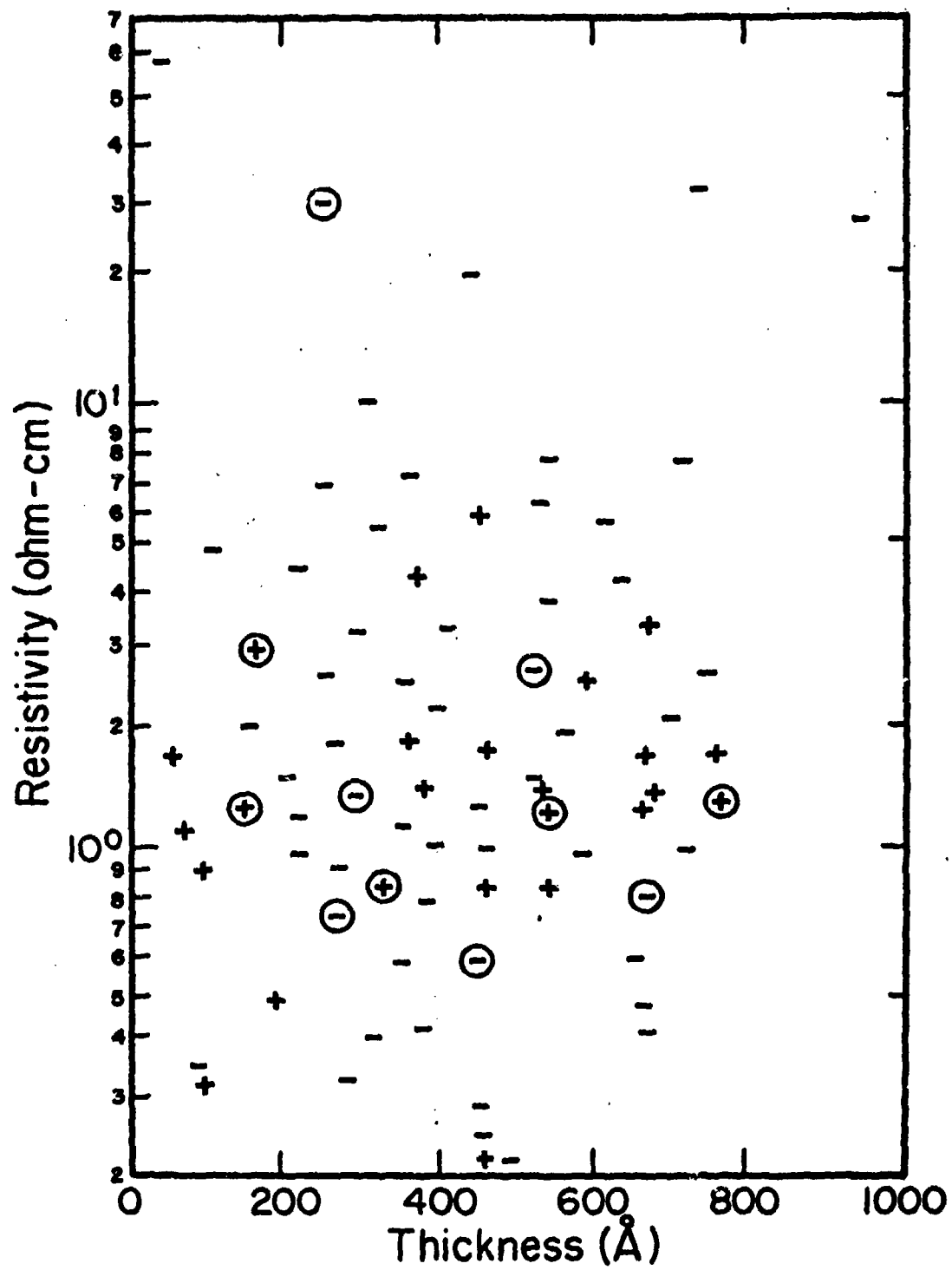


Table 4: A Master Table for all Fabricated Samples.



Table 4  
(Master Table)

S#	$\rho$ (ohm-cm)	Thickness ( $\text{\AA}$ )	Deposition Rate ( $\text{\AA}/\text{Sec}$ )	Pressure Torr
1	32.0	300	70	$5 \times 10^{-5}$
2	20.0	450	70	$5 \times 10^{-5}$
3	10.0	300	30	$5 \times 10^{-5}$
4	14.8	344	80	$5 \times 10^{-5}$
5	31.0	300	50	$5 \times 10^{-5}$
7	02.7	205	68	$5 \times 10^{-5}$
8	09.5	280	90	$5 \times 10^{-5}$
9	30.7	768	96	$5 \times 10^{-5}$
10	07.2	512	28	$5 \times 10^{-5}$
11	03.59	418	42	$5 \times 10^{-5}$
12	01.2	570	57	$5 \times 10^{-5}$
13	02.4	412	70	$5 \times 10^{-5}$
14	00.88	490	75	$5 \times 10^{-5}$
15	01.2	130	13	$5 \times 10^{-5}$
16	01.13	256	40	$5 \times 10^{-5}$
17	67.0	210	5	$5 \times 10^{-5}$
18	00.25	412	40	$5 \times 10^{-5}$
19	00.25	1695	65	$5 \times 10^{-5}$
20	00.33	896	75	$5 \times 10^{-5}$
21	00.29	287	57	$5 \times 10^{-5}$
22	00.4	167	42	$5 \times 10^{-5}$
23	00.82	37	45	$5 \times 10^{-5}$
24	100	30	115	$5 \times 10^{-5}$
25	00.14	603	121	$5 \times 10^{-5}$
26	00.24	693	46	$5 \times 10^{-5}$
27	00.42	160	75	$5 \times 10^{-5}$
28	07.9	512	28	$5 \times 10^{-5}$
29	00.33	287	57	$5 \times 10^{-5}$
30	00.23	350	58	$5 \times 10^{-5}$

S#	$\rho$ (ohm-cm)	Thickness ( $\text{\AA}$ )	Deposition Rate ( $\text{\AA}/\text{Sec}$ )	Pressure Torr
31	00.39	490	49	$5 \times 10^{-5}$
32	00.25	310	50	$5 \times 10^{-5}$
33	00.46	100	20	$5 \times 10^{-5}$
35	20.5	470	50	$5 \times 10^{-5}$
36	03.2	120	60	$5 \times 10^{-5}$
39	30.0	950	65	$5 \times 10^{-5}$
40	30.0	800	45	$5 \times 10^{-5}$
45	01.68	490	81	$5 \times 10^{-5}$
47	01.26	185	20	$5 \times 10^{-5}$
48	01.6	100	33	$5 \times 10^{-5}$
49	00.12	491	80	$5 \times 10^{-5}$
50	00.75	590	197	$5 \times 10^{-5}$
51	00.88	100	33	$5 \times 10^{-5}$
52	00.29	100	11	$5 \times 10^{-5}$
53	00.53	245	50	$5 \times 10^{-5}$
54	01.58	710	60	$5 \times 10^{-5}$
55	00.80	482	160	$5 \times 10^{-5}$
56	01.1	690	115	$5 \times 10^{-5}$
57	27.0	1050	58	$5 \times 10^{-5}$
58	03.8	704	118	$5 \times 10^{-5}$
59	05.9	428	70	$5 \times 10^{-5}$
60	03.2	560	80	$5 \times 10^{-5}$
61	$8 \times 10^7$	245	"	$5 \times 10^{-5}$
62	07.5	250	7	$5 \times 10^{-5}$
-	$5 \times 10^3$	260	6	$5 \times 10^{-5}$
63	$8 \times 10^3$	50	3	$5 \times 10^{-5}$
64	128	50	3	$5 \times 10^{-5}$
65	17	740	123	$5 \times 10^{-4}$
66	15.4	350	58	$5 \times 10^{-4}$
67	06.2	490	98	$5 \times 10^{-4}$
68	26.5	980	163	$5 \times 10^{-3}$
69	69	980	175	$5 \times 10^{-3}$

208&lt;

76

S#	$\rho$ (ohm-cm)	Thickness ( $\text{\AA}$ )	Deposition Rate ( $\text{\AA}/\text{Sec}$ )	Pressure Torr
70	74	740	74	$5 \times 10^{-3}$
71	70	700	80	$5 \times 10^{-3}$
72	2.2	400	60	$5 \times 10^{-5}$
73	3.0	250	75	$5 \times 10^{-5}$
74	5.0	400	90	$5 \times 10^{-5}$
75	1.0	500	40	$5 \times 10^{-5}$
76	.8	300	110	$5 \times 10^{-5}$
77	.2	500	115	$5 \times 10^{-5}$
78	.23	500	35	$5 \times 10^{-5}$
79	.28	100	65	$5 \times 10^{-5}$
80	.45	400	70	$5 \times 10^{-5}$
81	.46	700	83	$5 \times 10^{-5}$
82	7.0	300	67	$5 \times 10^{-5}$
83	0.2	500	120	$5 \times 10^{-5}$
84	1.3	600	100	$5 \times 10^{-5}$
85	1.3	700	20	$5 \times 10^{-5}$
86	1.4	750	57	$5 \times 10^{-5}$
87	1.2	780	90	$5 \times 10^{-5}$
88	0.7	200	119	$5 \times 10^{-5}$
89	0.8	250	30	$5 \times 10^{-5}$
90	0.89	720	60	$5 \times 10^{-5}$
91	6.0	420	53	$5 \times 10^{-5}$
92	2.0	210	42	$5 \times 10^{-5}$
93	6.0	410	45	$5 \times 10^{-5}$

## REFERENCES

1. D. Adler, Electronics 43: 61-72 (1970).
2. D. Adler, Amorphous Semiconductors, (Chemical Rubber Co., CRC Press; Cleveland, Ohio, 1971) pp 14-26.
3. A.K. Jonscher, Thin Solid Films 1 : 213-234 (1967).
4. N.F. Mott, Adv. Phys., 16: 49 (1967).
5. M.H. Cohen, Phys. Today, "Theory of Amorphous Semiconductors", pp. 26-32 May 1971.
6. D.S. Kupperman, C.K. Chau and Weinstock, Carbon, 11: 171 (1972).
7. C.J. Adkins, S.M. Freake and E.M. Hamilton, Phil Mag. 22: 183 (1970).
8. M.D. Blue and G.C. Danielson, J. App. Phys. 28: 583 (1956).
9. C.J. Adkins and E.M. Hamilton, Conduction in Low-Mobility Materials, Proceedings of the Second International Conference Eilat, Israel, 5-8 April 1971 (Taylor and Francis Ltd; N.Y., 1971).
10. R. Grigorovici, Thin Solid Films, 9: 1-23 (1971).
11. M. Morgan, Thin Solid Films, 7: 313 (1971).
12. J. Kakinoki, Proceedings of the Fifth Conference on Carbon, Vol. 2, University Park, Penn. June 19-23, 1961 (Pergamon Press, 1961).
13. B.T. Boiko, L.S. Palatnik and A.S. Derevyanchenko, Sov. Phys. Dokl., 13: 237 (1968).
14. H. Toyoda and M. Nagashima, J. Phys. Soc. Jap., 14: 274 (1959).
15. A. Debenyl, A. Gheorghin, A. Belu and G. Korony, Conduction in Low Mobility Materials, Proceedings of the Second International Conference, Eilat, Israel, 5-8 April 1971 (Taylor and Francis Ltd; N.Y., 1971).

210<

SEMI-ANNUAL TECHNICAL REPORT #3

Period: July 1, 1974 - December 31, 1974

Title: Research in Materials Sciences

Project Title: Chemical Synthesis Using High Temperature  
Lithium Vapor Species

Contract Number: DAHC 15-73-C-0316

ARPA Order Number: 2469

Program Code Number: 3D10

Name of Contractor: Massachusetts Institute of Technology  
Cambridge, Mass. 02139

Principal Investigator: N. J. Grant (617) 253-5638

Project Scientists or Engineers: Prof. R. Lagow (617) 253-5617

Effective Date of Contract: June 1, 1973

Contract Expiration Date: May 31, 1975

Amount of Contract: \$770,233.

Amount of Project: \$124,798

Sponsored By

Advanced Research Projects Agency

ARPA Order No. 2469

The views and conclusions contained in this document are those of the authors and should not be interpreted as necessarily representing the official policies, either expressed or implied of the Advanced Research Projects Agency or the U. S. Government.

Summary of Research Progress in the Synthesis Characterization  
and Reactions of Polylithium Compounds

Professor R. J. Lagow

Over the past three months, this project has reached a degree of maturity such that the phase of our research program involving the synthesis of polymers and diamond-like materials has been initiated. The initial studies in several areas have been very promising. However, the major problem remains the purification and separation of the novel polylithium compounds.

The polymer synthesis program is developing in three different areas. These are the synthesis of polymers in a high pressure - high temperature apparatus, the synthesis of three dimensional polymers in solution, and the synthesis of polymers by means of gas phase reaction. The first high pressure - high temperature studies were conducted a month ago in a tetrahedral anvil system. A large amount of effort has been devoted over the past year to the construction of a large high temperature - high pressure press which is capable of obtaining 40 Kilobar pressures at 400°C with significant reaction container sizes on the order of 2 inches in diameter. Calibration runs were made in November on this new apparatus. Because the starting materials for these polymer syntheses had been produced in our program several months ago and because the potential value of these experiments is so great, a graduate student was flown to a tetrahedral anvil facility in Houston to conduct preliminary studies on the program and in a related area. Even though the container size for such a high pressure device is only one-eighth inch in diameter, eight experiments were conducted. The results are now being evaluated. With the completion of the larger scale high pressure apparatus extensive experimentation will be undertaken in this area during the next fiscal year, with this being one of the most important efforts anticipated.

Very promising and exciting results have been obtained in the development of synthetic reactions in solution between monomer polylithium compounds and difunctional alkanes. The reaction of dilithiomethane,  $\text{H}_2\text{CLi}_2$ , with methylene chloride,  $\text{H}_2\text{CCl}_2$ , and with 1,2 dichloroethane have yielded higher alkanes and a polymer which is very much like polyethylene. This result is a giant step toward the synthesis of three dimensional

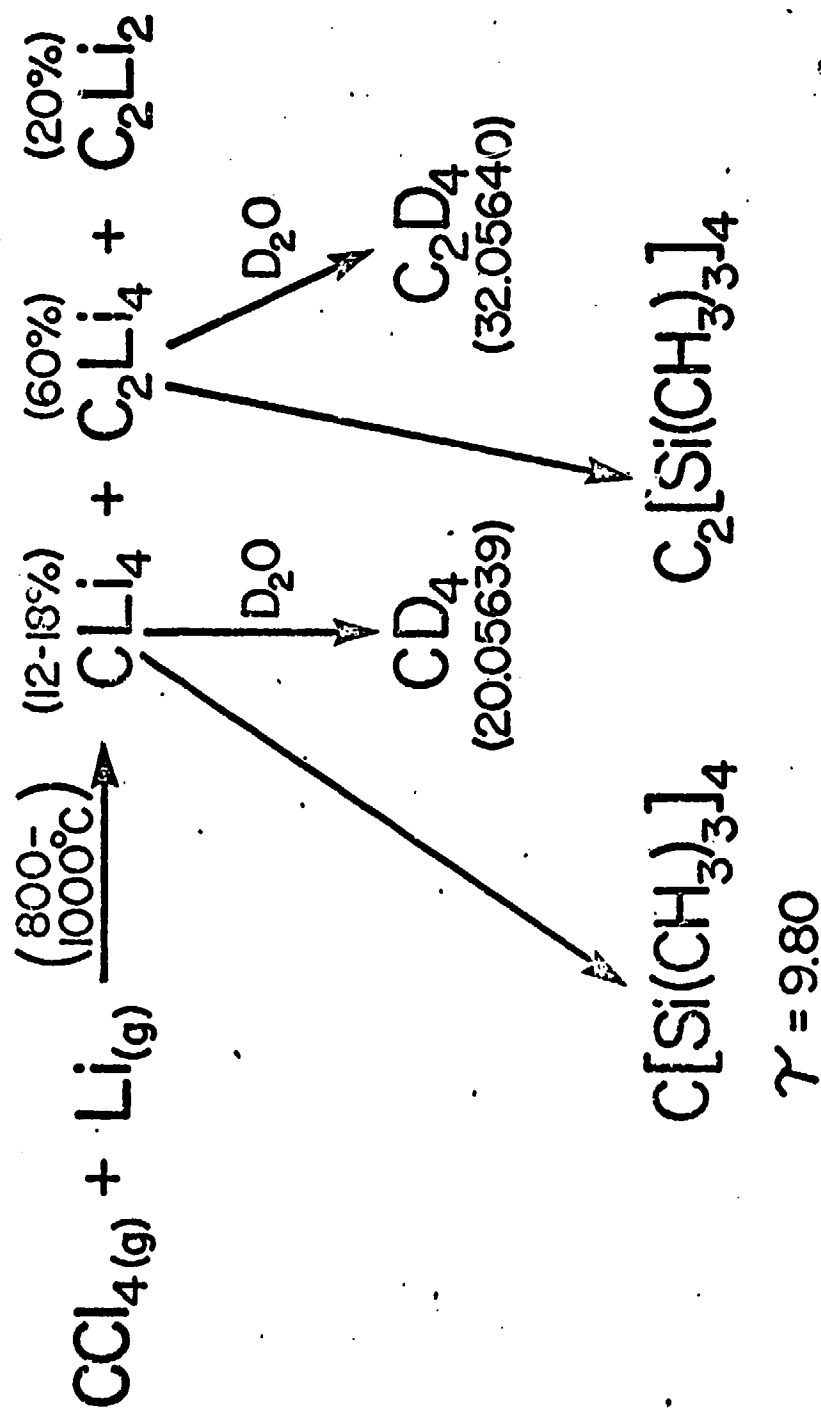
polymers from other polylithium compounds and indicates the feasibility of such processes. Efforts to maximize and establish the molecular weights are underway.

The discovery that polylithium compounds such as  $C_3Li_4$  may be vaporized without extensive decomposition has led to an experimental program designed to study the reaction of such vapor species with difunctional monomeric materials. The degree of polymerization of such reaction products is under study.

Earlier in our program, a study of the reaction of carbon tetrachloride,  $CCl_4$  and the reaction of hexachloroethane  $C_2Cl_6$  was conducted with lithium vapor at a  $1000^\circ C$ .<sup>1</sup> The products of the initial reaction were tetralithiomethane  $CLi_4$  and tetralithioethene  $Li_2C-CLi_2$ . (See Figure 1.) These compounds were characterized and it has been found that they react with various organic and inorganic substrates in the manner characteristic of other lithium compounds such as the conventionally prepared monolithium compounds. This experimental result provides evidence of the suitability of such polylithium compounds for reactions as monomers in the proposed diamond-like polymer systems. Subsequently, the reaction of hexachloroethane (see Figure 2) with lithium produced hexolithioethane in approximately 80 per cent yield. Again this material has been shown to be a potentially reactive monomer.

A study of the reaction of carbon vapor generated from a carbon arc apparatus at  $2500^\circ C$  (see Figure 3) was undertaken to establish an alternative method for synthesizing polylithium compounds.<sup>2</sup> (See Figure 4.) The principal product was  $C_3Li_4$  which appears to have the allene structure and might be an attractive monomer. Varying amounts of tetralithiomethane and tetralithioethylene were also produced in this study.

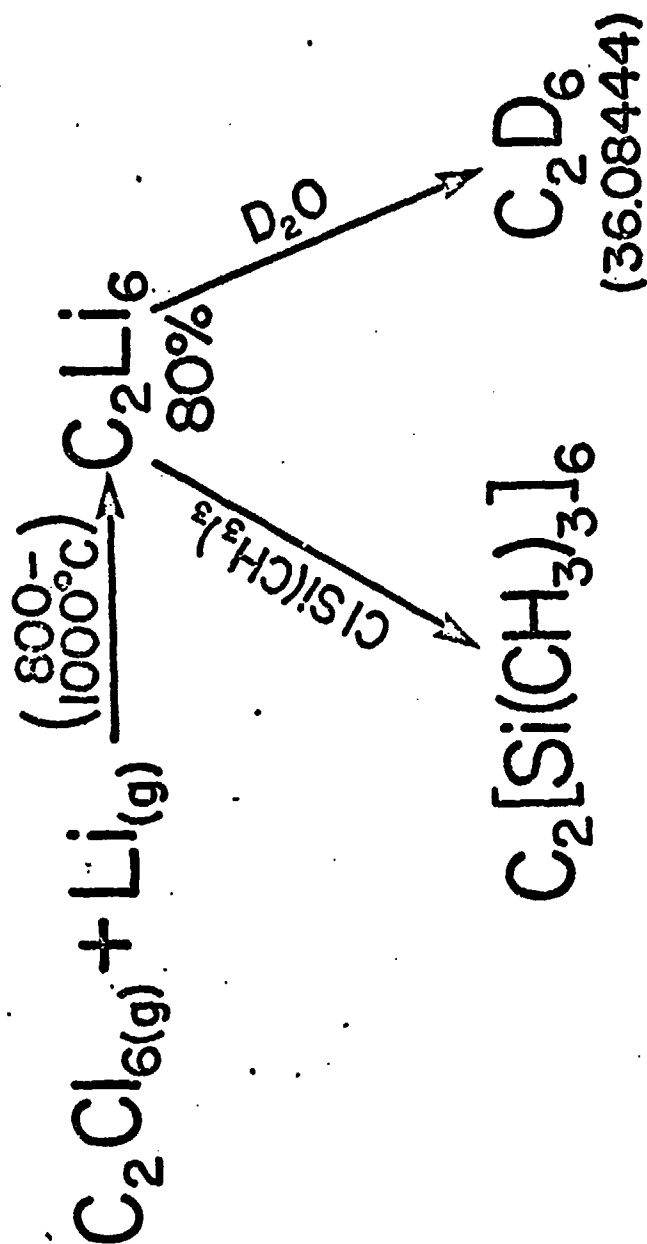
A third publication has resulted from the reaction of lithium vapor with benzene.<sup>3</sup> While for most of our systems the reactants are admitted to the reactor at room temperature and reacted with the high temperature lithium vapor, initial studies giving a small yield of hexalithiobenzene prompted us to do a more extensive study based on the reaction of lithium vapor plus benzene at various temperatures. A new type of reactor was designed for this purpose. At room temperature one gets a distribution of lithiated benzene ranging from over the range of  $C_6Li_{6-n}H_n$  where  $n = 1$  to 6. At room temperature the species of highest yield is dilithiobenzene. As one raises the temperature progressively to  $800^\circ C$  a



C. Chung and R.J. Lagow, Chem. Comm. 1078 (1972)

Fig. 1





C. Chung and R.J. Lagow,  
Chem. Comm. 1078, (1972)

Fig. 2

215<

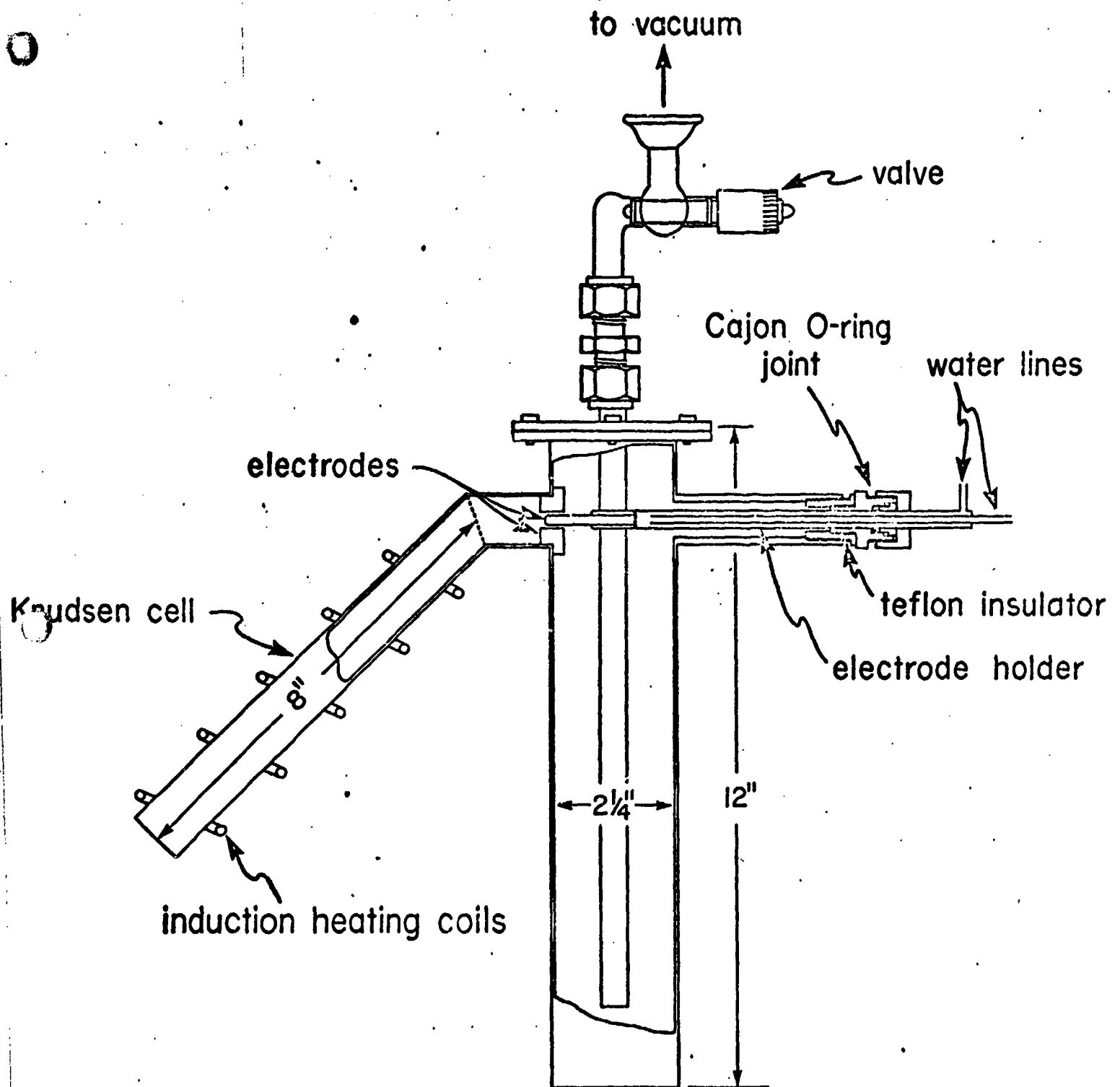
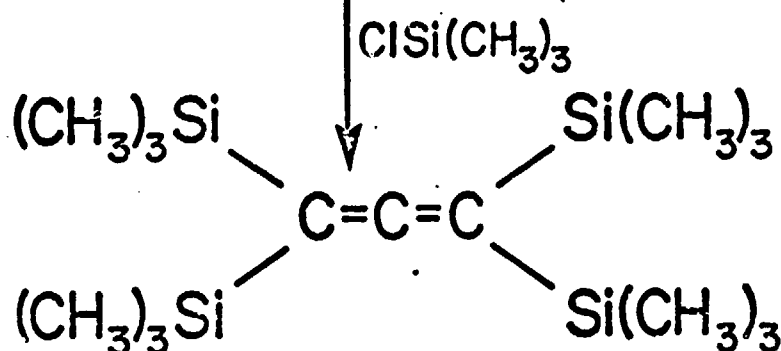
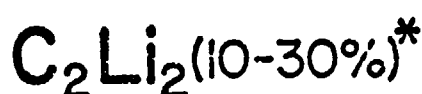
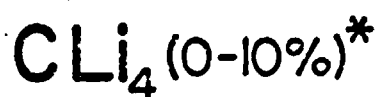
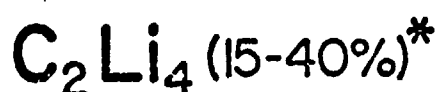
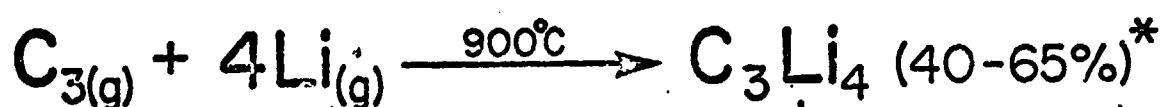
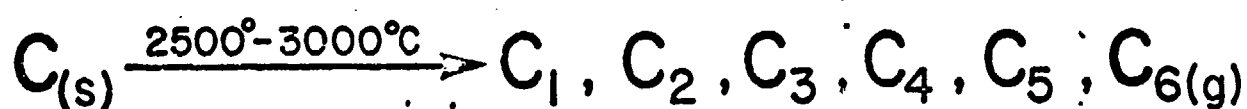


Fig. 3



$$\gamma = 9.89$$

\* Based on Carbon Vaporized

L. A. Shimp and R. J. Lagow, J. Am. Chem. Soc. 95,  
1343 (1973)

Fig. 4

shift toward the higher benzene polylithium compounds is noted. The temperature of the benzene is raised to  $900^{\circ}\text{C}$  and a striking new result is attained. One begins to obtain polylithiated cyclohexanes from the benzene starting material. This results from a tendency for the lithium to add to the double bonds as well as replace the protons on the ring. Studies were made up to temperatures of  $1200^{\circ}\text{C}$  producing such striking compounds as perlithiocyclohexane and  $\text{C}_6\text{Li}_6\text{H}_6$ . It has been found subsequently that the reaction of hexachlorobenzene with lithium provides a much cleaner route to hexalithiobenzene.<sup>4</sup>

The reaction of methane gas with lithium has also been extensively investigated.<sup>5</sup> We predicted and found that lithium at  $1000^{\circ}$  will not react with methane gas at room temperature. The activation energy for this reaction appears to be in the 30 kcal mole range. Lithium at  $1000^{\circ}\text{C}$  usually has about 3 kcal mole of translational or kinetic energy and only a very small percentage of lithium in the first excited electronic state. Therefore, the activation energy for the lithium-methane reaction is not likely to be available under these reaction conditions. The reaction between methane and lithium would be a very important one for the production of tetralithiomethane which we consider to be one of the important materials in subsequent polymer synthesis. We have used several approaches to provide the activation energy for this reaction. We have found that if we either electronically excite the lithium or vibrationally excite the methane the reaction proceeds in a satisfactory manner. We have conducted an experiment in which the methane was heated to  $900^{\circ}\text{C}$  and obtained satisfactory results. Increased temperatures populate higher vibrational strates in the methane and thus allow a very significant decrease in the activation energy of the reaction. We also used a radio frequency source to excite the lithium vapor electronically and produced a successful reaction. Still another piece of work has been done using a methane plasma source which vibrationally excites the methane and allows the reaction to proceed. The most important result in this area is discussed in the "newest results" section and involve the study of the reaction of lasar induced electronically excited lithium.

In the study of tetralithiomethane, a fourth synthesis is being completed which involves initial synthesis of dilithiomethane and subsequent pyrolysis to give a substantial yield of tetralithiomethane.<sup>6</sup> Using this method we have obtained substantial quantities of tetralithiomethane.

Extensive work has been done on solvent systems for tetralithiomethane so that one may do the polymer synthesis in solution. Several successful solvent systems are being developed and the concentrations of the poly-lithium compounds in solution are being determined by NMR studies and the preparation of derivatives.

An extensive study has been recently completed on the reactions of olefins with lithium vapor.<sup>7</sup> (See Figure 5.) A large number of new polyolithium compounds such as tetralithio cyclohexadiene, 2,3 dilithio 2 butene, 2,3 tetralithio 2 butene, 1,2 dilithio isobutane, 1,4 dilithio 2 butene, and 1,2 trilithio isobutane have been prepared in this study. We have seen instances of both substitution for hydrogen on sites requiring a low activation energy for reaction and addition to double bonds. This study has established another general route to polyolithium compounds.

Studies of reactions of inorganic species with lithium have also been undertaken. The reaction of silicon tetrachloride,  $\text{SiCl}_4$ , with lithium has been recently studied and the polyolithium compound  $\text{SiLi}_4$  was obtained in good yield.<sup>8</sup> Hydrolysis and deuterolysis of the compound produced silanes and perdeutero silanes. A subsequent study of the reaction of tetralithiosilane with methyl chloride resulted in a 15 per cent yield of tetramethyl silane indicating that the  $\text{SiLi}_4$  is also a potential monomer. The reaction of  $\text{BCl}_3$  and  $\text{PCl}_3$  are currently under study. A fair yield of trimethylborane  $\text{B}(\text{CH}_3)_3$  was obtained from the reaction of  $\text{Bli}_3$  with methyl chloride. Additionally the synthesis of polyolithiated carboranes has been attempted and a workup is now in progress. Isolation of a higher purity  $\text{SiLi}_4$  is being undertaken. It should be pointed out that if the diamond syntheses from tetralithiomethane are successful, a synthesis of a silicon analog for a diamond will be attempted using the  $\text{SiLi}_4$ . Such a diamond-like silicon structure would have many unusual electrical and physical properties. This type of structure has been the object of numerous unsuccessful synthetic studies utilizing the phase diagram of silicon. This potentially valuable species has previously eluded all other synthetic approaches.

# Major Products of the Reaction of Lithium with Alkenes

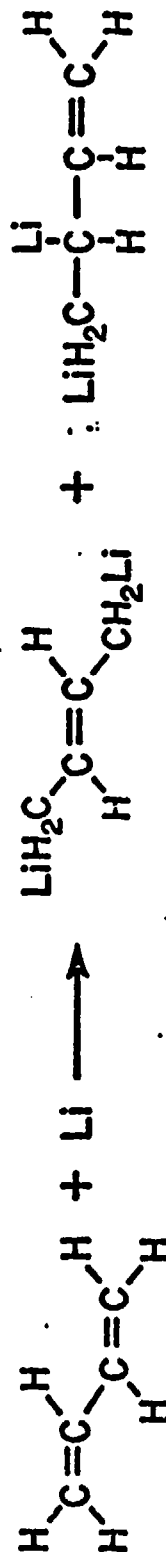
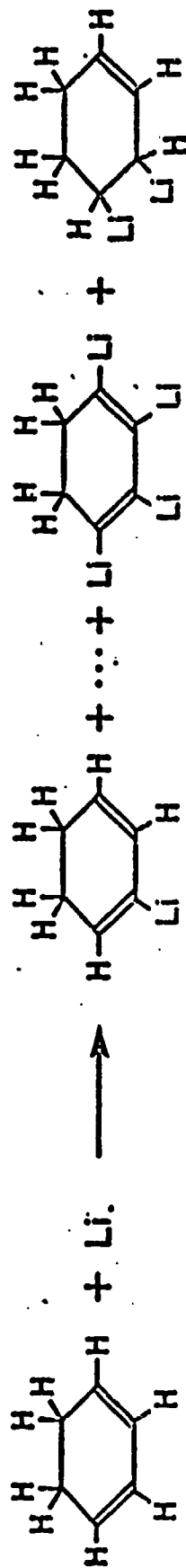
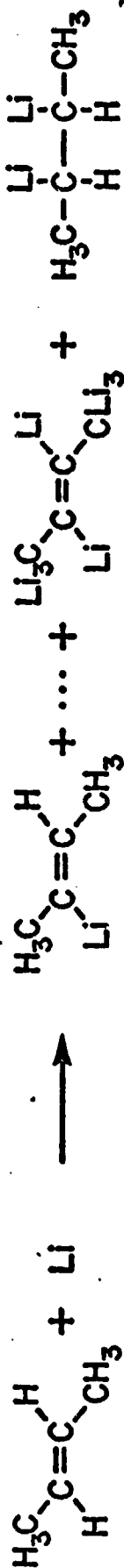
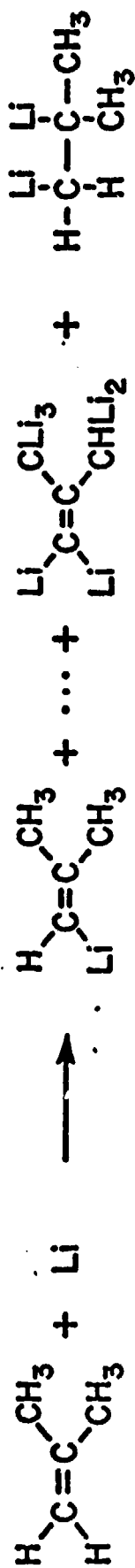


Fig. 5

## Most Recent Results

One of the most exciting recent results in this area is the synthesis of the first polylithium ethers.  $C_3Li_7OC_3Li_7$  has been prepared recently and is being characterized. This development opens many possibilities in the polymer area such as using structures with ether linkages as monomers and the possibility of obtaining other oxygen containing polylithium compounds.

Another completed study<sup>9</sup> has indicated that perlithiocarbons may be obtained by the reaction of lithium vapor with partially chlorinated hydrocarbons. Perlithio propane  $C_3Li_6$  has been obtained from several monochloro isomers. Similar reactions have produced other novel polylithium compounds. These results suggest that the replacement of a halogen by lithium is so exothermic, that the activation energy required for the lithium to abstract hydrogen is available. The result is similar to that obtained with a vibrationally excited alkane and suggests vibrational excitation.

Recently structural studies have been initiated on several polylithium compounds. We have been interested in the lithium and carbon 13 NMR spectra and the laser-raman spectra of polylithium compounds both in solution and in the solid state. Very encouraging results have been obtained. Such studies will also lead to accurate methods for determination of concentration of reactive polylithium intermediates in solution and for identification of polylithium compounds.

A major breakthrough<sup>10</sup> of great significance in synthetic chemistry and of prime interest in physical chemistry has come about through a collaboration with Professor J. S. Steinfield of our department. Lithium vapor generated at  $1000^\circ\text{C}$  has been selectively excited to the first excited electronic state (1.56 eV above ground state) with a tunable dye laser in 80 per cent yield. This electronically excited lithium has been found to react very efficiently with methane in contrast to no reaction at all when lithium is in the ground state. This reaction opens a whole new field of synthetic chemistry: the reaction of electronically excited lithium vapor. This chemistry will surely differ greatly from the chemistry of lithium vapor in the ground state. This event is also very significant because it is believed to be the first study of any synthetic reaction of a selectively electronically excited metal vapor and because it may provide input into synthetic routes to  $ClLi_4$  and  $C_2Li_6$ .

1. C. Chung and R. J. Lagow, "The Reaction of Lithium Atoms at 1000°C with Chlorocarbons; A New Route to Polylithium Compounds", Chem. Comm. 1079 (1972).
2. L. A. Shimp and R. J. Lagow, "The Reaction of Carbon Vapor with Lithium Atoms; A Direct Synthesis of Polylithium Compounds". J. Amer. Chem. Soc. 95, 1343 (1973).
3. L. A. Shimp, C. Chung, J. A. Morrison and R. J. Lagow, "The Reaction of Lithium Vapor with Benzene." J. Am. Chem. Soc. (in press).
4. L. A. Shimp and R. J. Lagow, "The Synthesis of Hexalithiobenzene" (to be published).
5. L. A. Shimp and R. J. Lagow, "The Reaction of High Temperature Lithium Vapor with Methane", submitted to J. Am. Chem. Soc.
6. J. A. Morrison and R. J. Lagow, "A New Synthesis for Tetralithiomethane", submitted to J. Am. Chem. Soc.
7. J. A. Morrison, C. Chung and R. J. Lagow, "The Reaction of High Temperature Lithium Vapor with Olefins; A Synthesis for Polylithium Compounds", J. Am. Chem. Soc., Feb. (1975) (in press).
8. J. A. Morrison and R. J. Lagow, "The Synthesis of  $\text{SiLi}_4$ ,  $\text{GeLi}_4$  and  $\text{BLi}_3$ " (manuscript in preparation).
9. L. G. Sneddon and R. J. Lagow, "The Reaction of Chloroalkanes with High Temperature Lithium Vapor", submitted to J. Am. Chem. Soc.
10. R. J. Lagow, L. A. Shimp, F. Lucer and J. S. Steinfield, "The Reaction of Laser Induced Electronically Excited Lithium with Methane", (manuscript in preparation).